

March 2022

Finding Signal in the Noise: High-Fidelity, Quantitative, Optical Blood Perfusion Imaging with Interference

Abdul Mohaimen Safi
University of South Florida

Follow this and additional works at: <https://digitalcommons.usf.edu/etd>



Part of the [Biomedical Engineering and Bioengineering Commons](#), [Electrical and Computer Engineering Commons](#), and the [Optics Commons](#)

Scholar Commons Citation

Safi, Abdul Mohaimen, "Finding Signal in the Noise: High-Fidelity, Quantitative, Optical Blood Perfusion Imaging with Interference" (2022). *USF Tampa Graduate Theses and Dissertations*.
<https://digitalcommons.usf.edu/etd/10351>

This Dissertation is brought to you for free and open access by the USF Graduate Theses and Dissertations at Digital Commons @ University of South Florida. It has been accepted for inclusion in USF Tampa Graduate Theses and Dissertations by an authorized administrator of Digital Commons @ University of South Florida. For more information, please contact digitalcommons@usf.edu.

Finding Signal in the Noise: High-Fidelity, Quantitative, Optical
Blood Perfusion Imaging with Interference

by

Abdul Mohaimen Safi

A dissertation submitted in partial fulfillment
of the requirements for the degree of
Doctor of Philosophy in Electrical Engineering
Department of Electrical Engineering
College of Engineering
University of South Florida

Major Professor: Ashwin Parthasarathy, Ph.D.
Ramesh Ayyala, M.D.
Christopher Passaglia, Ph.D.
Ismail Uysal, Ph.D.
Jing Wang, Ph.D.

Date of Approval:
March 31, 2022

Keywords: Speckle, Instrumentation, Interferometry, Preclinical

Copyright © 2022, Abdul Mohaimen Safi

Dedication

This dissertation is dedicated to my family and friends who have always motivated me throughout my Ph.D.

Acknowledgments

Firstly, I am grateful to Allah Almighty for providing me with the confidence and fortitude to seek and achieve this massive goal. Throughout my Ph.D. studies at USF, I am grateful to many people, who helped me both in terms of research and personally. I hope I can make them proud by transferring the skills and knowledge to the future generation. Professor Ashwin Parthasarathy, my advisor, deserves special thanks. Even though I had no prior knowledge of speckle theory or diffuse optics, Prof. Parthasarathy took a bet on me and offered me a Ph.D. position in TROPICS lab. His constant supervision, encouragement, and enthusiasm for research have played a pivotal role in the development of my scientific knowledge, in addition to just providing me with the opportunity. Whenever I encountered problems both in research and personal life, he provided me with valuable advice and guidance. I would like to express my gratitude to Professor Christopher Passaglia, Professor Jing Wang, Professor Ismail Uysal, and Professor Ramesh Ayyala, members of my committee. Their suggestions and in-depth knowledge helped me to mature my research. I am grateful to Professor Diane Allen-Gipson, my dissertation committee chair, and collaborator. Her continuous encouragement, motivation, and expertise, aid me to give a successful defense. The favorable climate of the research group contributes to successful research in Ph.D. I am fortunate to be surrounded by wonderful people from whom I have learned a lot. During my four and half years at TROPICS, I met some amazing people. I want to thank Sadhu Moka in particular, for not just assisting me with my research but also with my personal life. I remember, we discussed lots of ideas to make our projects work and would try different experiments to prove our hypothesis till late at night. He became more like a brother to me rather than a colleague as I can share

everything with him. Another special person is Mitchell Harrah; even though we know each other for more than two years, I feel like I have known him more than this. Together with him, I won my first international competition, which was a morale booster for me. His positive attitude and personality always helped me cheer up even in tough times. I am thankful to Parveen for sharing her insights on data processing and helping me prepare for my candidacy and final defense presentation. I'd want to thank all the lab members I met during my stay: Dillon, Nikola, Stephen, Arindam, Dheeraj, and Arslan. I'd also like to express my gratitude to Dr. Lianchun Wang (Byrd Research Institute) and Dr. Wesley Valdes (Hyperbaric and Wound Care Inc.), for their insightful questions and constructive criticism. Also, a big thank you to the EE staff - Diana Hamilton and Kristen Brandt for helping me out with the administrative work.

I am indebted to my best friends Muhammad Mohsin Qureshi, Myeongsu Seong, and Young Jae Rye, for teaching me to work with the optics and alignment tricks back in the days when I was a master's student in South Korea. My parents and sister deserve special acknowledgment, without their constant prayers and emotional support, my Ph.D. would be unfinished. I forever owe to them, and I hope I can make them proud in the future. A huge contribution for my motivation goes to my fiancé, her prayer, love, caring, and continuous encouragement helped me to achieve this big goal.

I am thankful to my roommates Mitchell Farmer, Zain, and Mohammed for helping me out in my time of need. I would like to thank, Sujie Chen and Dr. Sri Goyal (Student Innovation Incubator, USF CONNECT), for giving me confidence that I can also be an entrepreneur and helping me out throughout my stay in USF.

Table of Contents

| | |
|---|-----|
| List of Tables | iii |
| List of Figures | iv |
| Abstract | vi |
| Chapter 1: Introduction | 1 |
| 1.1 Introduction..... | 1 |
| 1.2 Thesis Objective | 3 |
| 1.3 Thesis Outline | 3 |
| Chapter 2: Light-Tissue Interaction | 5 |
| 2.1 Introduction..... | 5 |
| 2.2 Absorption | 7 |
| 2.3 Scattering | 9 |
| 2.4 Photon Propagation in Tissue | 11 |
| 2.5 Extracting Tissue Properties- Speckle Based Approach..... | 15 |
| 2.5.1 Interferometry | 15 |
| 2.5.2 Diffuse Correlation Spectroscopy (DCS) | 17 |
| 2.5.3 Time Resolved Measurement | 18 |
| 2.6 Conclusion | 19 |
| Chapter 3: Synthetic Multi-Exposure Laser Speckle Imaging | 20 |
| 3.1 Introduction..... | 20 |
| 3.2 Methods | 23 |
| 3.2.1 Working Principle of syMESI | 23 |
| 3.2.2 Optical Setup..... | 26 |
| 3.2.3 Microfluidic Phantom Preparation..... | 27 |
| 3.2.4 Animal Model Preparation..... | 27 |
| 3.3 Results..... | 29 |
| 3.3.1 Proof of Principle Experiments in Microfluidic Flow Phantom | 29 |
| 3.3.2 Proof of Principle with Static Layer | 31 |
| 3.3.3 <i>In vivo</i> Demonstration of Quantitative Assessment of CBF | 32 |
| 3.3.4 Fidelity of CBF Changes with an <i>In vivo</i> Cautery Experiment | 34 |
| 3.3.5 High Speed Measurement to Evaluate Pulsatility of Flow | 37 |
| 3.4 Feasibility of Synthetic MESI Approach in Diffusion Regime | 37 |
| 3.4.1 Optical Instrument | 39 |
| 3.4.2 Detecting Deep Tissue Blood Flow with Synthetic MESI | 39 |
| 3.5 Discussion..... | 41 |

| | |
|--|-----|
| Chapter 4: Heterodyne Synthetic Multi-Exposure Laser Speckle Imaging..... | 46 |
| 4.1 Introduction..... | 46 |
| 4.2 Heterodyne Speckle Model..... | 47 |
| 4.3 Instrumentation..... | 49 |
| 4.4 Results..... | 49 |
| 4.4.1 Boosting Weak Dynamic Signal..... | 49 |
| 4.4.2 Quantitative Imaging of Flow in Presence of Photon Shot Noise..... | 51 |
| 4.4.3 Linearity of Large Flow Changes in Presence of Photon Shot Noise..... | 52 |
| 4.5 Discussion..... | 54 |
| Chapter 5: Continuous Wave Pathlength Resolved Diffuse Correlation Spectroscopy..... | 57 |
| 5.1 Introduction..... | 57 |
| 5.2 Theory..... | 61 |
| 5.3 Data Processing..... | 63 |
| 5.4 Instrumentation..... | 63 |
| 5.5 Results..... | 65 |
| 5.6 Discussion..... | 66 |
| Chapter 6: Conclusion and Future Work..... | 70 |
| 6.1 Dual Wavelength Synthetic Multi-Exposure Imaging for Wound Care..... | 71 |
| 6.2 Quantitative Assessment of Neurovascular Coupling..... | 71 |
| 6.3 Blood Coagulation Measurement Using Synthetic Multi-Exposure Imaging..... | 72 |
| 6.4 Wearable Deep Tissue Blood Flow Monitoring..... | 73 |
| 6.5 Path-Length Resolved Measurement of Cerebral Autoregulation..... | 73 |
| References..... | 75 |
| Appendix A: Copyright Permissions..... | 103 |
| Appendix B: IRB Approval Pages..... | 110 |
| Appendix C: IACUC Approval Pages..... | 111 |

List of Tables

| | |
|---|----|
| Table 1.1 Characteristics of different lasers | 16 |
|---|----|

List of Figures

| | |
|--|----|
| Figure 2.1 Jablonski diagram..... | 6 |
| Figure 2.2 Absorption and scattering coefficient in human skin..... | 7 |
| Figure 2.3 Different regimes for <i>in vivo</i> optical imaging | 13 |
| Figure 2.4 Speckle formation interferometry approach..... | 17 |
| Figure 2.5 Schematic for diffuse correlation spectroscopy | 18 |
| Figure 2.6 Time resolved measurement scheme..... | 19 |
| Figure 3.1 Working principle of synthetic multi-exposure speckle imaging (syMESI)..... | 25 |
| Figure 3.2 Experimental setup for syMESI | 26 |
| Figure 3.3 Microfluidic channel | 28 |
| Figure 3.4 syMESI on microfluidic flow phantom study | 31 |
| Figure 3.5 syMESI on the effect of static layer | 33 |
| Figure 3.6 syMESI of blood flow in a rodent brain <i>in vivo</i> | 35 |
| Figure 3.7 Application of syMESI during cautery in rodent model | 36 |
| Figure 3.8 Pulsatility of flow | 38 |
| Figure 3.9 Schematic diagram of experiment for synthetic multi-exposure speckle imaging applied to measure deep tissue blood flow with diffuse speckle contrast analysis (DSCA)..... | 40 |
| Figure 3.10 Validation syMESI algorithm in DSCA setup | 41 |
| Figure 3.11 Measurement of % rBF by syMESI algorithm using DSCA systems during arm cuff occlusion protocol | 42 |
| Figure 4.1 Schematic for heterodyne multi-exposure speckle imaging..... | 50 |

| | | |
|------------|---|----|
| Figure 4.2 | Characterization of heterodyne synthetic multi exposure speckle imaging | 51 |
| Figure 4.3 | Comparison between homodyne speckle imaging and heterodyne synthetic MESI speckle contrast map for flow rate 5mm/s..... | 52 |
| Figure 4.4 | Heterodyne syMESI on microfluidic phantom study | 55 |
| Figure 5.1 | Schematic of noninvasive, fast measurement of CBF waveforms with diffuse correlation spectroscopy (DCS) | 60 |
| Figure 5.2 | Data analysis scheme for pathlength resolved diffuse correlation spectroscopy (PR-DCS) | 64 |
| Figure 5.3 | Schematic of proposed pathlength resolved diffuse correlation spectroscopy (PR-DCS) instrument..... | 65 |
| Figure 5.4 | Experimental validation of pathlength resolved diffuse correlation spectroscopy (PR-DCS)..... | 67 |
| Figure 5.5 | PR-DCS on <i>in vivo</i> experiment | 68 |
| Figure 6.1 | Dual wavelength synthetic multi-exposure imaging | 72 |

Abstract

For label-free, non-invasive, wide field-of-view (FOV) imaging/monitoring of blood flow, speckle-based approaches are gaining popularity. However, to obtain quantitative flow information, speckle techniques rely on the multi-exposure scheme which requires complex, bulky, and expensive instrumentation, limiting its application to preclinical studies. This dissertation directly addresses these issues. In the first part of this dissertation, we report a novel single shot synthetic multi-exposure speckle imaging (syMESI) method to synthetically produce multi-exposure images from one short single exposure speckle image using spatial binning/averaging. We demonstrate that syMESI can reimagine conventional hardware based MESI, with low-cost single exposure laser speckle imaging (LSCI) instrumentation. We validate the syMESI algorithm with flow experiments on microfluidic channels, and by imaging cerebral blood flow in rodent brain *in vivo*. In the second part of this dissertation, we introduce a novel heterodyne instrument for imaging blood flow and new heterodyne laser speckle theory and model. We demonstrate that our new technique, can increase the signal-to-noise ratio (SNR) of blood flow measurements and can quantify flow images at low photon budget (<40 average detection intensity). These two techniques, transform traditional expensive multi-exposure method into a low-cost quantitative imaging tool, solving a decade long problem. Finally, we introduce a new diffuse optical instrument by combining a low coherence laser diode and a Mach-Zehnder interferometer, for obtaining dynamic properties (optical properties and blood flow). Our new instrument can provide deep tissue information by utilizing the diffusion theory of photon propagation. The capability to record path resolved diffuse optical measurements using a

continuous (CW) laser source allows our instrument to operate at source-distance (S-D) separation of 2.5 cm or greater. As a proof of concept, we demonstrate results of intralipid phantom and *in vivo* arm-cuff occlusion. We believe, this new path-resolved instrument will enable researchers to uncover deep tissue optical properties information which cannot be performed with traditional diffuse correlation technique.

Chapter 1: Introduction

1.1 Introduction

Light Amplification by Stimulated Emission of Radiation (LASER) is one of the discoveries that has paved the way for many scientific discoveries. In the late 1950s, Schawlow-Townes introduced the concept and started the race for building practical working laser (Schawlow & Townes, 1958). In the early, 1960's Theodore Maiman from Hughes Research Lab demonstrated the first commercial working laser (Maiman, 1960). By the 1970's with the invention of the laser printer and laser bar code scanner the application of laser got widely recognized. Researchers who were working with laser found a strange phenomenon, when laser light reflected from surface like paper, wood, metal, etc., the observed reflected light was granular in nature (Dainty, 1972; Fujii & Asakura, 1974, 1975; Goodman, 1975; Langmuir, 1963; Parry, 1975; Pedersen, 1974). This granular pattern was termed as "speckle" and was initially considered as noise. Interestingly, this speckle pattern forms due to the roughness of the surface and almost all the material in the world is rough.

Parallely, in the 1950s several researchers used the laser to explore dynamic light scattering (DLS) (Bosworth et al., 1952; Doty & Steiner, 1950; Kratochvil & Smart, 1965; Outer et al., 1950; Zimm, 1945, 1948). Foord and colleagues in 1970, first time experimentally demonstrated the relationship between diffusion coefficient and light scattering, this laid the framework for particle sizing using dynamic light scattering (Foord et al., 1970). In the DLS field, researchers observed that, in random medium, light waves scattered from particles experience phase shifts resulting in a fluctuating speckle pattern; this phenomenon is analogous to doppler

shift where intensity fluctuates. Various research groups utilized this temporal fluctuation to obtain blood flow information (Bonner & Nossal, 1981; Pine et al., 1988; Stern, 1975). In 1980, Fercher and Briers, for first time, demonstrated non-invasive, label free blood flow imaging of retina using a camera and the speckle method and this gave rise to “Laser Speckle Imaging” as a field of research (Fercher & Briers, 1981). This speckle imaging field opens up new exciting research field such as deep tissue light focusing in turbid media (Conkey et al., 2012; Judkewitz et al., 2013; Vellekoop & Mosk, 2008), speckle image velocimetry (Qureshi et al., 2021; Safi et al., 2019), quantitative blood flow imaging/monitoring (Bandyopadhyay et al., 2005; Bi et al., 2013; Parthasarathy et al., 2008) etc.

Laser speckle is a random homodyne interference pattern produced in the image plane due to light backscattered from random media (such as tissue) traveling multiple trajectories with different optical pathlengths. If the object is stationary, the interference pattern does not change over time (i.e., static speckle pattern); moving particles in the imaging volume such as red blood cell will cause the interference pattern to fluctuate both in time and space (i.e., dynamic speckle pattern) due to the changes imparted in the light pathlength by the moving scatterer. For dynamic sample, as the camera exposure time is typically longer than sample decorrelation time, this spatio-temporal fluctuation manifests as blurring in the camera image. Quantification of this blurring, as speckle contrast (usually in the range from 0 to 1) is a direct measure of motion (blood flow in tissue) within the sample. Blood flow typically follows the inverse of this speckle contrast. Over the years, various image processing algorithms have been developed to extract flow information image from the speckle contrast. A detail of these algorithms can be found in the review articles published by various groups (Boas & Dunn, 2010; Draijer et al., 2009; Senarathna et al., 2013).

Laser speckle shares the same principle of dynamic light scattering technique where temporal fluctuation is captured using high speed detector (Boas & Yodh, 1997; Boas et al., 1995; Wang et al., 2016). The spatial-temporal fluctuation of speckle has allowed the invention of affordable deep tissue flow monitoring tool such as Diffuse Correlation Spectroscopy (DCS) where single speckle fluctuation is utilized and Diffuse Speckle Contrast Analysis (DSCA) where flow information is extracted from multiple time-varying speckles captured by a camera (Bi et al., 2013).

1.2 Thesis Objective

The objective of this thesis is to image/obtain blood flow quantitatively from biological tissue at high-speed, with a low-cost scheme. To distinguish between healthy and disease tissue quantitative baseline flow imaging plays a critical role. Even though over the years many instruments have been developed to quantitative imaging of blood flow, their ability to provide quantitative information is limited by the instrumentation. Here, in my thesis, I have developed a software algorithm based on the speckle ergodicity that can estimate quantitative baseline blood flow, reproducing the capabilities of traditional hardware based MESI method. I have also developed new theory and instrument to overcome photon shot noise, which is one of the biggest problems of MESI operating in short-exposure time. I have experimentally demonstrated, the efficacy of the new model and instrument, and evaluate how much quantitative flow information I can recover in the photon shot noise limit.

1.3 Thesis Outline

Outline of this thesis is as follows:

Chapter 2 provides a brief introduction to light-tissue interaction, and the role of optics to extracts quantitative information from tissue. This chapter introduces the properties of different

light source and optical techniques which lay the foundation of ideas discussed in the later chapters.

Chapter 3 describes an algorithm utilizing spatial binning approach of the camera pixel, thereby synthetically reproduces exposure time in a single shot scheme. This allows performing multi-exposure speckle contrast imaging using a traditional single exposure speckle imaging instrument thereby reducing the system cost 400-fold. Our new technique opens analysis of dynamic light scattering using spatial statistics approach.

In chapter 4, we have introduced and experimentally validated a new theory and instrument “Heterodyne Multi-exposure Speckle Imaging”. This new instrument allows imaging of quantitative flow at photon shot noise limit using only low power laser. This technique enables increasing dynamic range of any low-cost CMOS sensor.

In chapter 5, we have translated the application of interferometry in the diffusion regime. We have showed interferometric theory and a diffuse correlation spectroscopy instrument which can provide deep tissue path length resolved blood flow as well as provide optical properties of tissue. This new system has the potential of deep brain blood flow estimation which traditional diffuse correlation spectroscopy is unable to provide.

Finally, in chapter 6, I include future applications of my developed theory and instruments which I believe will provide clinicians and researchers in the biomedical optics field.

Chapter 2: Light-Tissue Interaction

2.1 Introduction

Interaction of light with biological tissue provides various contrast mechanism which enables quantitative information about the tissue. Light-matter interaction can be classified into two classes a) resonant and b) non-resonant. These classes direct the typical contrast phenomena such as absorption, scattering, fluorescence, and phosphorescence. These can be better understood using the Jablonski diagram shown in Figure 2.1. In optical imaging, utilizing these contrast mechanisms biological tissue's structural and functional information can be obtained.

In resonant interactions, incoming photon energy matches the internal energy of the material; molecules absorb this energy and electrons from ground state jump to an excited state. Electron from excited state can relax back to natural ground state in two pathways a) nonradiative b) radiative relaxation.

In non-radiative relaxation process, excited electron returns to ground state without releasing any photon and dissipates the energy as heat. Non-radiative relaxation processes include vibrational relaxation, internal conversion, and intersystem crossing.

In radiative process, a photon is emitted when the electron energy decays to its ground state. This radiative process is the basis of laser generation – hence the term stimulated emission is in the abbreviation of laser. Fluorescence is one of the examples of the radiative process which typically last in the order of nanosecond. Phosphorescence goes through intersystem crossing; hence the time scale is typically in the order of milliseconds to seconds, much slower than fluorescence.

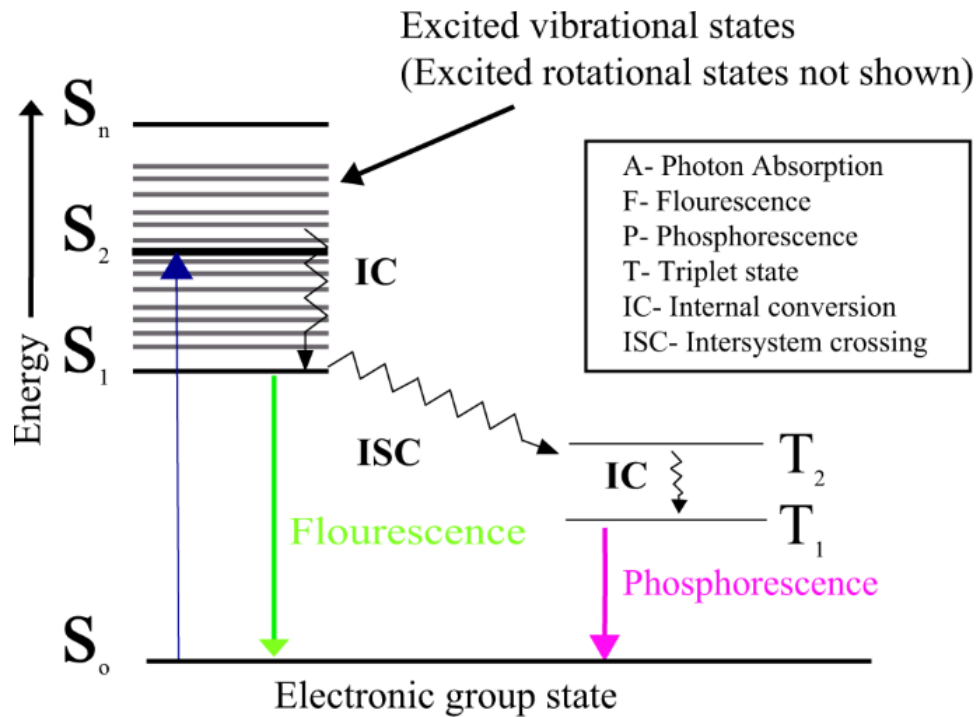


Figure 2.1 Jablonski diagram (Iyer et al., 2019)

Non-resonant interaction process corresponds to situations when incoming photon energy does not match the internal energy of the material. This type of interaction is usually characterized by elastic and non-elastic scattering. In elastic scattering, scattered light frequency or wavelength is the same as incident light. Rayleigh and Mie scattering are the examples of elastic scattering. In inelastic scattering, scattered light shows different wavelength. Typically, Raman scattering is characterized as inelastic scattering.

Light-matter interaction governs the imaging system, whether it is super resolution microscope or human eye. Light when illuminate sample, it experiences- a) absorption b) scattering. Typically, in biological sample scattering dominates than absorption. This scattering is the fundamental principle of designing imaging system as resolution is dependent of the scattering of the sample. Figure 2.2 shows effect of absorption and scattering with respect to wavelength in biological tissue. Also, scattering enables quantitative imaging system by providing information

of molecule size, internal complexity, and heterogeneity of sample. Next section will provide in detail discussion about light scattering and absorption in biological tissue.

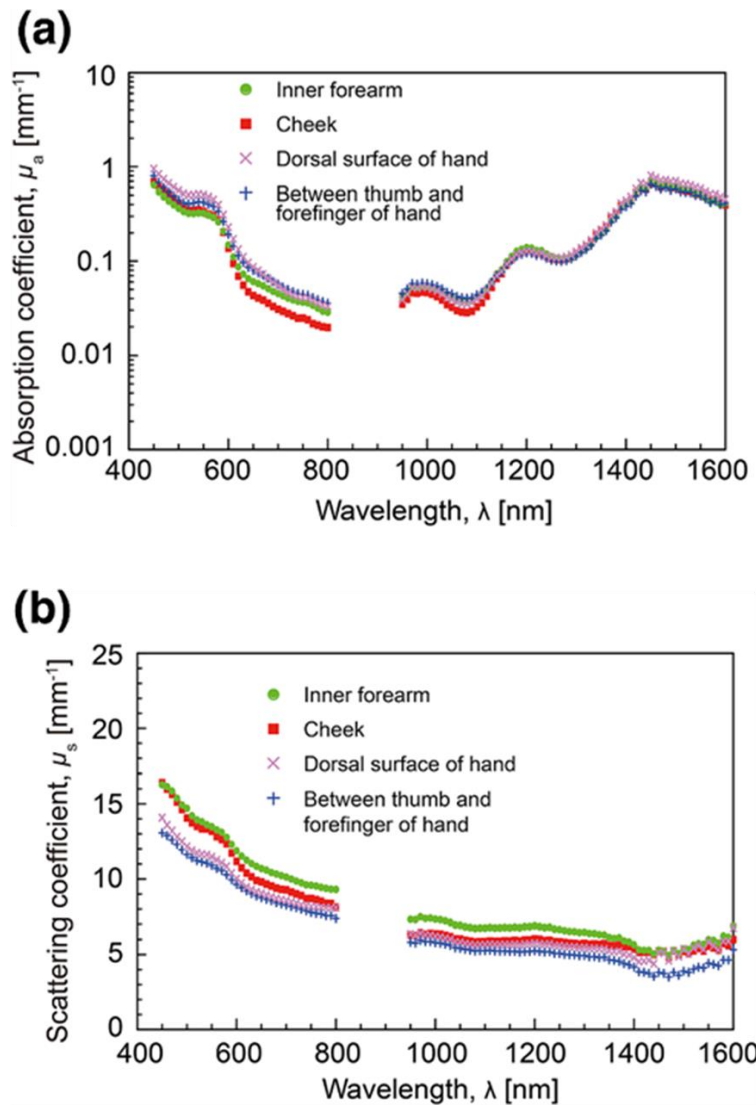


Figure 2.2 Absorption and scattering coefficient in human skin (Kono & Yamada, 2019)

2.2 Absorption

When, biological sample is illuminated by light, molecules in the sample absorb photon energy, if the frequency or wavelength of the incoming light matches with the vibrational frequency of the molecule. In this case, electrons jump from its lower energy state E_1 to excited state E_2 . The difference between them can be expressed as-

$$E_2 - E_1 = \frac{hc}{\lambda}, \quad (\text{Eq. 2.1})$$

where h is the Planck's constant, c is the speed of light and λ is the wavelength of the light. When molecules return to the lower energy state, they dissipate the energy in the form of heat, which is the basis of absorption. Many optical imaging techniques rely on the principle of absorption. In fact, popular pulse-oximetry method is based on absorption of light by blood. In tissue, typical absorbers in ultraviolet and visible wavelength range are typically DNA, lipids, hemoglobin whereas in near infrared region water, lipids, and hemoglobin are the primary absorbers.

Light absorption in tissue is characterized by the absorption coefficient of the tissue. To quantify this, let us consider simple scenario a collimated light of intensity, I_0 illuminating a thick slab length L , assuming slab is containing absorbing media and intensity of light transmitted from the slab is I . Now if we assume concentration of molecule in the absorbing media is N (cm^{-3}), effective absorption cross-section σ_a (cm^2), and the slab is made up of thin slices whose thickness is dx , we can write probability of photon being absorbed in dx as:

$$P(\text{Absorbed}@dx) = N\sigma_a dx, \quad (\text{Eq 2.2})$$

Intensity of light absorbed in that thin slice of dx with respect to the illuminating intensity I_0 is:

$$dI = I_0 N\sigma_a dx, \quad (\text{Eq. 2.3})$$

If we integrate and rearrange this equation, we can establish a formula for absorption for the whole slab and this can be written as:

$$I = I_0 e^{-N\sigma_a L}, \quad (\text{Eq. 2.4})$$

We can define absorption coefficient as:

$$\mu_a = N\sigma_a, \quad (\text{Eq. 2.5})$$

Following our unit convention, unit of absorption coefficient is (cm^{-1}), inverse of this is mean free path for absorption (cm) i.e., average distance a photon is travelled before being absorbed.

We can write it as:

$$l_a = \frac{1}{\mu_a}, \quad (\text{Eq. 2.6})$$

Finally, in terms of absorption coefficient we can rewrite the Eq. 2.4 as:

$$I = I_0 e^{-\mu_a L}, \quad (\text{Eq. 2.7})$$

This equation represents emitted intensity, I attenuate based on the absorption coefficient and optical path length of the of the absorptive media. This phenomenon is known as Beer-Lambert law (Mayerhöfer et al., 2020).

2.3 Scattering

In biological tissue, scattering is mostly elastic, where scattered light energy is same as the incident energy. Variation of refractive index inside the tissue cause scattering in the tissue. Some examples of scatters in biological tissue are collagen, cells, mitochondria, and vesicles. Scattering is strongly dependent on scatterers size and wavelength. Based on size scattering can be divided into two categories: a) Rayleigh scattering b) Mie scattering (Lockwood, 2016)

Rayleigh scattering refers to scattering from particles which are typically smaller than the incident wavelength of light. In general, for Rayleigh scattering to happen, size of the scatters, $d < 0.1 \lambda$ (wavelength of light) and scattering intensity is dependent on wavelength. A practical example of Rayleigh scattering is blue sky in a sunny day, where air molecules act as a Rayleigh scatterer. Since Rayleigh scattering is dependent on wavelength, blue wavelength, which is short in the range of 400 nm, is scattered more than longer wavelengths. Hence, sky looks blue.

In biomedical optics, Mie scattering is more important as it is related to scatterers of bigger scatter sizes. Typically, for Mie scattering the scatterer size ($d > 0.1 \lambda$ (wavelength of light)). However, in this category, scatterer intensity is independent of the wavelength. In biological sample, typically cells which are in order of 10 μm usually act as a Mie scatterer. A more common

example of Mie scattering is, in a sunny day cloud looks white as particles scattering is independent of wavelength of the sun light.

Like absorption coefficient, to quantify scattering, let us consider collimated light of intensity, I_0 illuminating a thick slab length L , containing scattering medium only and intensity of light transmitted from the slab is I . Now if we assume, concentration of molecule in the scattering media is N (cm^{-3}), effective scattering cross-section σ_s (cm^2), and the slab is made up of thin slices whose length is dx , similar to absorption, we can write probability of photon being scattered in dx as:

$$P(\text{scattered @ } dx) = N\sigma_s dx, \quad (\text{Eq. 2.8})$$

Intensity of light absorbed in that thin slice of dx with respect to the illuminating intensity I_0 is:

$$dI = I_0 N\sigma_s dx, \quad (\text{Eq. 2.9})$$

If we integrate and rearrange this equation, we can establish a formula for scattering for whole slab as follows:

$$I = I_0 e^{-N\sigma_s L}, \quad (\text{Eq. 2.10})$$

We can define scattering coefficient as:

$$\mu_s = N\sigma_s, \quad (\text{Eq. 2.11})$$

Following our unit convention, unit of scattering coefficient is (cm^{-1}), inverse of this is provide characteristics path for scattering (cm). We can write it as:

$$l_s = \frac{1}{\mu_s}, \quad (\text{Eq. 2.12})$$

Finally, in terms of scattering coefficient we can rewrite the Eq. 2.9 as:

$$I = I_0 e^{-\mu_s L}, \quad (\text{Eq. 2.13})$$

When the photon scatters, change of the direction is of key importance as this laid the groundworks for the popular Monte-Carli simulation method for light propagation tissue. Typically scattering

anisotropy factor, g , quantifies the angular scattering behavior of photon. This is expressed as:

$$g = \langle \cos(\theta) \rangle, \quad (\text{Eq. 2.14})$$

Here, θ represents scattering angle. Anisotropy factor, g ranges between $[-1, 1]$. $g = -1$, indicates backward scattering. For isotropic scatter is $g = 0$. In case of forward scattering g value is close to 1. Biological samples mostly forward scatter, and g is assumed as 0.9.

2.4 Photon Propagation in Tissue

Biological tissue consists of both scatters and absorbers. As a results total extinction coefficient can be expressed as:

$$\mu_t = \mu_s + \mu_a, \quad (\text{Eq. 2.15})$$

Inverse of this is total extinction coefficient, i.e., $\frac{1}{\mu_t}$ which provides characteristic length (cm), which is known as mean free path (MFP). Typically, scattering is more dominant in tissue than absorption. Hence, MFP generally expressed as:

$$MFP = \frac{1}{\mu_s}, \quad (\text{Eq. 2.16})$$

So, we can say that MFP provides the value for mean length for the scattering events inside biological tissue. As μ_s is dictated by the scattering cross-section (σ_s) and number of scatterers (N), MFP shows inverse relationship to them. MFP in biological tissue $\sim 100 \mu\text{m}$.

As we have discussed before, in tissue photons undergo multiple scattering events before they either emerge out of the tissue or are absorbed. Considering degree of scattering, scattering coefficient, $\mu_s (\text{cm}^{-1})$ is expressed as reduced scattering coefficient,

$$\mu'_s = \mu_s(1 - g), \quad (\text{Eq. 2.17})$$

The unit of this also, cm^{-1} . Inverse of this provide a characteristic length of unit cm, which is the step size of random walk for photon in diffusion regime considering scattering is isotropic in every step.

When photon enters the tissue, it went through multiple scattering as a result photon lost its direction i.e., correlation between photon entering direction and the traveling direction breaks down. This is characterized the by diffusion process as photon direction assumed to be randomized and radiative transport equation (RTE) is applied to probe light-tissue interaction. This is associated to transport mean free path (TMFP). Like MFP, considering $\mu_s \gg \mu_a$, TMFP can be expressed in terms of μ'_s as:

$$TMFP = \frac{1}{\mu'_s}, \quad (\text{Eq. 2.18})$$

TMFP can be defined as the mean photon travel distance after which the photon loses its directionality i.e., becomes randomized. In tissue, TMFP is ~ 1 mm. On the other hand, MFP, where photon retain its directionality and generally, associated to ballistic regime and traditional microscopy techniques works in this regime. MFP can be expressed in terms of TMFP as:

$$MFP = (1 - g) TMFP, \quad (\text{Eq. 2.19})$$

So, it is apparent that, as the forward scattering increases i.e. g value increases, MFP increases, which leads to increasing of penetration depth without photon being diffused out (Ntziachristos, 2010). Figure 2.3 shows different optical imaging regime in relation to resolution and penetration depth.

Optical imaging in nanoscopic regime, breaks the diffraction barrier of conventional microscopy method. Typically, they allow spatial resolution in the order of less than 70 nm, enabling both functional and structural imaging of proteins. However, they are limited to penetration depth less than 100 μ m. To image in the super-resolution regime, along with sophisticated optical microscope such as photo activation localization microscope (PALM) (Betzig et al., 2006), stimulated depletion emission microscope (STED) (Hell & Wichmann, 1994),

stochastic optical reconstruction microscopy (STORM) (Rust et al., 2006), they rely on exogenous contrast agent such as SYFP, DY-480XL, etc. (Berning et al., 2012; Pellett et al., 2011).

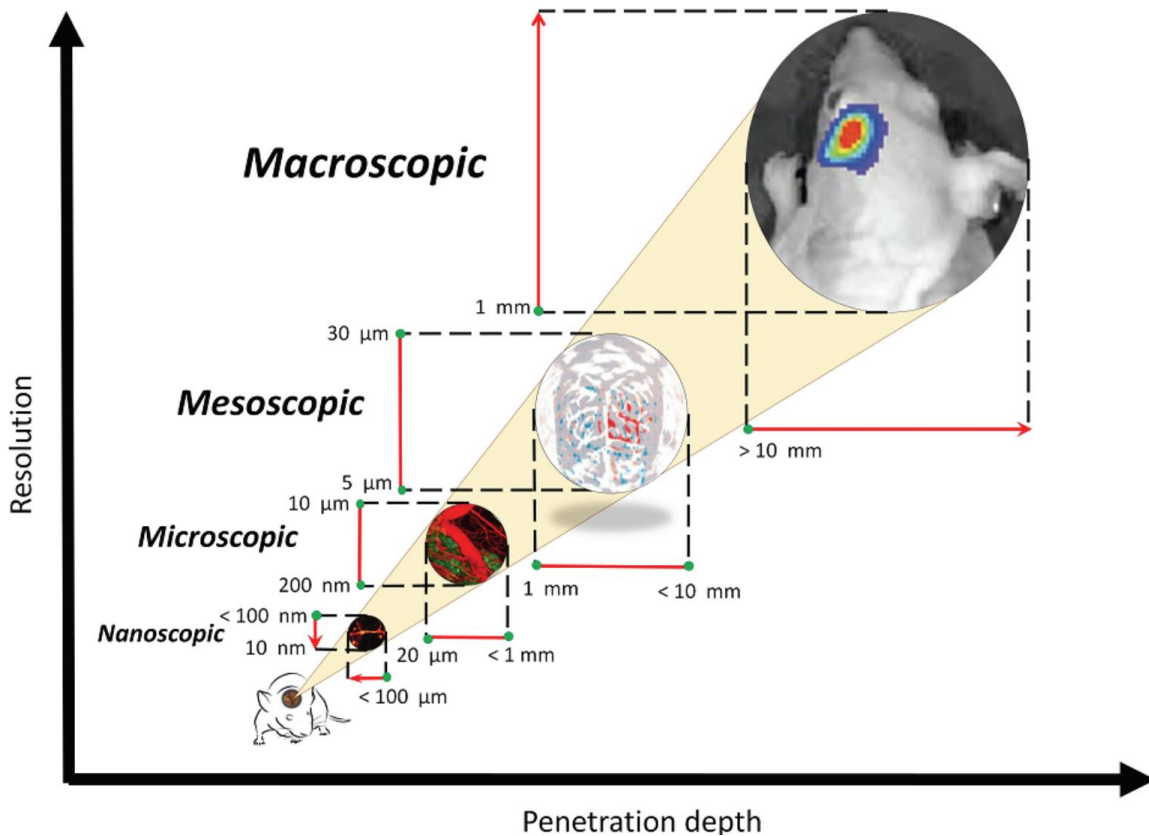


Figure 2.3 Different regimes for *in vivo* optical imaging. Resolution of imaging system is inversely related to the light penetration depth in the tissue due to the strong influence of optical scattering (Safi & Chung, 2015)

Imaging system under the category of microscopic realm works on either endogenous contrast agent such as oxyhemoglobin (HbO₂), deoxy hemoglobin (Hb), and autofluorescence or exogenous contrast agent such as fluorescent dyes, protein, gold nano shell etc. (Chong et al., 2011; Gratton, 2011; Ntziachristos, 2010). Imaging techniques such as two-photon/ multiphoton microscope (2P/MP) (Helmchen & Denk, 2005), confocal microscope typically offer resolution in the order of 0.5 μm and penetration depth up to 400 μm (Conchello & Lichtman, 2005; Masters, 2008). Optical Coherence Tomography (OCT), one of the most popular microscopy imaging

methods, allows penetration depth ~ 2 mm with a resolution in the order of $2 \mu\text{m}$ (Gabriele et al., 2011).

Mesoscopic imaging modalities usually falls on the diffusive regime in the order of 10 mm. They usually use endogenous contrast agent oxyhemoglobin (HbO_2), deoxy hemoglobin (Hb) to provide structural and functional information of tissue. Their resolution typically ranges from 5 to $20 \mu\text{m}$ with a penetration depth up to few mm. Laser speckle contrast imaging (LSCI) (Boas & Dunn, 2010; Draijer et al., 2009; Senarathna et al., 2013), photoacoustic microscopy (PAM) (Wang & Hu, 2012; Zhang et al., 2006), multispectral optoacoustic tomography (MSOT) (Ntziachristos & Razansky, 2010; Razansky et al., 2011), hyperspectral imaging (Yoon, 2022) are some popular techniques use in both clinical and research field (Cochran et al., 2021; Frijia et al., 2021; Gibson et al., 2005).

Similar to mesoscopic imaging macroscopic imaging also work in the diffusion region and to reconstruct image usually photon diffusion model used. However, techniques associated to macroscopic imaging usually have penetration depth in order of few cm and resolution in the order of mm. Techniques such as near infrared spectroscopy (NIRS) (Hashem et al., 2022; Kato, 2004; Torricelli et al., 2014), diffuse correlation spectroscopy (Shang et al., 2017), diffuse optical spectroscopy (Lam et al., 2021) usually use source-distance separations of 1-3 cm, and require multiple source/ detector pairs to form image. Their working principle relies on endogenous contrast agent especially, oxyhemoglobin (HbO_2), deoxy hemoglobin (Hb), red blood cell (RBC). Whereas techniques such as bioluminescence imaging (BLI) (Contag & Bachmann, 2002), near-infrared fluorescence imaging (NIRF) (Shah & Weissleder, 2005), utilize luciferin, near-infrared fluorophore etc.

2.5 Extracting Tissue Properties- Speckle Based Approach

In the previous section, we have provided a generalized theoretical background of the light-tissue interaction and the effect of absorption and scattering in imaging and extracting information from biological sample. As stated before, speckle is the resulting interference pattern due to coherent addition of light field that have travelled different pathlengths as they scatter through biological sample. Coherence of light source plays a critical role to obtain quantitative tissue properties. Coherence can be classified into two categories: a) temporal coherence (TCL) and b) spatial coherence (SCL).

Temporal coherence describes the consistency of optical phase of the light source over time along the propagation distance, whereas spatial coherence defined as the consistency of optical phase in space. Typically, Michelson interferometer, high resolution spectrometer can be used for measuring temporal coherence length of light source. A simple way to measure light source's spatial coherence length is Young's double slit experiment. Table 1.1 shows different sources and their coherence properties. Utilizing the property of light source coherence speckle can be produced. Next sections provide techniques which uses speckle in biomedical application.

2.5.1 Interferometry

Most common interferometry which can generate speckle is optical coherence tomography (OCT) which is based on the Michelson interferometer principle. Here, light is from a partially coherent source, of temporal coherence length in order of $<10 \mu\text{m}$. The source beam is divided into sample and reference arm. Backscattered light from both arms is detected by a camera or photodetector. Speckle is generated only when the optical path length of both arms match. This allows depth resolved measurement of flow. Figure 2.4 shows speckle formation by interferometry method for a bead of size $1 \mu\text{m}$. Dynamic full field OCT (Scholler, 2019; Scholler et al., 2019),

speckle variance OCT (Conroy et al., 2012; Liu et al., 2011; Mariampillai et al., 2010) mainly use speckle to get dynamic information of tissue.

Table 1.1 Characteristics of different lasers

| Source Type | Temporal Coherence Length | Spatial Coherence Length | Comments |
|--------------------------|----------------------------------|---------------------------------|--|
| Laser (Single frequency) | >100m | High | Best for speckle imaging, holography, spectroscopy application |
| Laser (Single Mode) | ~3-4m | High | Good for speckle imaging, however, limited spectroscopy and holography when coupled with multimode fiber. |
| Laser (Multimode) | ~0.5-1 mm | Low | Not suitable for speckle imaging, holography and spectroscopy. Spatial mode can be improved using pinhole or coupling to single mode approach. |
| LED | Tens of μm | Low | Not suitable |

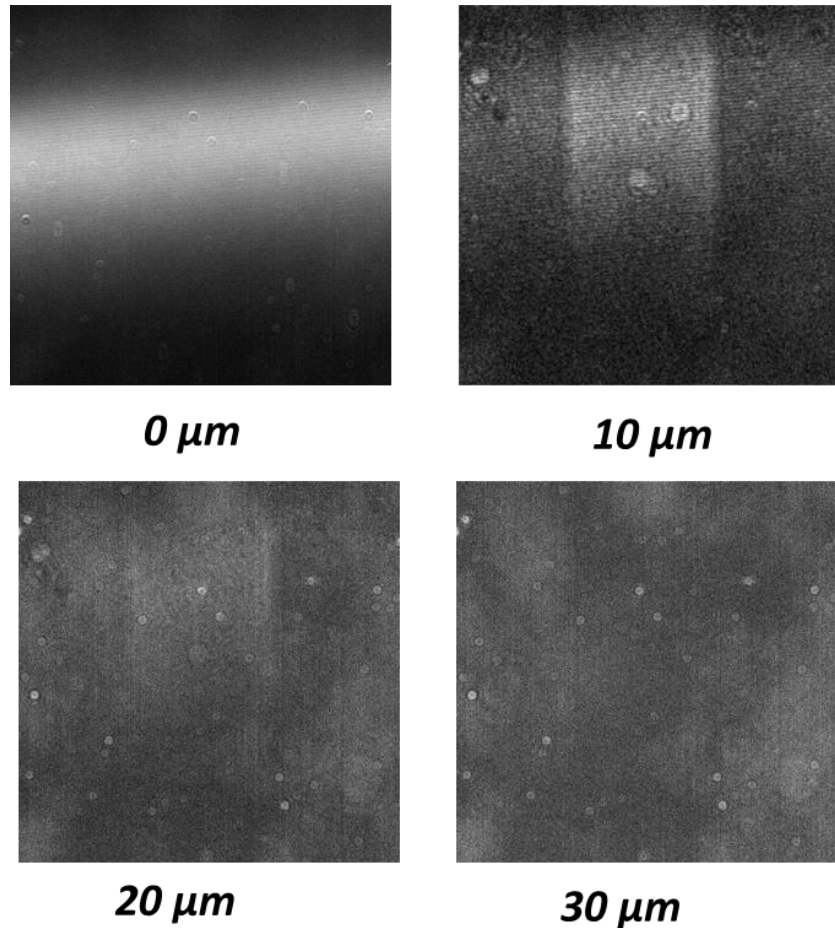


Figure 2.4 Speckle formation interferometry approach. At depth $0 \mu m$ where optical pathlength matches optical path length of the glass slide. At $10 \mu m$ depth strong speckle formation observed due to the matching of pathlength of flowing beads with reference arm and gradually speckle/interference diminishes at $30 \mu m$ depth.

2.5.2 Diffuse Correlation Spectroscopy (DCS)

Diffuse correlation spectroscopy (DCS) uses high coherence single frequency laser to probe deep into the tissue (Boas & Yodh, 1997; Boas et al., 1995; Wang et al., 2016). Typically, temporal intensity fluctuation can be captured either use of single mode fiber and SPAD detector (Wang et al., 2016) or multiple speckles using multimode fiber and array of SPAD detector/highly sensitive camera (Bi et al., 2020; Dragojević et al., 2018; Huang et al., 2016; Liu et al., 2021; Sie et al., 2020; Varma et al., 2014). Temporal intensity fluctuations are quantified with an intensity autocorrelation function fit to a diffusion model to extract blood flow index. High coherence laser

source allows self-interference of light fields and allows retaining scattering correlation. Due to the use of high coherence laser source extracted blood flow information is from a distribution/spread of optical paths inside tissue. Use of sensitive high-speed detector/ camera allows source-distance separation up to 4 cm which allows higher depth inside tissue.

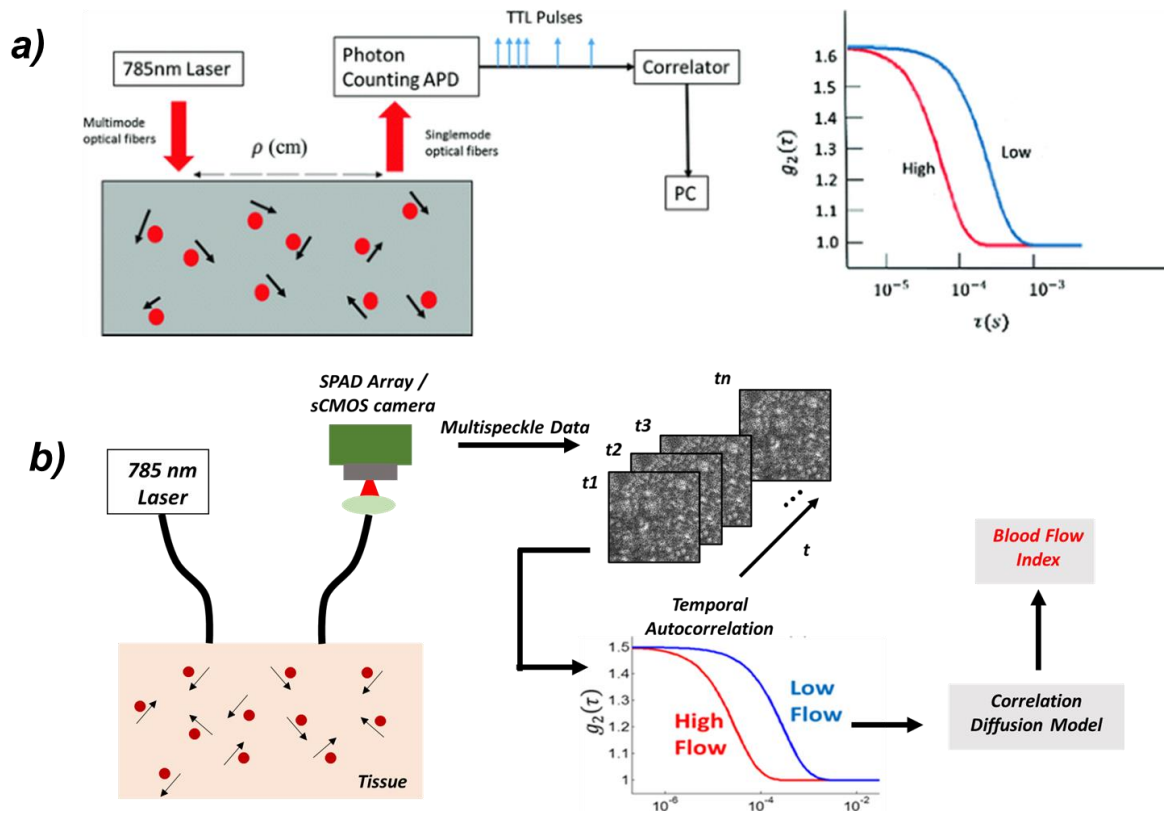


Figure 2.5 Schematic for diffuse correlation spectroscopy. a) single speckle method; single mode fiber and APD detector used for capturing temporal fluctuation (I.-T. Huang et al., 2018) b) Multi-speckle method; typically, large core multimode fiber and SPAD / sCMOS camera used for acquiring spatio-temporal fluctuation. Both methods are fit to diffusion model and provide similar blood flow indices.

2.5.3 Time Resolved Measurement

Using speckle in time resolved measurement is fairly a new technique. This allows optical discrimination of optical path length (Colombo et al., 2021; Guzman-Sepulveda & Dogariu, 2019; Kholiqov et al., 2020; Marco Pagliuzzi et al., 2021; Sutin et al., 2016), hence acquiring optical properties of tissue scattering coefficient (μ_s), absorption coefficient (μ_a), and blood flow index

simultaneously. This technique relies on pulse laser, where width of pulse governs the temporal coherence length of the laser which allows evaluation of blow index at each optical pathlength inside tissue. Optical properties calculated by arrival time of photon in the detection side in relation to the pulse of the laser.

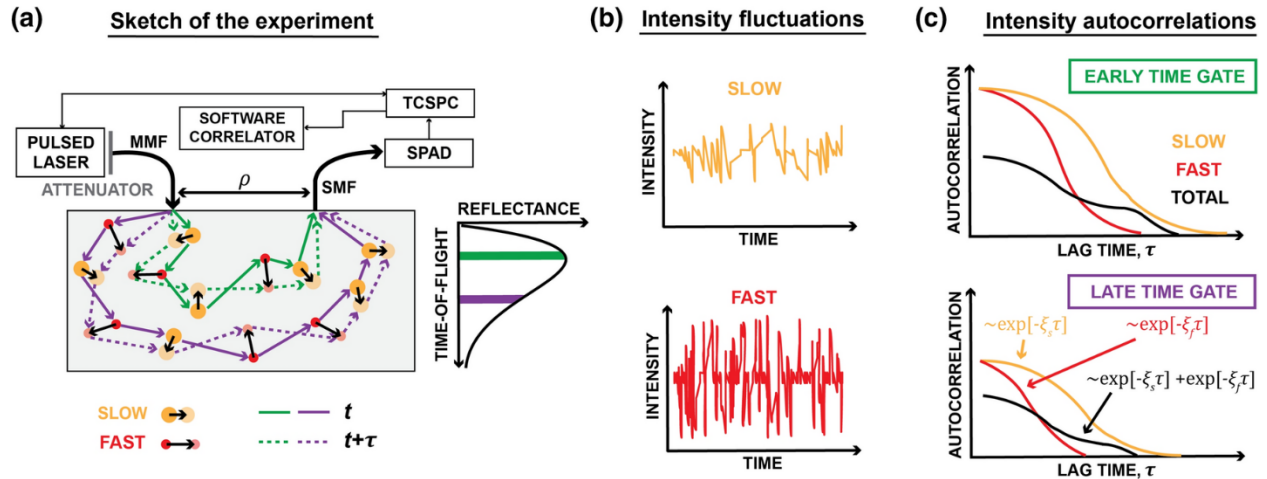


Figure 2.6 Time resolved measurement scheme. a) Schematic diagram of the system. Pulsed laser in synchronization with SPAD detector via time correlated single photon counting (TCSPC) is used to obtain photon arrival time, which is fit to time domain diffusion model to extract optical properties. b) Photon arrival time (early time gate, late time gate) generated by laser pulse corresponds to optical path length in the tissue. Photons that travel shorter pathlength (early time gate) corresponds to shallow depth typically shows slow temporal intensity fluctuations compared to photons that travel longer path length (late time gate). (Samaei et al., 2021).

2.6 Conclusion

This chapter provides conceptual description of different parameters which dictates the light-tissue interaction. Here, characteristics i.e., coherence of various light sources have been discussed. We have also included some fundamental techniques utilizes speckle by tailoring coherence length of the laser in an optical scheme to extract quantitative information of tissue.

Chapter 3: Synthetic Multi-exposure Laser Speckle Imaging¹

3.1 Introduction

In adult human brain metabolism, aerobic glycolysis, consume only ~10-12% glucose but plays a crucial role for neural activity (Liang et al., 2013; Raichle et al., 1970; Vaishnavi et al., 2010), a biomarker of tissue health, is critical for delivering oxygen and nutrients (e.g., glucose) for normal brain metabolism. Local CBF is closely coupled to neural activity, and this laid out foundation of functional neuroimaging techniques (Devor et al., 2012; Kisler et al., 2017). In clinical and research setting, functional imaging of blood flow in cerebral vessels is of paramount importance to understand the normal functioning of physiology, monitor disease progression, and to track treatment (Dunn et al., 2001; Erdener et al., 2019; Parthasarathy, Kazmi, et al., 2010; Venugopal et al., 2019).

Functional imaging of cerebral blood flow based on optical method can be categorized as either tracking of red blood cell (RBC) in time and space (Ishikawa et al., 1998; Roe, 2010) or photon correlation-based techniques (Bandyopadhyay et al., 2005; Boas & Yodh, 1997). RBC tracking techniques involve laser scanning microscopy (Kirkpatrick et al., 2012; Seylaz et al., 1999) or high frame rate RBC photography (Tsukada et al., 2000, 2004). Even though these methods provide absolute flow-ranging from 0.5 mm/s to 20 mm/s, they are limited to small field-

¹ This chapter is adapted from the publication Safi, A. M., Hernandez-Isidro, C., Cini, S., Moka, S., Harrah, M., Passaglia, C. L., & Parthasarathy, A. B. (2021, April). *Quantitative Cerebral Blood Flow Imaging with Synthetic Single-Shot Multi-Exposure Laser Speckle Imaging*. In *Optics and the Brain* (pp. BW3B-4). Optical Society of America. Submitted for provisional patent: US provisional patent application # 63/200,914 (Ashwin B Parthasarathy, Abdul Mohaimen Safi)

of-view (FOV) ~600–1000- μm , due to limitations of point scanning method in case of laser scanning-based microscope (Shih et al., 2012; Takanezawa et al., 2021) and limitation of high framerate at wide field-of-view in case of speed RBC photography method (Tsukada et al., 2000, 2004). Photon correlation-based technique includes Doppler based methods, such as laser Doppler flowmetry, holographic laser doppler imaging, photoacoustic Doppler velocimetry (Brunker & Beard, 2016; Magnain et al., 2014; Steinmeier et al., 2002) and speckle based method such as laser speckle contrast imaging (LSCI) (Boas & Dunn, 2010; Dunn, 2012; Fercher & Briers, 1981) and speckle variance optical coherence tomography (Choi et al., 2016; Liu et al., 2011).

LSCI is an emerging technique that allows label-free imaging of wide-field cortical blood flow dynamics at superior spatiotemporal resolution than conventional Magnetic Resonance Imaging (MRI), Computed Tomography (CT) or Diffuse Optical Tomography (DOT) with relatively simple instrumentation. Hence, LSCI has proven to be a powerful functional imaging tool for both in preclinical (Ayata et al., 2004; Dunn et al., 2001; Durduran et al., 2004; Mangraviti et al., 2020) and clinical research settings (Miller et al., 2022; Parthasarathy et al., 2010; Richards et al., 2017; Yu et al., 2021). However, CBF measured with LSCI methods provide only relative flow information, which makes LSCI an inappropriate tool for longitudinal studies (Ayata et al., 2004). Therefore, quantitative blood flow imaging with speckle became an active area of research. So far, four techniques have been reported to solve this fundamental issue, which are multi-exposure laser speckle imaging (Parthasarathy et al., 2008), frequency-domain laser speckle imaging (FDLSI) (Li et al., 2014), laser speckle flowmetry (Nadort et al., 2013, 2016), and optical speckle image velocimetry (OSICV) (Qureshi et al., 2021). MESI introduces a new quantitative model for blood flow estimation and new instrument, where speckle images are obtained for wide range of exposure times and the multi-exposure speckle images are fit into the model to obtain

quantitative flow. However, due to the complex instrumentation and synchronization, original MESI instrument application is only limited to preclinical studies. For clinical studies, MESI instrument have been modified, and instead of acousto-optic modulator (AOM) a rotating ND filter has been used (Parthasarathy et al., 2010; Richards et al., 2017), to record speckle images in various exposure times, which limits the temporal resolution of the system. However, the MESI model has been proven to be quantitative and has recently been adopted into the diffuse speckle correlation spectroscopy applications (Dragojević et al., 2018; Murali et al., 2020; Murali & Varma, 2020). FDLSI introduces speckle imaging in the Fourier domain to obtain quantitative flow. However, it requires high frame rate camera and is limited to simple studies such as single vessel flow estimation and not suitable for CBF imaging. Laser speckle flowmetry demonstrates a scaling factor to convert speckle contrast to flow value but for different sample this scaling value needs to be recalculated. OSICV, demonstrates flow magnitude and direction without need for calibration or mathematical model. However, OSICV can only work at 532 nm wavelength, where absorption is significant to reduce penetration depth. It also requires high speed camera and only able to provide single vessel information.

In this chapter, we present a simple technique utilizing the speckle ergodicity in the spatial domain to obtain a quantitative, wide-field MESI with a traditional LSCI setup. The technique is termed synthetic multi-exposure speckle imaging (syMESI). syMESI is analogous to single-shot acquisition MESI (sMESI) (Dragojević et al., 2015). However, sMESI, utilizes temporal ensemble averaging, where speckle images are captured with a SPAD detector. Hence, it is better suited for low-resolution images (8x5 pixels). In contrast, in syMESI, relies on spatial ensemble averaging, where speckle images are recorded in low-cost camera and processed spatio-temporally. We validated our approach, by performing *in vitro* flow phantom experiments in microfluidic channels

and by measuring CBF in rodent cortex *in vivo*, mimicking the similar experiments parameters of the “gold standard” hardware based MESI. Furthermore, we demonstrated the application of syMESI with a clinical feasibility via cauterization in rodent brain. To the best of our knowledge, syMESI is the first of its kind to provide quantitative flow information like MESI but with high spatial and temporal resolution.

3.2 Methods

3.2.1 Working Principle of syMESI

When light from a highly coherent source such as laser illuminates a sample (e.g., tissue), backscattered light produces random interference that can be imaged by a camera. This interference, termed laser speckle, is due to light waves travelling multiple paths inside tissue before coherently adding at the detector. For a dynamic sample such as living brain, speckle pattern contains the spatial and temporal information of movement of red blood cells, as a form of blurring in the image. Quantification of this blurriness, widely known as speckle contrast, $K = \sigma_s / \langle I \rangle$, where σ_s local standard deviation of the intensity and $\langle I \rangle$ local mean local intensity of the recorded speckle image, provides visibility of blood flow information in the tissue. Speckle contrast, K, is highly sensitive to camera exposure duration; short exposure times are sensitive to faster flow and longer exposure times provides information about slower blood flow. Multi-exposure speckle imaging (MESI), developed by Parthasarathy et al., 2008 addressed this issue and provided a new speckle contrast model.

$$K(T, \tau_c) = (\beta(e^{-2x} - 1 + 2x)/2x^2)^{1/2}, \quad (\text{Eq.3.1})$$

here, $x = T/\tau_c$, β is a speckle instrumentation factor that depends on wavelength of light, detector pixel size and speckle size, T, is the camera exposure duration and τ_c is the speckle decorrelation time - a quantitative index that is inversely proportional to blood flow. MESI instruments allow

acquisition of speckle images over a range of exposure times (50 μ s to 80 ms), which can be fit to the speckle contrast model to estimate an index of blood flow (τ_c). Considering the effect of static scattering and noise Eq. 3.1. can be updated as

$$K(T, \tau_c) = \left(\frac{\beta \rho^2 (e^{-2x} - 1 + 2x)}{2x^2} + \frac{4\beta \rho (1-\rho)(e^{-x} - 1 + x)}{x^2} + v_s \right)^{1/2} \quad (\text{Eq. 3.2})$$

here, ρ is ratio of dynamic to total scattered light and v_s represents noise in the system.

Unlike MESI, which used hardware components (acousto-optic modulator or neutral density filters) and camera triggering to acquire images at multiple exposure durations, syMESI reimagines same multi-exposure image acquisition as a software process. Our hypothesis based on the foundation of ergodicity of speckle – dynamics and statistics of speckle is similar in space and time (Liu et al., 2021; Parthasarathy et al., 2008; Zakharov et al., 2009). In a speckle image, speckle recorded in each pixel is independent. Therefore, recorded speckle intensity in camera pixel can be binned spatially to yield a synthetic exposure. For example, a speckle image at 4 ms exposure can be synthesized by spatially averaging 4 pixels of an image acquired at 1 ms exposure.

We demonstrate in Figure 3.1., processing scheme of syMESI algorithm. A series of raw speckle images are acquired by the camera at a fixed exposure time. Each of these images can be converted to synthetic multi-exposure images by spatially averaging the camera recorded image.

Raw speckle images at longer exposure can be synthesized by spatially averaging images at shorter exposure. For example, speckle images at 1 ms exposure duration are synthesized by spatially averaging 4 pixels of a 0.25 ms speckle image. This averaging can be accomplished with a 2x2 moving window or by 2x2 binning. Spatially averaging the image with a square window yields a synthetic exposure image. Each pixel of the synthetic image is an average of adjacent pixels of the camera acquired image. By repeating this process for every recorded image, we can synthesize a stream of multi-exposure speckle images. Finally, blood flow information is quantify

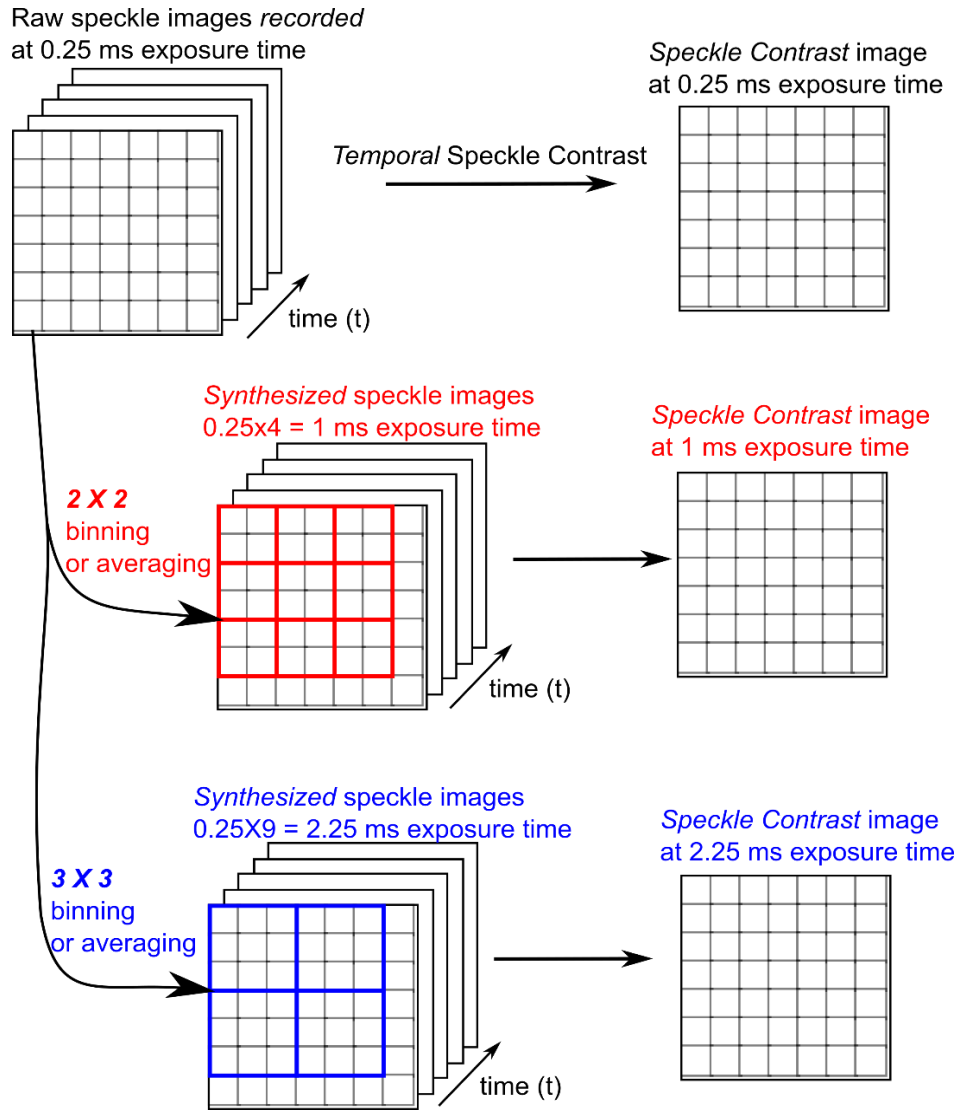


Figure 3.1 Working principle of synthetic multi-exposure speckle imaging (syMESI)

by computing the temporal speckle contrast at each image pixel for all exposure times, i.e., by computing $K = \frac{\sigma_s}{\langle I \rangle}$ at each pixel, where σ_s is the standard deviation and $\langle I \rangle$ is the mean of pixel intensities of sequential images (typically frames). At each pixel, we can thus estimate blood flow index fitting the synthetic multi-exposure data in Eq.3.1 or Eq. 3.2. Note that the speckle contrast can also be computed as spatially, by computing the standard deviation and mean of pixel intensities within a moving spatial window (typically 7×7), as typically performed in

literature.(Briers & Webster, 1996; Draijer et al., 2008; Ramirez-San-Juan et al., 2014; Tom et al., 2008; Yuan et al., 2005)

3.2.2 Optical Setup

Figure. 3.2. shows a schematic of syMESI instrumentation, which is similar to setups traditionally used for single-exposure LSCI. Briefly, a linearly polarized single mode laser diode ($\lambda=785$ nm, 90 mW, Thorlabs) was collimated to uniformly illuminate the sample (tissue phantom, or rat brain,). Backscattered light from the sample was imaged using a custom optical system consisting of a CMOS camera (Basler acA2000-165umNIR) and an objective lens (4X, NA 0.10, Olympus). Speckle images were continuously recorded at a 100 Hz frame rate and 250 μ s exposure time. Synthetic MESI images were computed by spatially averaging the raw single exposure speckle images, with moving windows of different sizes. For example, spatially averaging a 250 μ s speckle image with a 2x2 moving spatial window would yield a synthetic 1 ms exposure image. Synthetic speckle contrast images were then computed by estimating the temporal speckle contrast ($n=100$ frames) at each pixel. The process was repeated for exposures 250 μ s to 25ms.

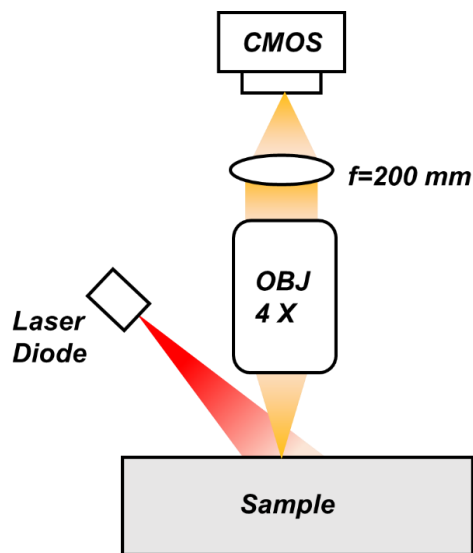


Figure 3.2 Experimental setup for syMESI. Schematic of the imaging system; light from a single mode diode laser illuminates the sample. The back-reflected light is images using custom made 4f imaging system and a CMOS camera.

3.2.3 Microfluidic Phantom Preparation

Tissue simulating microfluidic phantoms were used to test the syMESI algorithm, including phantoms that simulated a thin skull over a flow region. Microfluidic flow phantoms of channel dimension $200\ \mu\text{m} \times 150\ \mu\text{m}$ were designed in Solidworks and fabricated using Somos 9120 high-resolution stereolithography process (Proto Labs, Inc., USA). To mimic tissue properties, PDMS was mixed with Titanium dioxide (TiO_2) by following the recipe described in (Parthasarathy et al., 2008b). Prepared microfluidic channel was bonded with slide glass using plasma bonding technique-performed at USF Nanotechnology Research and Education Center. To mimic flow, a syringe pump (Harvard apparatus, USA) used in conjunction with polyethylene tube (PE tube) was connected to the microfluidic channel and 20% intralipid was pumped through it at varying speeds. Figure 3.3c shows schematic diagram of the microfluidic channel in combination with syringe pump and PE tube. The tissue mimicking microfluidic phantom without thin scattering layer shown in Figure 3.3a. Using a custom mold, a thin scattering layer which mimics the superficial tissue properties was fabricated and bonded with microfluidic sample by following the procedure described in (Parthasarathy et al., 2008). Mold for making $200\ \mu\text{m}$ thick static scattering layer, was fabricated using Watershed XC 11122 high-resolution stereolithography process (Proto Labs, Inc., USA). Figure 3.3b shows microfluidic channel with thin scattering layer.

3.2.4 Animal Model Preparation

For in-vivo experiments, adult male retired-breeder Brown-Norway rats (400-450 g, over a year old) were used in accordance with protocols approved by the Institutional Animal Care and Use Committee at the University of South Florida. Initial anesthesia was induced via an intraperitoneal (IP) injection of ketamine hydrochloride (75 mg/kg) and xylazine (7.5 mg/kg). An incision on the underside side of the left leg was done to expose the femoral vein. The vein was then isolated, and

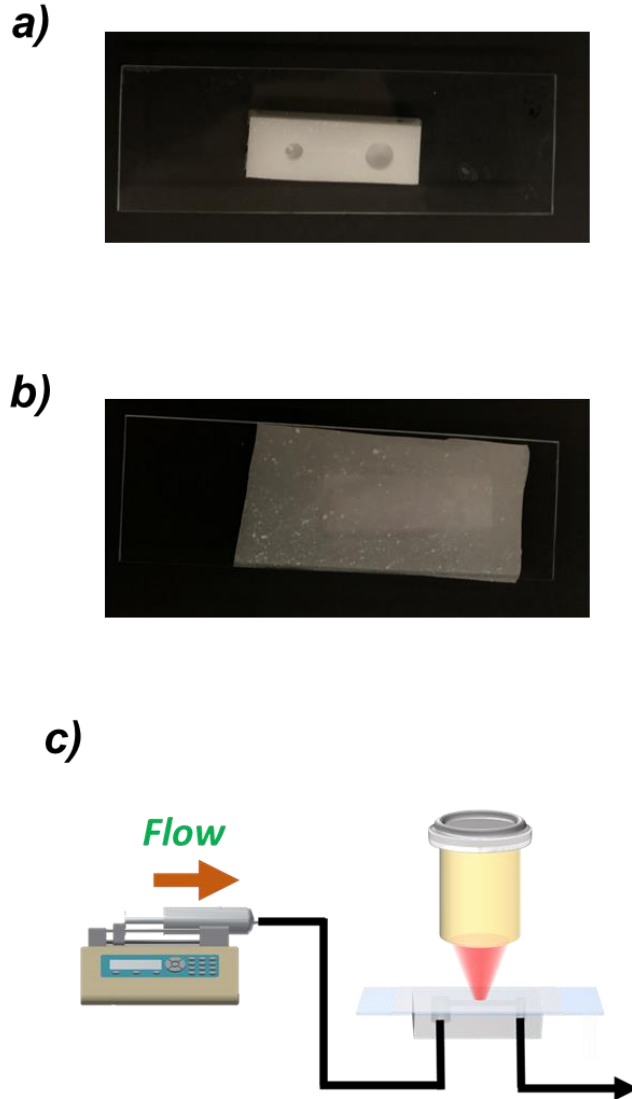


Figure 3.3 Microfluidic channel. (a) Phantom without static scattering layer (b) Phantom with 200 μm scattering layer. (c) Schematic diagram of the experimental setup for flow study (laser not shown)

a small incision was made for insertion of a 25-gauge femoral vein catheter (Instech, Plymouth Meeting, PA, USA). Anesthesia was then maintained by intravenous infusion of ketamine (30 mg/kg/hr) through the femoral vein catheter. Body temperature and heart rate were recorded with a rectal thermometer and ECG electrodes, respectively, and logged with a custom LABVIEW program (National Instruments, Austin, TX USA). Heart rate and body temperature were monitored and maintained within physiological levels by placing the animal on a heating pad

(Stryker T/Pump Professional Model TP700 set to 37°C) and adjusting the infusion rate of ketamine with a syringe pump (Harvard Apparatus PHD ULTRA). A subcutaneous bolus of dexamethasone (1 mg/kg) was given to prevent cerebral edema during the experiment. The rat's head was secured in a stereotaxic apparatus to perform a craniotomy. To expose the skull, an incision was made along the midline of the head after the hair was trimmed. The overlying tissue on the skull was cleared and the skull was cleaned with 3% hydrogen peroxide. A hole was drilled with a 5 mm diameter drill bit (Fine Science Tools, Item No. 18004-50) attached to a Dremel tool (Dremel 200 Series Two Speed Rotary Tool) lateral to the midline, on a parietal plate, to avoid damaging major vessels below the sagittal suture. During drilling of the hole, a small amount of saline was used on the surface of the skull to remove some heat caused by friction between the drill bit and the skull. Fine tip curved forceps were then used to remove the remaining skull fragment. There was minor bleeding after removing the skull fragment which was cleaned with gauze pads. Saline was also used to keep the exposed brain moist and helped with image quality. The rats were euthanized at the end of the experiments with an IP bolus of Euthasol (50 mg/kg) euthanasia solution.

3.3 Results

3.3.1 Proof of Principle Experiments in Microfluidic Flow Phantom

To validate syMESI approach, we designed a microfluidic flow phantom study similar to the original MESI experiment. A microfluidic channel with no scattering layer was illuminated by coherent laser light, while we acquired a series of 200 raw speckle images each at 250 μ s exposure duration, while the flow pump was operated to pump intralipid through the channel at speeds of 1 to 10 mm/s. Each raw speckle image was converted to synthetic exposure images, and subsequently speckle contrast images at each exposure time. Representative synthetic multi-

exposure speckle contrast images are shown in Figure. 3.4 (a). The decrease in speckle contrast with exposure duration is evident in these images, similar to what one would obtain with original hardware based MESI. A small region of interest (100×100 pixels) was selected within the flow channel to quantify the speckle variance (average within the ROI). For each speed, ($n=3$ trials) were performed and data was taken at 5 min interval for each speed, this allows flowing intralipid to reach defined flow speed throughout the microfluidic channel. Figure. 3.4 (b) shows a plot of the speckle variance in the flow channel as a function of exposure duration for each speed. The filled circles are the speckle variance values. The data for each speed is fit to the multi-exposure speckle model to estimate the instrumentation factor β and the flow index τ_c . Figure 3.4 (b) clearly shows that the speckle variance data obtained from synthetic method fits well with the MESI model for wide range of flow rate. Figure. 3.4 (c) shows a plot of the relative change in blood flow using a baseline speed of 2 mm/s. Relative blood flow was calculated as the ratio of τ_c at baseline, to the measured τ_c (note that flow is inversely proportional to τ_c). Individual data points and estimation errors are shown. Figure. 3.4 (c) shows that the measured relative flow (with τ_c) linear with relative speed of intralipid set by the pump. We can observe that for high speed (> 6 mm /s) linearity breaks down. For estimation of relative flow standard deviation ($\leq \pm 0.11$) in case of low-speed range. The dynamic range of speed could be improved by acquiring data at shorter exposure times ($\sim 1 \mu\text{s}$) and higher frame rate (> 100 fps). This is an important finding that reaffirms that syMESI reproduces the quantitative imaging nature of hardware MESI. Specifically, this result shows that with syMESI approach we can transform traditional LSCI to count for underestimation of large flow changes.

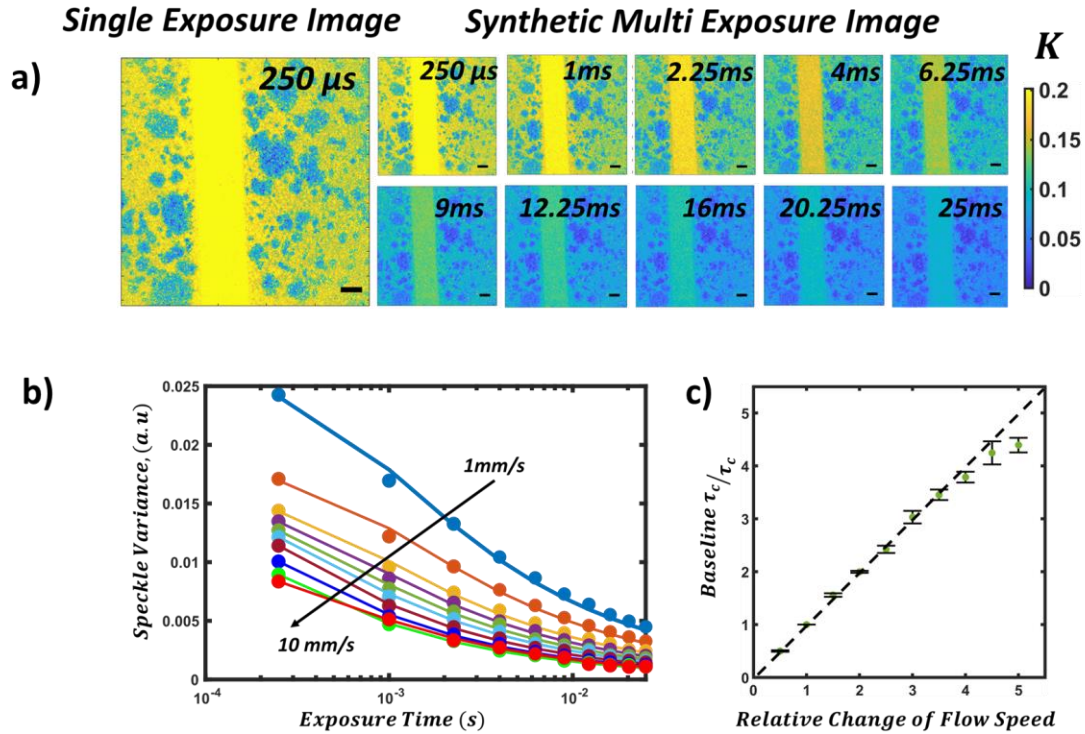


Figure 3.4 syMESI on microfluidic flow phantom study (a) Single-exposure image at 250 μ s and syMESI images at 250 μ s to 25 ms exposure durations - flow phantom (scale bar: 100 μ m). (b) Fit of synthetic speckle variance data to the MESI model. (c) Plot of relative correlation time to relative change of flow.

3.3.2 Proof of Principle with Static layer

One of the significant advances that MESI made was to quantitatively image in the presence of static scatterers. Here, we validate that syMESI can also estimate flow quantitatively in the presence of scattering layer. According to section 3.2.3, a microfluidic channel, and a static layer of 200 μ m thickness was prepared. A series of 200 raw speckle images each at 250 μ s exposure duration was acquired while pumping intralipid through the channel at speeds of 1 to 5 mm/s. Similar to microfluidic phantom without static layer, section 3.3.2, each raw speckle image was converted to synthetic exposure images, and subsequently speckle contrast images at each exposure time. A small region of interest (100 \times 100 pixels) was selected within the flow channel to quantify the speckle variance (average within the ROI). Figure 3.5a shows representative results

of synthetic speckle variance curve for two level of static layers and two speed. The open circles plot the speckle variance as a function of exposure time for 2 mm/s (blue) and 5 mm/s (red) speeds in the phantom without static scattering layer ($\mu'_s = 0cm^{-1}$). Similarly, the filled squares plot the speckle variance as a function of exposure time for 2 mm/s (blue) and 5 mm/s (red) speeds in the phantom with $200\mu m$ thick static scattering layer ($\mu'_s = 4cm^{-1}$). In each case, the solid and dashed lines are fits of the data to the multi-exposure speckle model. We can see that, speckle variance generated by the syMESI method fits well with the MESI model. Similar to Figure 3.4c, Figure 3.5b shows a plot of the relative change in blood flow (measured as a ratio of τ_c s) with relative change in speed of the intralipid through the flow channel, with 1 mm/s as baseline. Figure 3.5b clearly shows that the linearity of flow changes is retained over a large range even the presence of static layer. These results further bolster our claim that syMESI algorithm can provide similar characteristics as traditional hardware based MESI.

3.3.3 *In vivo* Demonstration of Quantitative Assessment of CBF

The main goal of this experiment to assess the how well synthetic MESI represents physiological changes in an animal model. Briefly, a rat was prepared for imaging using methods described in Section 3.2.4. Raw speckle images were obtained at 100 Hz at $250\ \mu s$ exposure duration. Each raw speckle image was converted to synthetic exposure images, and subsequently speckle contrast images at each exposure time by performing temporal contrast on 200 images. Figure 3.6. depicts *in vivo* results at baseline condition. Bright field image and corresponding synthetic MESI ICT image shown in Figure 3.6a and 3.6b respectively. The MESI ICT image is a quantitative map of speckle inverse correlation times (ICTs, $1/\tau_c$), estimated by fitting the speckle variance as a function of exposure time to the speckle model at each pixel of the image. To understand the effect of vessel size and tissue, vessels of different sizes and tissue paranchyma

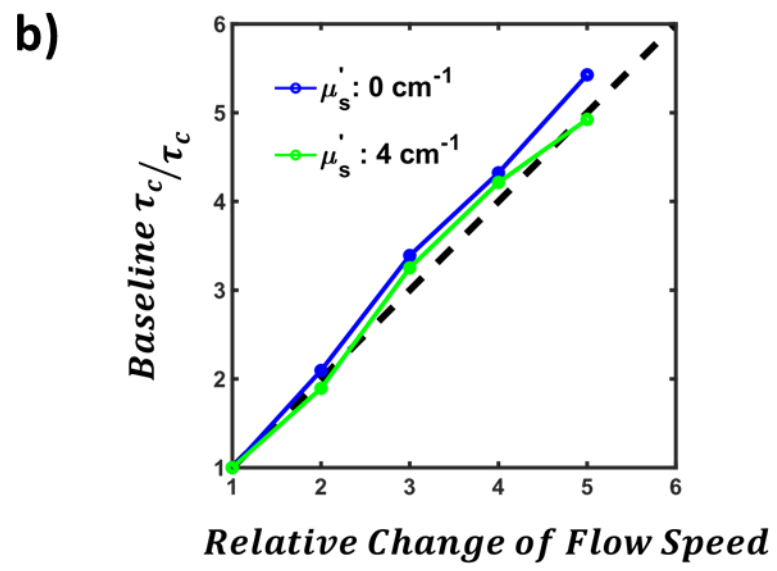
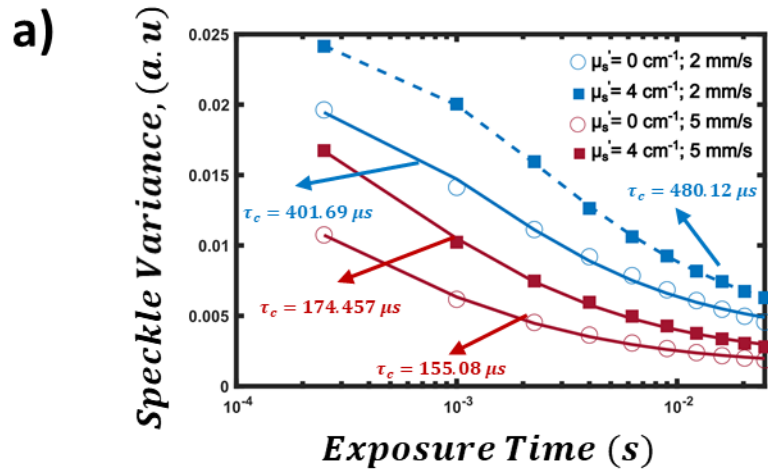


Figure 3.5 syMESI on the effect of static layer. (a) Synthetic multi-exposure speckle contrast data from two samples fit to the multi-exposure speckle model. Speckle variance as a function of exposure duration for two different speeds and two levels of static scattering. (b) Plot of relative correlation time to relative speed for different level of static layer properties. Baseline flow – 1 mm/sec.

selected as ROIs, in the synthetic MESI ICT frame. Figure 3.6c shows the speckle variance curve for each of the ROI. These curves demonstrate data obtained by synthetic MESI followed expected physical trend. For the ROIs in bigger vessel shows faster decays and the smaller vessel shows slower decays as expected. ROI in parenchyma show the slowest decay. Flow conservation

analysis have been performed to further bolster the validation of synthetic MESI to measure quantitative blood flow. A bifurcated figure vessel was chosen, Figure 3.6 (b, d). Based on the diameter of the vessel, a parent vessel two daughter vessels were identified and designated as p, D₁ and D₂ respectively. According to flow conservation theory, sum of flow in the two smaller diameter daughter vessels (D₁, and D₂) should be equal to flow in the large diameter parent vessel (p). We can verify this by measuring the error of flow between parent vessel and two daughter vessels, using the equation described in literature (Richards et al., 2017) as-

$$\% Error = \left| \frac{D_1 ICT_1 + D_2 ICT_2 - D_p ICT_p}{D_p ICT_p} \right| \times 100, \quad (\text{Eq.3.3})$$

here, D_p, D₁, D₂, are the diameters of the parent and two daughter vessels respectively. ICT_p, ICT₁, ICT₂, are the speckle inverse correlation time of parent and two daughter vessels respectively.

In bifurcated vessel segment shown in Figure 3.6 b, n=3 segments (1-1', 2-2', 3-3') were taken for each vessel (parent, daughter1 and daughter 2). Diameters for each vessel segment was measured using ImageJ (Schneider et al., 2012). Baseline flow in each segment was calculated by multiplying the diameter with the respective speckle inverse correlation time (ICT) (Kazmi et al., 2013). Finally, using Eq. 3.3, the percentage error for the flow conversion was measured for each segment. Results are shown in Figure 3.6 (b, d), where the bar graph clearly demonstrates that in each segment, flow conservation is maintained; and average percentage of error for flow conservation across the three segments was calculated to be 5.8±0.5%. This demonstrates synthetic MESI can provide quantitative flow.

3.3.4 Fidelity of CBF Changes with an *In vivo* Cautery Experiment

Synthetic MESI was performed before and after vessel cautery to illustrate the feasibility of clinical application in synthetic MESI to evaluate blood flow changes during surgery. Briefly,

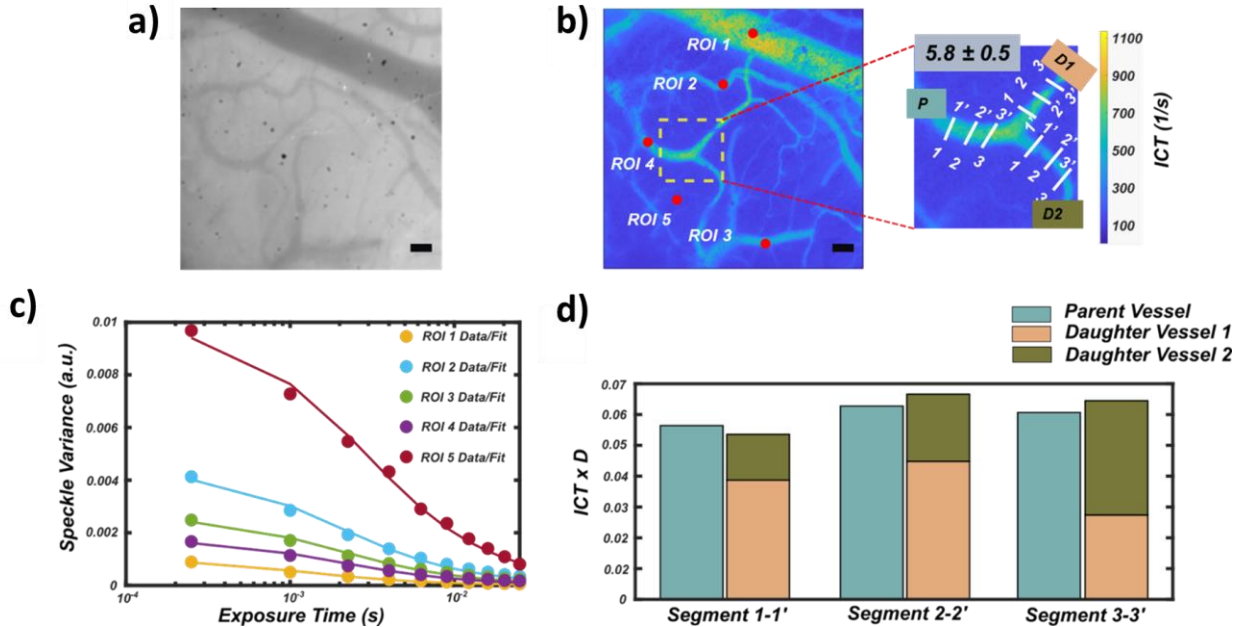


Figure 3.6 syMESI of blood flow in a rodent brain *in vivo*. (a) Bright field image of cerebral blood vessel of exposed rat cortex. (b) Corresponding synthetic MESI image. Higher ICT values indicate faster flow. The numbered ROIs used for analysis are shown in red in the synthetic MESI ICT frame. (c) Synthetic MESI-computed speckle visibility curves for the corresponding five ROIs are shown on a semi-logarithmic scale. (d) Conservation of flow analysis for three-way vessel branches, for the (yellow dotted) rectangular ROI. synthetic MESI computed percentage of error due to the combination of flow from two daughter vessels (D1, D2) and the parent vessel (P) is shown in the inset of Figure 3.6(b). All scale bar: 100 μm .

a rat was prepared for imaging using methods described in Section 3.2.4. A vessel of interest was identified using the bright field image. Raw speckle images were obtained at 100 Hz at 250 μs exposure duration. After performing baseline imaging, vessel of interest was carefully cauterized manually with an electric cautery pen without damaging surrounding vessels. After cautery, similarly, raw speckle images were obtained at 100 Hz at 250 μs exposure duration. In post processing for both before and after cautery, each raw speckle image was converted to synthetic exposure images, and subsequently speckle contrast images at each exposure time by performing temporal contrast on 200 images respectively. Speckle inverse correlation time (ICTs, $1/\tau_c$), estimated by fitting the speckle variance as a function of exposure time to the speckle model at

each pixel of the image for both before and after cautery. Figure 3.7a shows synthetic MESI ICT frame before and after cautery. After cautery synthetic MESI clearly shows reduction of flow in the location of cautery. The location further way from the cautery retains their flow with minimal changes. Figure 3.7b shows the corresponding speckle variance curves before and after cautery in an ROI within a blood vessel; 50 % change in cerebral blood flow can be observed after the cautery.

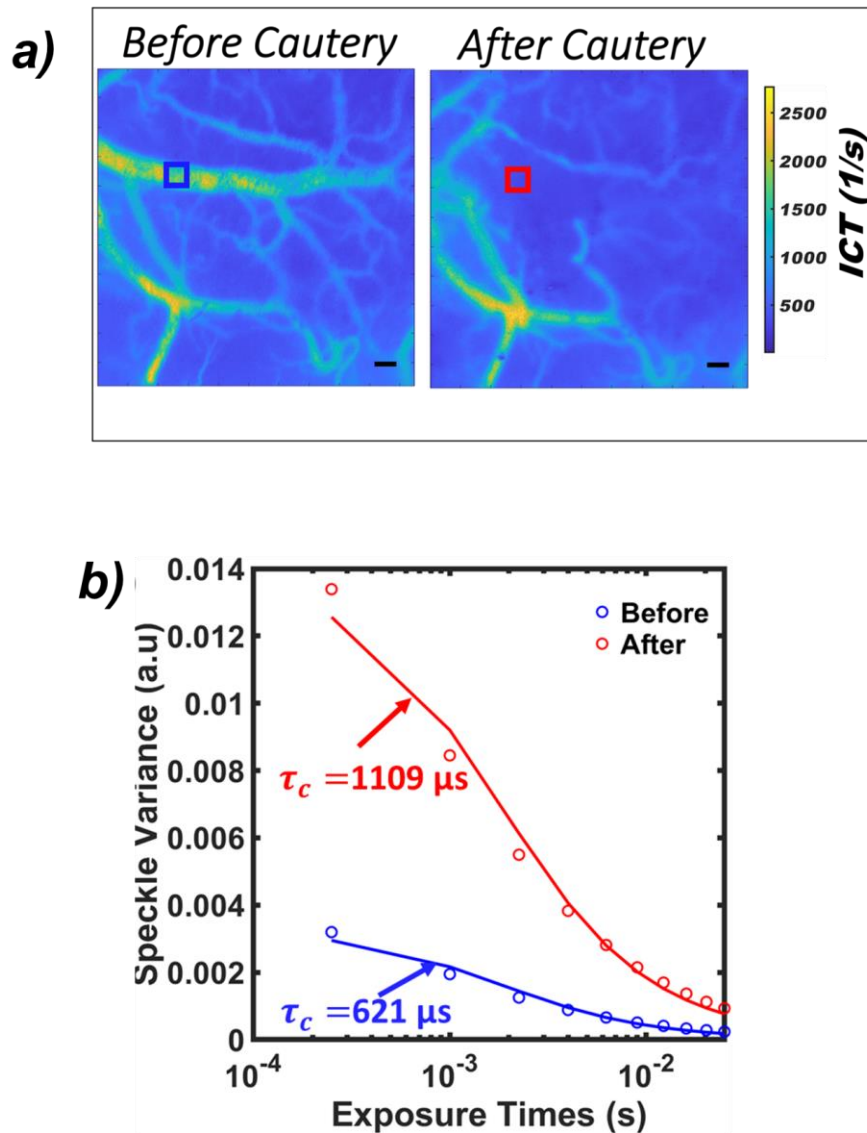


Figure 3.7 Application of syMESI during cautery in rodent model. (a) syMESI measured speckle decorrelation time maps of flow before and after cautery of a cerebral blood vessel in an anesthetized rat (scale bar: 100 μm). (b) Corresponding speckle visibility curves for the selected ROI highlighting a ~50% reduction in cerebral blood flow

3.3.5 High Speed Measurement to Evaluate Pulsatility of Flow

Here, we investigate the capability of high-speed acquisition of syMESI approach. Traditional hardware based MESI method limited to acquisition rate 30 fps (frame per second) due to the complexities of syncing the laser modulation to time gating of the camera. syMESI is completely software dependent, hence acquisition rate is limited only by the camera. For demonstration, we acquired images at 100 fps on a rodent cerebral cortex at baseline condition. Each raw speckle image was converted to synthetic exposure images, and subsequently speckle contrast images at each exposure time. To preserve the temporal resolution, moving average performed using 10 images which also retain the statistics of temporal speckle contrast. Figure 3.8 shows representative syMESI speckle contrast images at different exposure times (Figure 3.8a) and a syMESI ICT image (Figure 3.8b). A 10 second time series plot of selected ROI which is on the vessel (indicated by red square) on Figure 3.8b is plot in Figure 3.8c. We can clearly see the pulsatile nature of the flow. This clearly indicates, syMESI can overcome the temporal resolution bottle neck of traditional MESI.

3.4 Feasibility of Synthetic MESI Approach in Diffusion Regime

Several recent studies have adopted laser speckle imaging to obtain blood flow from deep tissue regions by performing measurements in the diffusion regime. These studies leverage the simpler instrumentation offered by speckle imagers as an alternative to more expensive diffuse optical devices, and measure blood flow using diffuse speckle contrast analysis (DSCA), typically at a single exposure time, usually (~ 0.2 ms). Here, speckle from diffuse illumination of tissue, (usually with a laser source 1-2.5 cm away) is directly imaged on the CCD sensor in case of spatial DSCA, or via single mode fiber to highly sensitive EMCCD camera for temporal DSCA (Bi et al., 2013, 2020; Mazdeyasna et al., 2018; Zhao et al., 2021). Blood flow information is obtained by

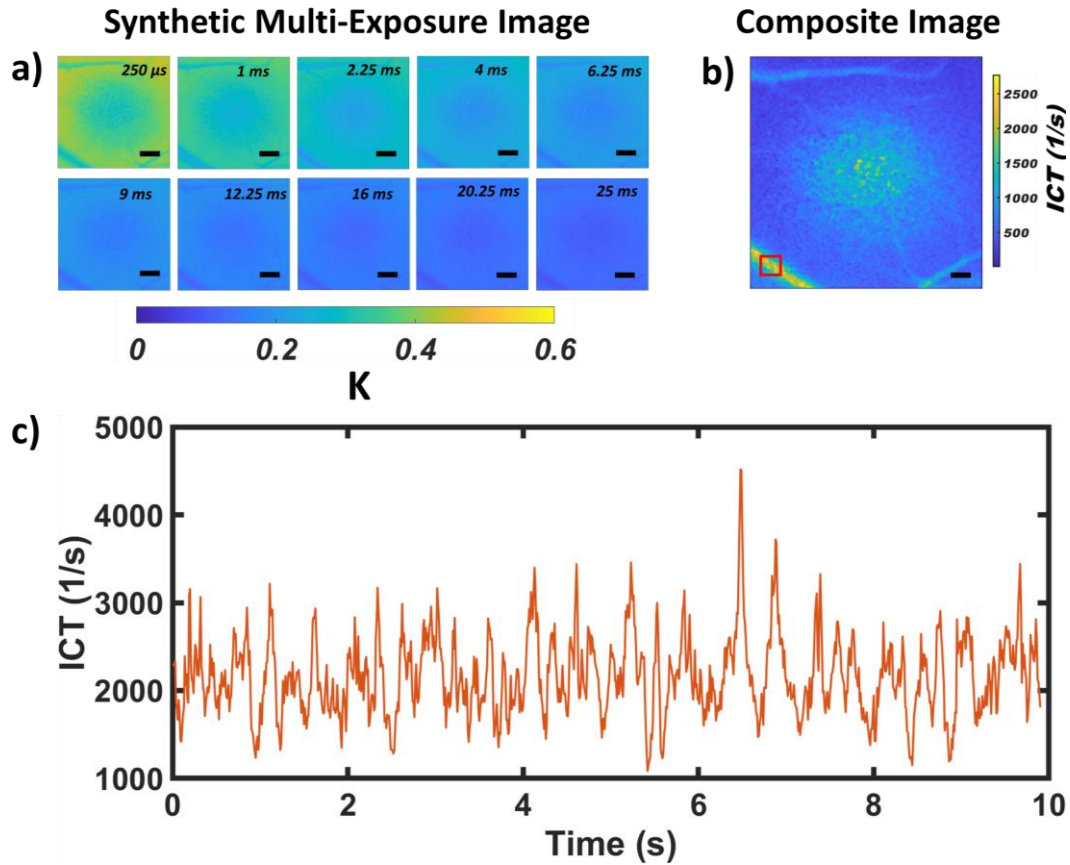


Figure 3.8 Pulsatility of flow. (a) syMESI images at 250 μ s to 25 ms exposure durations acquired at 100 fps. b) Composite ICT image, lower ICT value indicates slow flow and higher ICT value indicates faster flow. c) Time series ICT value for the selected ROI (indicated by red square) shows pulsatile nature of flow.

simply calculating $1/K^2$, which is qualitative rather than quantitative. Recently, MESI-DSCA has been reported (Liu et al., 2017); however, this technique is limited to phantom study as it requires manually changing exposure time and it is not suitable for detecting fast blood flow change. Durduran's group in ICFO, recently developed SCOS (Dragojević et al., 2018) and SCOT (Varma et al., 2014), where multi-exposure speckle contrast K obtained synthetically by temporally binning images acquired using an expensive SPAD camera. Then the multi-exposure K fitted to a model based on Diffuse Correlation Spectroscopy (DCS) theory.

In this section, we provide some initial results which shows potential of syMESI approach to quantify deep tissue blood flow with an inexpensive setup.

3.4.1 Optical Instrument

A schematic of the optical system shown in Figure 3.9. Light from a linearly polarized CW single mode laser diode (L820P200 - 820 nm, 200 mW, Ø5.6 mm, Thorlabs) is collimated using an aspheric lens. The collimated beam is coupled to a multimode fiber (M45L01 - Ø400 µm, 0.50 NA) and connect to a custom-made probe. At source distance separation 1.5 cm, backscattered diffuse light from the sample was collected by multimode fiber (M59L01 - Ø1000 µm, 0.50 NA). Output beam from the fiber is collimated by an aspheric lens (A397TM-B - $f = 11.00$ mm, NA = 0.3) and focused by a 40X objective lens on to a CMOS camera sensor (Basler acA2000-165umNIR). To demonstrate the feasibility of our approach, we performed *in vivo* arm-cuff occlusion study on a healthy subject. All experimental protocols were approved by Institutional Review Board at the University of South Florida. Briefly, probe was placed on the volunteer's forearm. Power measured from the source probe was 45mW, which is well within safely limit of minimum skin exposure (Widginton, 1986) . A blood pressure cuff was placed on the subject's bicep. After baseline (1min), the pressure cuff was inflated to 200 mmHg for 1 minute. When the pressure cuff was released, the recovery of the blood flow was recorded for 1 Minutes. To measure the deep tissue flow, speckle images (128×128 pixels) were continuously recorded at a 30 Hz frame rate and 250 µs exposure time which yield 5400 raw speckle images. Each raw speckle image was converted to synthetic exposure images, and subsequently speckle contrast images at each exposure time by performing moving temporal contrast on 30 images.

3.4.2 Detecting Deep Tissue Blood flow with Synthetic MESI

Figure 3.10 depicts the key results for the validation of our approach for *in vivo* arm cuff occlusion of a healthy subject. Briefly, synthetic speckle variance curve, obtained by performing syMESI approach each raw images, were fit to a diffusion model described in literature

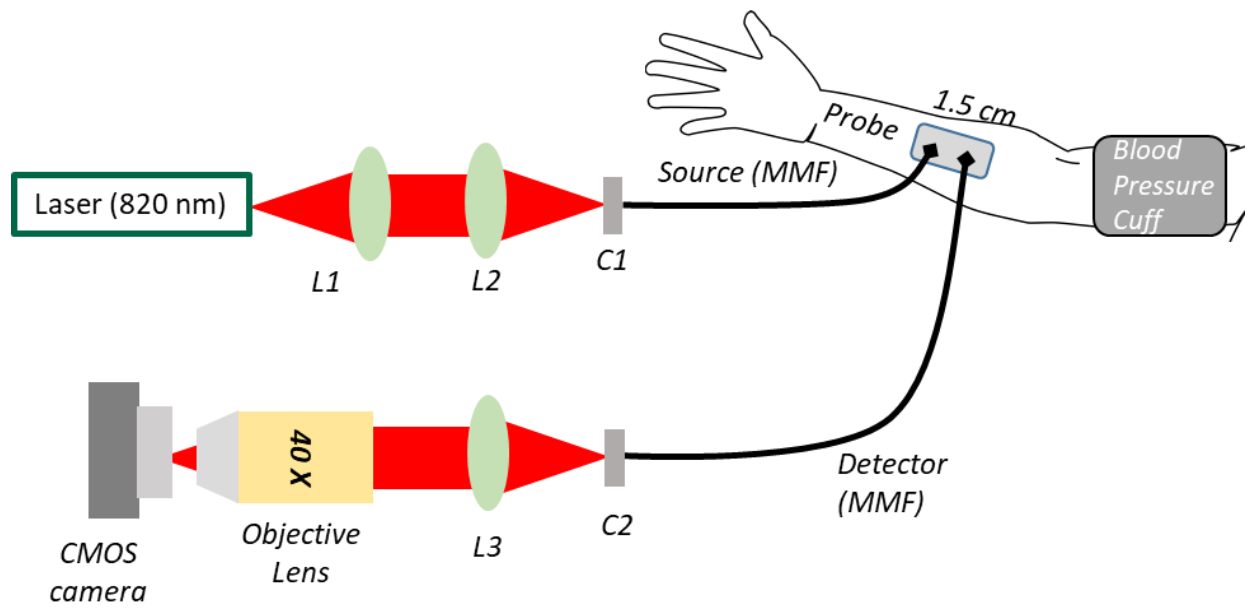


Figure 3.9 Schematic diagram of experiment for synthetic multi-exposure speckle imaging applied to measure deep tissue blood flow with diffuse speckle contrast analysis (DSCA)

(Dragojević et al., 2018). During occlusion we can see higher speckle variance in early exposure time compared to baseline and recovery period. It is expected during occlusion period, as there is less or no blood flow, speckle shows less fluctuation both temporarily and spatially as a result of high speckle variance observed and speckle variance curves decay slower than baseline and recovery period. Error value for curve fitting, in case of baseline ($\sim 1 \times 10^{-4}$), occlusion ($\sim 3 \times 10^{-3}$), recovery ($\sim 1 \times 10^{-3}$). Typical DSCA cannot provide speckle variance curves (speckle variance as a function of exposure duration) as it only acquires images at a single exposure duration. While our method provides speckle variance curves similar to the typical variance curves for multi-exposure method. This suggests that our method can detect flow changes similar to SCOS (Dragojević et al., 2018). Figure 3.11 shows a plot of relative blood flow as a function of time through the course of the experiment. Relative blood flow was calculated by normalizing the time course of blood flow index to the blood flow index at baseline. We can observe nearly 90% blood flow drop. Compare to DSCA (direct image based or single mode fiber based) and SCOS

instrument (direct image based) in our proposed method we used large core multi-mode fiber to capture detected signal. Use of multimode fiber allow us to detect multi-speckle at the low cost sensor thereby increase the signal to noise ratio (SNR) (Liu et al., 2021). This also make the system more sensitive, hence we can observe fluctuations in Figure 3.11.

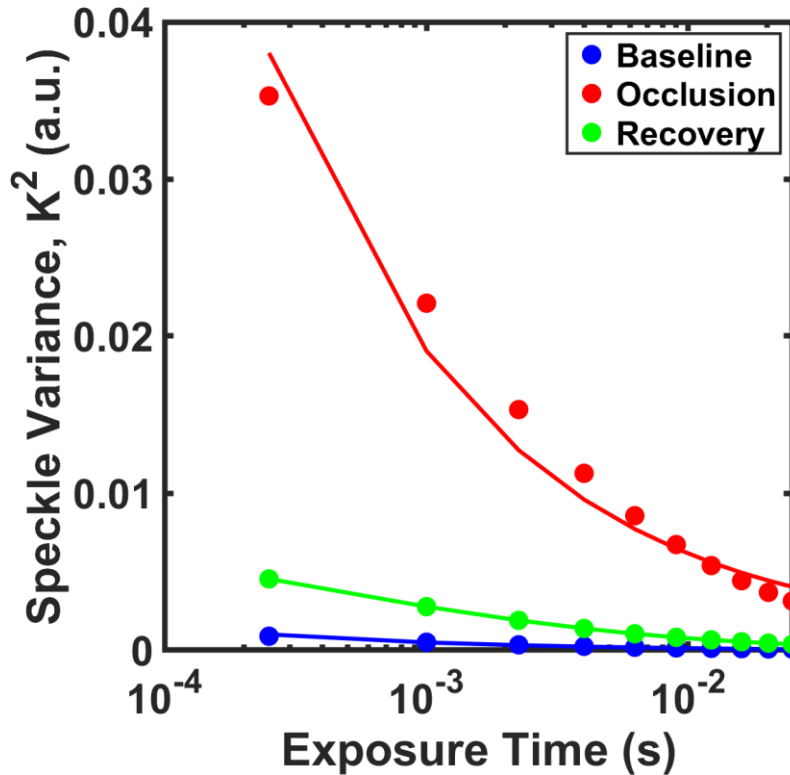


Figure 3.10 Validation of syMESI algorithm in DSCA setup. Speckle variance data measured from the forearm during the baseline (blue), occlusion (red) and recovery (green) as a function of synthetic exposure time (range 250 μ s to 25 ms).

3.5 Discussion

We reported a novel speckle image processing algorithm by exploiting the spatial ensemble averaging of the speckle in the 2D camera sensor. Our syMESI reproduces speckle variance curve similar to traditional MESI. This facilitates us to synthetically perform MESI measurement with traditionnel simple LSCI instrument.

Synthetic multi exposure speckle imaging previously reported in the literature is based on temporal sampling approach, which requires short interframe delay to capture the speckle

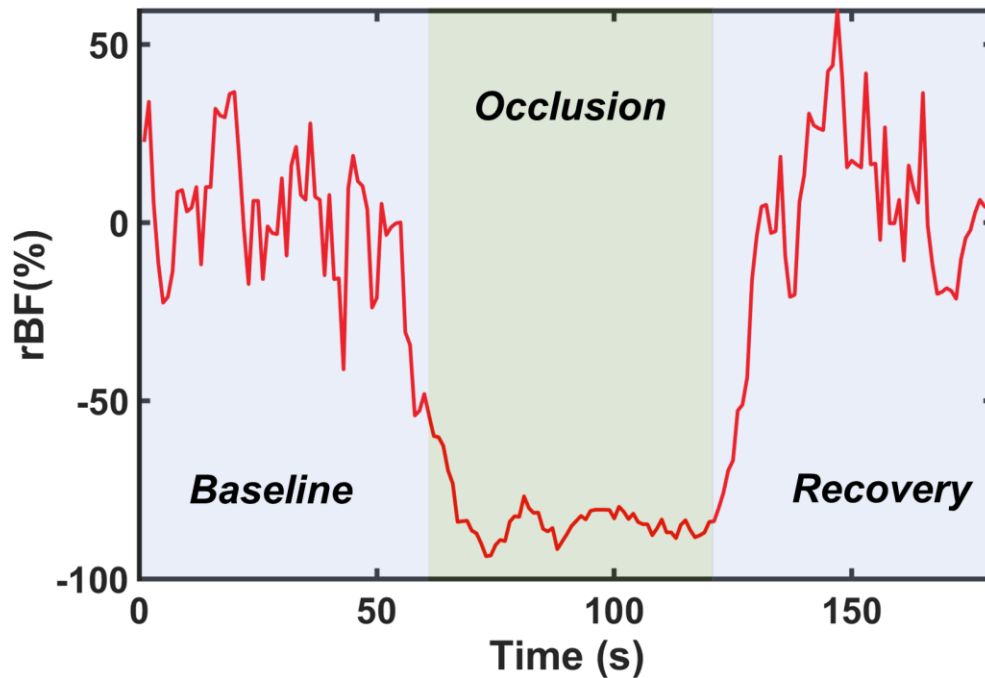


Figure 3.11 Measurement of %rBF by syMESI algorithm using DSCA systems during arm cuff occlusion protocol

decorrelation. For example, Dragojević et al., 2015 used a high speed single photon avalanche detector (SPAD), which allows zero readout noise and negligible inter frame delay to capture the speckle dynamics, albeit at a low spatial resolution (8×5 pixels). Hultman et al., 2018; Sun et al., 2015 have demonstrated high frame rate (> 1 kHz) imaging using FPGA with CMOS sensor for temporal sampling, their approach reduces the interframe delay in order of few μ s, hence allowing high spatial resolution. More recently, Chammas & Pain, 2022 showed, imaging with a CMOS sensor utilizing 1 ms exposure time and 46 fps (frame per second), with temporal binning to obtain synthetic MESI. They validate their approach with hardware based MESI approach. However, their application limited to phantom study as their temporal resolution is 430 ms for full frame. This may not be feasible for *in vivo* blood imaging as speckle decorrelation time shorter than 430 ms.

Recently, Hong et al., 2021 derived a new robust model based on the laser speckle auto-

inverse covariance using a low-cost CMOS sensor. They demonstrated that analysis based on new model allows independence from the statistical sample size, speckle size, static scattering and detector noise. Hence, processing data both on temporal scheme and spatial scheme provide similar quantitative information. Even though this model works on single exposure time (for animal- 10 ms), but it does not provide correction for static scattering, noise like our syMESI approach; hence it is prone to error at high flow. Siket et al., 2021 proposed new instrumentation, time varied illumination LSCI (TVI-LSCI), where laser intensity is modulated in binary fashion at finite pulse time and constant intensity, hence increase the sensitivity of the dynamic range. Even though, the idea is similar to hardware based MESI, optical modulation rather electrical modulation performed. But this requires characterization of laser to maintain the coherence length, and noise during modulation. Also, the results are still in preliminary stage where effect of static scattering and effect of modulation to change of cerebral blood flow, especially quantitative baseline flow estimation have not been addressed in comparison to our syMESI approach. Wang et al., 2019 presented a calibration approach, where both temporal and spatial speckle contrast speckle estimated for a single exposure duration. However, detailed velocity distribution is not possible by this approach, which syMESI approach can provide. Similarly, Wang et al., 2017 presented a calibration approach, where, using single short exposure duration 0.02 ms provide same dynamic range estimation as MESI. However, for different sample calibration procedure needed to be recalculated hence this procedure may not be suitable for longitudinal study.

The primary advantage of syMESI is its ability to transform any existing single exposure speckle image into multi-exposure image without performing experiments. This paves the way for analysis of any both preclinical and clinical speckle image and extract quantitative information. However, we note that, until recently, most speckle imaging with traditional LSCI setup performed

at exposure duration usually, 5ms especially for CBF imaging which provided maximum sensitivity (Yuan et al., 2005). However, as MESI operates on (50 μ s to 80ms), our syMESI method will regenerate MESI image if the speckle images are captured at optimal short exposure duration (Kazmi et al., 2014).

The instrumentation for the synthetic MESI approach presented here is extremely simple; the instrument requires only a CMOS/CCD camera and illumination from a single mode laser. Any low-cost camera (e.g., web cam) (Richards et al., 2013) with such as conventionally available image sizes (as little as 1 megapixels), bit depths and light sensitivities can be used. There are no requirements for specialized sensor technologies (such as APD arrays), cooling or image intensifications – the technique will be shot-noise limited.

Traditionally, acquisition of MESI image required time-gating of laser using acousto-optic modulator or rotating filter wheel which makes the instrumentation bulky and slow for video rate imaging. while other temporal ensemble-based method utilizes high framerate camera to improve the temporal resolution sacrificing spatial resolution. For our method a high frame rate camera is not required, as a result, our approach can be used to perform quantitative video rate multi-exposure speckle imaging (about 10 times faster than current state of the art) with a normal low cost camera.

We note that, we could not achieve lowest exposure time (32 μ s) due to the low quantum efficiency of our CMOS camera (Basler acA2000-165umNIR) at wavelength (785 nm). This can be overcome by using wavelength of 633 nm which provide highest quantum efficiency (~60%). However, to achieve short exposure time and perform syMESI in the near infrared range we believe, CMOS technology needed to be upgraded for providing highest quantum efficiency in that regime. Note that this may not be a critical limitation, as low exposure times of 100 μ s may

be sufficient.

Critically, the innovation of syMESI facilitates intraoperative quantitative fast blood flow imaging by only using low-cost laser diode (~34 USD) as an add-on to the surgical microscope. We believe, syMESI may prove to be suitable candidate surgical work, which will enable surgeons to assess vascular flow in the surgical field of view in dye-free, robust manner.

For future directions, we would like to investigate multi-wavelength syMESI approach, which will allow simultaneously real-time acquisition of quantitative fast blood flow and oxygen consumption. Moreover, a portable, miniaturized syMESI instrument would be interesting to study functional imaging of awake animal (Miao et al., 2011).

Chapter 4: Heterodyne Synthetic Multi-Exposure Laser Speckle Imaging²

4.1 Introduction

Laser Speckle Imaging (LSI) is a robust noninvasive optical technique that has been widely used to directly image blood flow dynamics in tissues microvasculature utilizing the intrinsic contrast of red blood cell motion (Boas & Dunn, 2010). Unlike point scanning method such as Laser Doppler Imaging (LDI), LSI offers wide-field imaging with superior spatiotemporal resolution (Senarathna et al., 2013). Hence, LSI has been widely used to quantify blood flow in skin (Carvalho Brinca et al., 2021; Chen et al., 2021; Lazaridis et al., 2022; Teng et al., 2022), retina (Calzetti, La Morgia, et al., 2022; Calzetti, Mursch-Edlmayr, et al., 2022; Ikemura et al., 2022; Kase et al., 2022), and brain (Guilbert & Desjardins, 2022; Miller et al., 2022; Sullender et al., 2022; Zeng et al., 2021) . Due to relatively simple, inexpensive setup and high spatial and temporal resolution at single vessel resolution, in recent decades, LSCI become a popular tool for imaging cerebral blood flow (CBF) in both preclinical animal models and intraoperative clinical settings.

We have previously described the instrumentation and working principle of laser speckle contrast imaging in sections 1.1 and 3.1. Briefly, laser speckle is the coherent addition of light waves that have traveled multiple pathlengths through tissue. Moving particles within the imaging

² Part of this chapter accepted in Safi, A. M., & Parthasarathy, A. B. (2022, April). *Quantitative Blood Flow Imaging at Photon Shot Noise Limit with Heterodyne Synthetic Multi-Exposure Laser Speckle Imaging*. Optical Society of America. Submitted for US Provisional patent application # 63/265,312 (Ashwin B Parthasarathy, Abdul Mohaimen Safi)

volume impart spatial and temporal fluctuations in the speckle pattern, which are quantified using as a speckle contrast to estimate blood flow. Of particular relevance to this chapter, we note that the light fields that interfere to cause laser speckle all emerge from the sample; thus we term the traditional laser speckle imaging as *homodyne* laser speckle imaging.

Even though LSCI can provide good measures of relative flow, it cannot quantitatively measure baseline flows; we have previously detailed the limitations of traditional LSCI in section 3.1. These limitations have prevented comparisons of blood flow images across individuals, between species or across different studies. One method to overcome these limitations is to employ multi-exposure laser speckle imaging (MESI) (Parthasarathy et al., 2008) to image blood flow, which enables quantitative baseline flow measurement. However, MESI suffers from two critical limitations. One, it requires complex and bulky instrumentation, and two, it requires images to be acquired at lower camera exposure duration, which necessitates high laser powers or sensitive camera as imaging is limited by the photon shot noise at lower exposure time. In chapter 3 of this dissertation, we introduced synthetic multi-exposure imaging (syMESI) a new software-based approach which relaxes the instrumentation requirement (Safi et al., 2021). Here we report a new instrumentation and speckle visibility model to obtain quantitative blood flow information overcoming the shot noise limit of the sensor at low laser power using an interferometric method, termed o heterodyne synthetic multi-exposure speckle imaging. Critically, our approach can be easily used as an ‘add-on’ to existing speckle imaging system instruments to increase the sensitivity of blood flow measurements.

4.2 Heterodyne Speckle Model

Heterodyne synthetic multi-exposure speckle imaging depends on the *heterodyne* interference between the light fields backscattered from the sample and light fields from a

reference arm. For this interferometric approach, the electric field can be expressed as,

$$E(t) = E_{\text{sample}}(t) + E_{\text{reference}}(t), \quad (\text{Eq. 4.1})$$

where, $E_{\text{sample}}(t)$ is the electric field backscattered from sample and $E_{\text{reference}}(t)$ electric field due to reference. The intensity recorded by the camera sensor is,

$$I(t) = |E(t)|^2, \quad (\text{Eq. 4.2})$$

$$I(t) = |E_{\text{sample}}(t) E_{\text{sample}}^*(t) + E_{\text{reference}}(t) E_{\text{reference}}^*(t) + 2\text{Re}\{E_{\text{sample}}(t) E_{\text{reference}}^*(t)\}|$$

Here, $E_{\text{reference}}(t)$ is similar to the static field amplitude in the multi-exposure speckle imaging model (Parthasarathy et. al., 2008). Following Siegert relation, (Bandyopadhyay et al., 2005) intensity autocorrelation function $g_2(\tau)$ can be written as-

$$g_2(\tau) = 1 + \beta \left[\frac{\langle I_s(t) \rangle^2}{(\langle I_s(t) \rangle + \langle I_r(t) \rangle)^2} |g_1(\tau)|^2 + \frac{2\langle I_s(t) \rangle \langle I_r(t) \rangle}{(\langle I_s(t) \rangle + \langle I_r(t) \rangle)^2} g_1(\tau) \right], \quad (\text{Eq. 4.3})$$

$$g_2(\tau) = 1 + \beta_1 |g_1(\tau)|^2 + \beta_2 g_1(\tau), \quad (\text{Eq. 4.4})$$

where,

$$\beta_1 = \beta \left(1 - \left(\frac{I_r(t)}{I_T(t)} \right)^2 \right), \beta_2 = 2\beta \frac{I_r(t)}{I_T(t)} \left(1 - \frac{I_r(t)}{I_T(t)} \right), \quad (\text{Eq. 4.5})$$

$$I_T = I_s + I_r, \quad (\text{Eq. 4.6})$$

Following (Bandyopadhyay et al., 2005) , we can express heterodyne speckle visibility as,

$$V_2(t) = \beta_1 \int_0^T 2 \left(1 - \frac{t}{T} \right) |g_1(t)|^2 \frac{dt}{T} + \beta_2 \int_0^T 2 \left(1 - \frac{t}{T} \right) |g_1(t)| \frac{dt}{T}, \quad (\text{Eq. 4.7})$$

Assuming Lorentzian distribution, $g_1(t) = e^{-t/\tau_c}$, we can write heterodyne speckle contrast as,

$$K = \left[\beta_1 \frac{e^{-2x} - 1 + 2x}{2x^2} + 2\beta_2 \frac{e^{-x} - 1 + x}{x^2} \right]^{1/2}, \quad (\text{Eq. 4.8})$$

Eq 4.10, is the new speckle visibility model for speckle imaging in heterodyne mode.

4.3 Instrumentation

A schematic of the optical system shown in Figure 4.1 is based on a free space Mach-Zehnder interferometry configuration. Light from a linearly polarized CW single mode laser diode ($\lambda=638$ nm, 150 mW, Thorlabs) is collimated using an aspheric lens (Thorlabs C171TMD-B - $f = 6.20$ mm, NA = 0.30). The collimated beam is split by a 90:10 non-polarizing beam splitter (Thorlabs BS076), 10 % beam is coupled to a step-Index multimode fiber optic patch cable (Thorlabs M124L01 - $\text{Ø}400$ μm , 0.50 NA), 90% light uniformly illuminates the sample at an angle 30-45 degree to vertical axis. 10% light from multimode fiber is collimated by a fiber collimator (Thorlabs F230FC-780 - 780 nm, $f = 4.51$ mm, NA = 0.55). Backscattered light from the sample was collected by an objective lens (4X, NA 0.10, Olympus). Backscattered beam and reference beam are then combined with a 50/50 beam splitter (Thorlabs CCM1-BS013) and imaged on a CMOS camera (Basler acA2000-165umNIR). Heterodyne speckle images were continuously recorded at a 100 Hz frame rate and 100 μs exposure time. Microfluidic flow phantoms were fabricated using methods described elsewhere (Parthasarathy et al., 2008, see also section 3.2.3). Images were collected while 20% intralipid was pumped through a $200 \mu\text{m} \times 150 \mu\text{m}$ flow channel, at flow rates 1 to 7 mm/s. Data processing of raw speckle images into *synthetic* multi-exposure images are as described earlier (section 3.2.1). Finally, synthetic heterodyne speckle contrast fit to Eq. 4.10 to estimate quantitative flow ($1/\tau_c$).

4.4 Results

4.4.1 Boosting Weak Dynamic Signal

Figure 4.2 shows intensity distribution (histogram) of the raw speckle images for both homodyne and heterodyne conditions, and representative raw speckle images from a microfluidic channel. For homodyne condition (blue, obtained by physically blocking the reference beam)

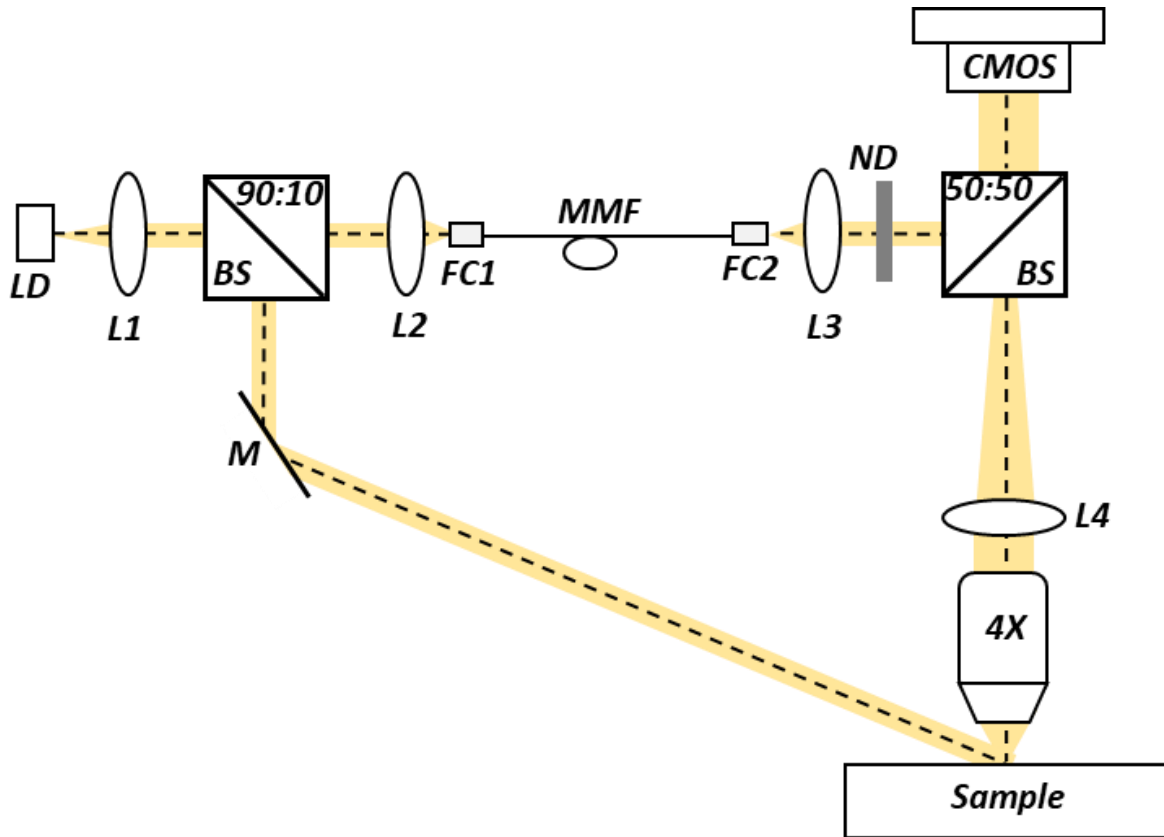


Figure 4.1 Schematic for heterodyne multi-exposure speckle imaging. LD-single mode laser diode, L-lens, BS- beam splitter, M-mirror, FC-fiber coupler, ND-neural density filter.

average intensity on camera is 33.75 (a.u.), which 4 times lower than lower than the intensity required to fill the dynamic range of the 8-bit camera sensor. Also, due to the low photon counts, imaged speckle is underdeveloped. Next, we introduced the reference arm with an average intensity (brown) 78.36 (a.u.). As we have used multimode fiber in the reference arm, we can control the intensity of the reference arm so that resulting heterodyne speckle pattern does not saturate the camera sensor. Finally, with heterodyne interference (yellow), overall average intensity increases to 113.73 (a.u.). From the inset we can clearly see dynamic speckle from the flow region boosted by the reference arm due to the heterodyne scheme compared to homodyne scheme. It is to be noted, as we are using multimode fiber in reference arm this is susceptible to

noise. Use of multimode fiber approached has been reported in the interferometric diffusive wave spectroscopy (Zhou et al., 2018).

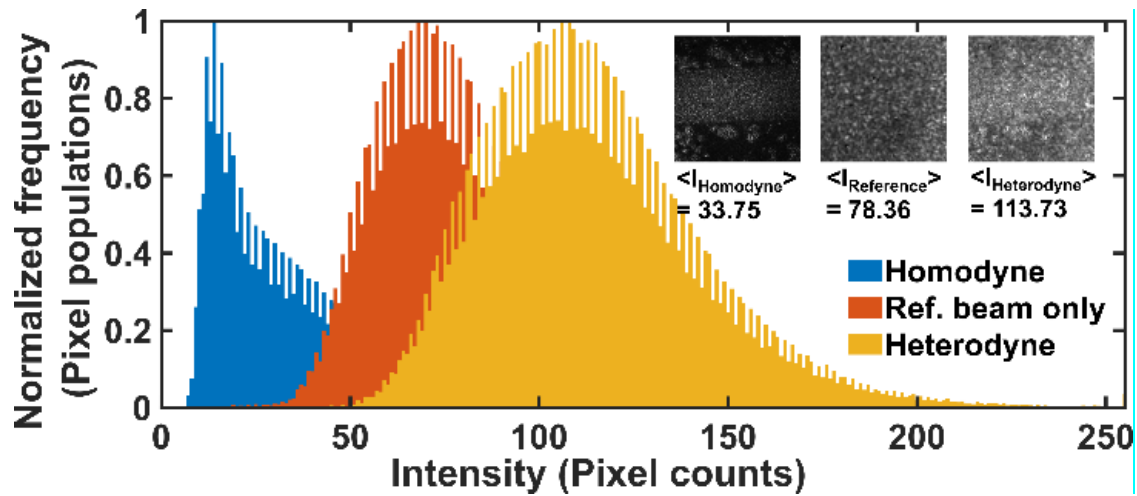


Figure 4.2 Characterization of heterodyne synthetic multi-exposure speckle imaging. Histogram of pixel intensities for homodyne and heterodyne method, with intensity map of the raw speckle images shown in the insets.

4.4.2 Quantitative Imaging of Flow in Presence of Photon Shot Noise

Figure 4.3 demonstrate the reconstruction of quantitative speckle contrast images with the heterodyne scheme. In traditional homodyne speckle imaging (with low photon counts typical of short exposure time $<1\text{ms}$) average intensity detected by the camera was low and the image was dominated by shot noise. Application of homodyne MESI/ syMESI data processing may yield artificially high speckle contrast values. The resultant blood flow image has poor sensitivity to the flow channel in the middle, with the entire image resembling that of a static speckle pattern. The heterodyne approach overcomes this issue by boosting the low mean intensity of from sample via the reference arm and can accurately evaluate speckle contrast image at short exposure time. As from Figure 4.3. It is evident that for homodyne approach at exposure time $100\ \mu\text{s}$, speckle contrast was high, whereas for the same exposure time by introducing reference arm we can accurately measure the speckle contrast image overcoming the shot noise.

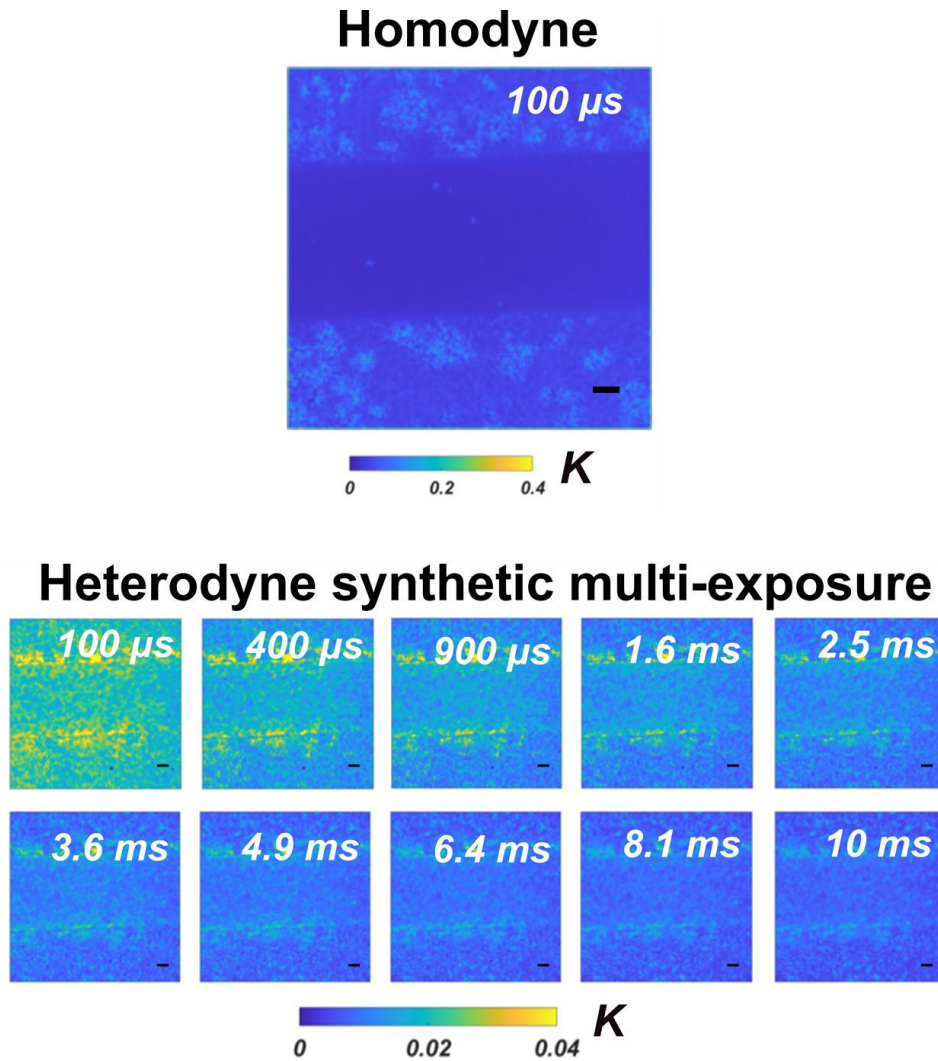


Figure 4.3 Comparison between homodyne speckle imaging and heterodyne synthetic MESI speckle contrast map for flow rate 5mm/s

4.4.3 Linearity of Large Flow Changes in Presence of Photon Shot Noise

The experimental setup (Figure 4.1) was used in conjunction with the synthetic exposure technique to perform controlled experiments on the microfluidic samples. Intralipid 20% was pumped through the sample using the syringe pump at different speeds from 1 mm/sec to 7 mm/sec in 1 mm/sec increments. 100 raw heterodyne speckle images were captured for each flow rate at 100 μs exposure duration. Similarly, 100 raw homodyne speckle images were captured for each flow rate at 100 μs exposure duration. For each speed and for both homodyne and heterodyne

mode, (n=3 trials) were performed and data was taken at 5 min interval for each speed, this allows flowing intralipid to reach defined flow speed throughout the microfluidic channel. For homodyne case, speckle contrast was estimated by traditional LSCI method (Senarathna et al., 2013). For heterodyne, using synthetic multi-exposure algorithm average heterodyne speckle contrast, as a function of exposure time, were calculated for the flow region. The heterodyne synthetic multi-exposure speckle contrast data was then fit to Eq. 4.10, by holding β and $\frac{I_r(t)}{I_T(t)}$ constant. Figure 4.4a shows the speckle variance (filled circles), measured from a region of interest within the microfluidic channel, as a function of exposure time, for speeds 1-7 mm/s. Solid lines represent fits to the heterodyne speckle model. Figure 4.4a clearly shows that the model fits the experimental data very well. The correlation time (a quantitative metric of flow) was estimated by having τ_c as a fitting parameter.

Next, we experimented whether the τ_c estimates obtained using the heterodyne speckle imaging instrument were more accurate than traditional single exposure LSCI measures by comparing the respective estimates of the relative correlation time measures. Correlation time estimates from traditional single exposure measures was obtained using the procedure detailed in (David A. Boas & Dunn, 2010). Relative correlation time measures were defined as $\frac{\text{Baseline } \tau_c}{\tau_c}$. Correlation time estimates were obtained from the fits performed in Figure 4.4a. the τ_c estimates obtained with the heterodyne instrument were compared with traditional homodyne single exposure estimates of τ_c at 100 μs to evaluate the efficacy of predicting relative flows. Ideally, relative correlation measures would be linear with relative speed. Relative correlation times were obtained for a baseline flow of 1 mm/sec.

Figure 4.4b shows the results of the relative blood flow experiment on microfluidic phantoms. The relative flow measured with the heterodyne model is shown in green, while the

relative flow measured with the homodyne model is shown in blue. The dashed black line represents the 1:1 correspondence between measured relative flow and relative flow in the channel. Figure 4.4b, shows that the new speckle model in conjunction with new heterodyne instrument and synthetic multi-exposure speckle imaging scheme can achieve linearity of relative correlation measures over a large flow range (nearly 6-fold) overcoming the photon shot noise. Standard deviation for estimating relative flow shows ($\leq \pm 0.18$) for the linear range. Whereas traditional homodyne based single exposure scheme failed to provide any relative change of flow, since the signal is completely buried in the noise level. This is expected as to evaluate linearity of relative change of flow average detected intensity needed to be at least 127 (a.u) for 8-bit and 32768 (a.u) for 16-bit camera. This allows fully utilizing the dynamic range of the camera and fully developed speckle. Homodyne single exposure laser speckle system or traditional homodyne multi-exposure system at such short exposure time (< 1 ms) is unable to achieve this dynamic range unless high laser power and sensitive detector used.

4.5 Discussion

Here, we have introduced a new quantitative speckle imaging instrument and new speckle model based on the interferometric method. Our method, directly address one of the main disadvantages of traditional speckle imaging modalities and both hardware based MESI or synthetic MESI i.e., scarcity of photon at shot exposure time which in turn effects the quantitative estimation of flow. We experimentally demonstrated our heterodyne technique can overcome this issue and increase the dynamic range of low-cost CMOS sensor. We believe, our new method can be valuable asset to intraoperative setting, as it can provide a clear quantitative blood flow image without using any exogenous contrast agent, thereby can help surgeons for any critical decision making. However, we note that, by introducing interferometric scheme we increase the sensitivity

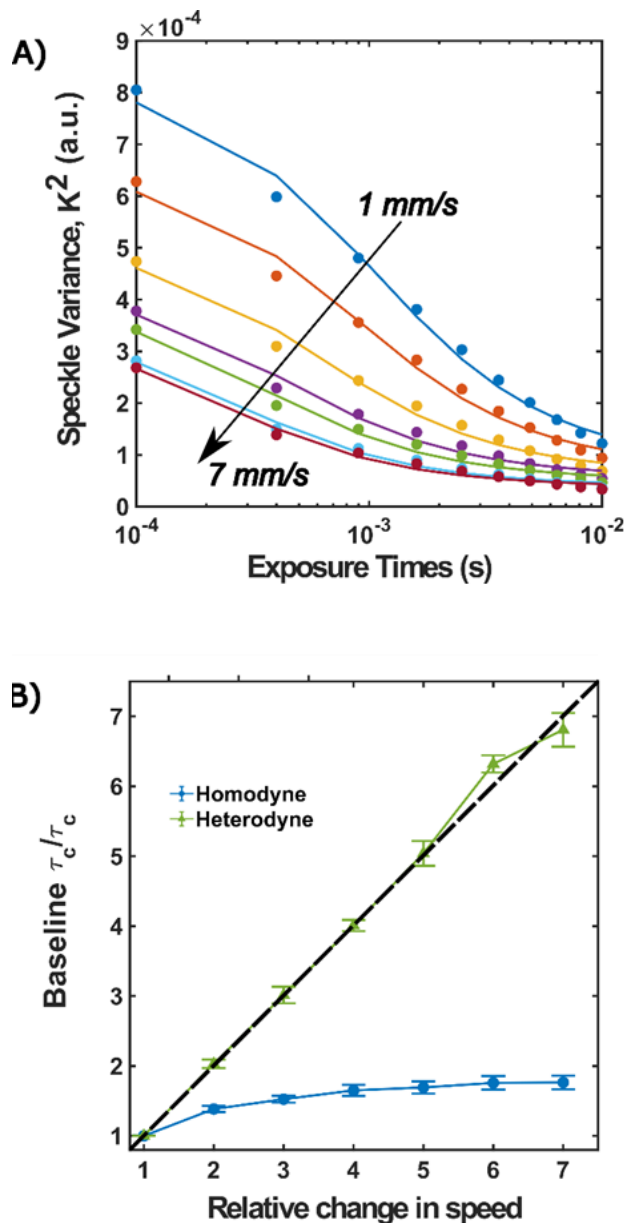


Figure 4.4 Heterodyne syMESI on microfluidic phantom study. A) Heterodyne synthetic speckle variance data fit to new speckle model. Speckle variance as a function of synthetic exposure duration for different speeds. Measurements were made on samples with no static scattering layer. B) Performance of homodyne model and heterodyne model to relative flow. Baseline speed: 1 mm/sec. Plot of relative τ_c to relative speed. Plot should ideally be a straight line (dashed line). Estimation using heterodyne synthetic multi-exposure extend linear range of relative τ_c estimates.

of the instrument. Unlike, traditional speckle imaging technique, where diode laser may not need to be temperature controlled, in our setup, temperature controller must be used in order to maintain the stability of the interference. Also, care should be taken in for shaping the laser beam in the

reference arm. Typical diode laser beam is elliptical in shape, here by introducing multimode fiber and with collimating lens we transformed the beam into uniform circular shape.

Our proposed heterodyne synthetic speckle imaging adapted from the concept of interferometric diffuse correlation spectroscopy (Robinson et al., 2020). To be noted, mathematical model for interferometric diffuse correlation spectroscopy has been developed for extracting blood flow index for diffusion regime using the correlation diffusion equation and this technique is for single speckle detection scheme hence for point detection only. To main goal, for the interferometric diffuse correlation spectroscopy to increase the strength of the signal coming from the long source-distance (SD) separation, typically >2.5 cm. Similarly, utilizing interferometer scheme and camera to capture multispeckle pattern, (Xu et al., 2020; Zhou et al., 2021), demonstrates boosting the weak signal coming from large SD separation. Whereas, our proposed heterodyne technique, model is for single scattering or ballistic regime. This allows imaging utilizing camera and a free space optical setup to capture speckle in a spatio-temporal manner and subsequently to reconstruct speckle contrast image to visualize the flow. The main goal of our proposed method is to increase the strength of the weak signal at short exposure time which is in generally buried in the photon shot noise in the camera. Hence, allowing quantitative speckle contrast imaging.

Chapter 5: Continuous Wave Pathlength Resolved Diffuse Correlation Spectroscopy³

5.1 Introduction

Diffuse Correlation Spectroscopy (DCS) is a robust noninvasive optical technique that has been widely used to directly measure microvascular flow in tissues (Boas & Yodh, 1997; Boas et al., 1995). DCS measures blood flow by analyzing temporal fluctuations in diffusely scattered light intensity brought about by the coherent addition of light fields traveling multiple path lengths in tissue. Formally, the temporal electric field autocorrelation is estimated from the intensity fluctuations and the Siegert relation (Bandyopadhyay et al., 2005; Lemieux & Durian, 1999), which is then fit to a solution to the Correlation Diffusion Equation to estimate blood flow in diffusion units (cm²/s), using either measured or assumed tissue optical properties (Boas & Yodh, 1997; Boas et al., 1995; Durduran et al., 2010). This unit of flow is absolute flow validated against MRI techniques (Carp et al., 2010; Jain et al., 2014; Yu et al., 2007). Figure 5.1. demonstrates a typical DCS working principle. Unlike ultrasound-based Doppler method, DCS is sensitive to small vessels and capillaries flow (Mesquita et al., 2011; Parthasarathy et al., 2018; Wang et al., 2016) making it an ideal tool for measuring tissue perfusion. In DCS, solution for CDE in case of homogenous semi-infinite tissue geometry can be expressed as-

$$g_1(\tau) = \frac{r_b \exp(-K_D(\tau)r_1) - r_1 \exp(-K_D(\tau)r_b)}{r_b \exp(-K_D(0)r_1) - r_1 \exp(-K_D(0)r_b)}, \quad (\text{Eq. 5.1})$$

³ Part of this chapter published in Safi, A. M., Moka, S., Harrah, M., Cini, S., & Parthasarathy, A. B. (2021, April). *Quantitative Measurement of Static and Dynamic Tissue Optical Properties with Continuous Wave Pathlength Resolved Diffuse Correlation Spectroscopy*. In *Optics and the Brain* (pp. BTh1B-6). Optical Society of America. Optical Society of America. Submitted for provisional patent: US Provisional patent application # 63/198,181 (Ashwin B Parthasarathy, Abdul Mohaimen Safi, Sadhu Moka)

where, τ , is correlation delay times, $K_D(\tau)^2 = (\mu_a + 6\mu'_s k_0^2 F)v/D$, F is the blood flow index, μ_a and μ'_s , the tissue absorption and reduced scattering coefficients respectively, k_0 , wave vector for tissue, $r_1^2 = (l_{tr}^2 + \rho^2)$ and $r_b^2 = ((2z_b + l_{tr})^2 + \rho^2)$ are constants which include transport mean-free path, $l_{tr} = 1/(\mu_a + \mu'_s)$, source detector separation, ρ , and $z_b = (2l_{tr}(1 + R_{eff}))/3(1 - R_{eff})$, R_{eff} effective reflection coefficient which accounts for refractive index mismatch between tissue (n_{tissue}) and surrounding medium (n_{medium}).

Electric field autocorrelation function $g_1(\tau)$, expressed in terms of intensity autocorrelation function $g_2(\tau)$, using Siegert relation (Bandyopadhyay et al., 2005; Lemieux & Durian, 1999) as-

$$g_2(\tau) = 1 + \beta |g_1(\tau)|^2, \quad (\text{Eq. 5.2})$$

where β accounts for coherence of the source, averaging of speckle and polarization. Typically, β assumed to be 0.5.

As detector only can measure intensity, hence intensity autocorrelation function which describes the intensity fluctuation in temporal domain, usually measured and converted to $g_1(\tau)$ using Eq. 5.2. and temporal intensity autocorrelation can be expressed as-

$$g_2(\tau) = \frac{\langle I(t)I(t+\tau) \rangle}{\langle I(t) \rangle^2}, \quad (\text{Eq. 5.3})$$

However, quantification of blood flow, especially, cerebral blood flow (CBF) using DCS is limited by the sensitivity issues due to the effect of scalp and skull thickness. Usually to measure CBF, DCS probe is placed on the scalp hence, measured CBF is a weighted sum of flow in cerebral tissues and flow in extra-cerebral tissues (scalp and skull) (Baker et al., 2014, 2015). The flow in extra-cerebral tissues is probe can be affected by systemic blood flow changes (e.g., due to blood pressure changes) or due to application of pressure on probe (Mesquita et al., 2011). Potential

solutions to this problem is algorithmic approach. (Baker et al., 2015). Furthermore, quantitative estimation of CBF relies on both tissue absorption and scattering coefficient, μ_a and μ'_s , respectively, since these are required to fit the measured autocorrelation function to the correlation diffusion model. Uncertainties in μ'_s estimation proportionally propagates into errors in estimation of CBF. For example, a 20% error in measuring μ'_s will lead to 20% error in estimation of CBF (Irwin et al., 2011). This variation effects the reliable clinical application of DCS. To solve this issue, often DCS is combined with frequency domain or time domain NIRS to determine absolute μ_a and μ'_s (Carp et al., 2017; He et al., 2018).

Traditionally, DCS instruments have used continuous wave (CW) laser sources, with coherence lengths ($>1\text{m}$) typically longer than the difference between the shortest and longest paths inside the tissue; therefore the measured autocorrelation function at the detector is from an ensemble average of all photon path lengths which can be written as (D. A. Boas & Yodh, 1997; Sutin et al., 2016).

$$g_1(\tau) = \int ds P(s) g_{1,s}(\tau, s) , \quad (\text{Eq. 5.4})$$

This equation denotes the dependence of field correlation to the pathlength, s . For traditional DCS, this equation is similar to the solution of CDE expressed in Eq. 5.1. Where, $P(s)$ is photon distribution probability inside sample for pathlength s . This averaging of pathlength results in loss of photon distribution of time-of-flight (DTOF) inside the medium. Since traditional DCS is unable to provide DTOF, as results optical properties is assumed from literature, experimentally measured by combining DCS with NIRS (Carp et al., 2017; He et al., 2018) or using multi-distance approach (Farzam & Durduran, 2015). These approaches make the DCS instrumentation bulky and limited to preclinical applications only. Furthermore, since shorter pathlengths (*i.e.*, from shallower tissue) are more probable than long pathlengths, the measured DCS autocorrelation functions are more

sensitive to extra-cerebral tissues rather than deep cerebral vasculatures. Therefore, a method to discriminate the DCS autocorrelation functions by pathlength will help address several of its critical limitations.

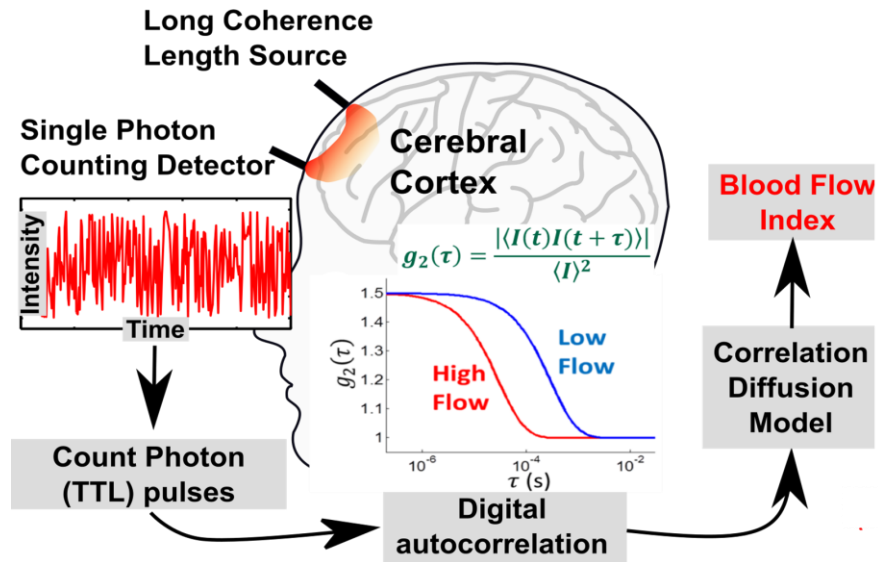


Figure 5.1 Schematic of noninvasive, fast measurement of CBF waveforms with diffuse correlation spectroscopy (DCS)

Yodh et al., 1990 first demonstrated path length resolved DCS, using an interferometry approach and a pulsed laser source. However, this method relies on the use of nonlinear optical elements and requires large amounts of optical power; hence it was unsuitable for *in vivo* experiments. Recently, (Sutin et al., 2016) and (M Pagliuzzi et al., 2017) demonstrated path resolved DCS measurements with Time Domain Diffuse Correlation Spectroscopy (TD-DCS). This approach uses a pulsed high coherence laser source to synchronize detection and time-tag photon arrival times. Thus, they can measure photon distribution of-flight (DTOF) information as well as separate flow shallow and deep layers in the tissue. Another recent instrument by (Borycki et al., 2016, 2017; Kholiqov et al., 2020) reported an interferometric approach based on swept source optical coherence tomography (OCT) to obtain optical properties and blood flow with a single SD separation. Unlike typical OCT, they used an intensity modulated light source with

instantaneous linewidth and narrow tuning range, which allows measurement of photon DTOF and longer photon path lengths. In both these approaches, measurement of photon time of flight information permitted estimation of tissue optical properties, which were then used to improve the fidelity of blood flow measured with DCS. However, both these approaches required the development of specialized pulsed/modulated laser sources with high temporal coherence and/or speed improvements to traditional DCS detectors.

Here, we report a simpler alternative to derive similar information from tissue (photon time of flight distribution and path length resolved electric field autocorrelation functions) using a new coherence gated DCS approach based on the principles of time domain OCT. Critically, our approach realizes these measurements with readily available CW multimode laser diodes with low temporal coherence length in the order of millimeter, and conventional DCS detection systems. Thus, our system can be used as an ‘add-on’ to existing DCS instruments to add path length sensitivity to blood flow measurements.

5.2 Theory

For pathlength resolved DCS, detectors measure the coherent addition of electric fields from the sample ($E_S(t)$) and reference ($E_R(t)$) arms, *i.e.*

$$I(t) = |E_S(t) + E_R(t)|^2, \quad (\text{Eq. 5.5})$$

where $E_S(t)$ is the superposition of light fields that have traveled multiple pathlengths through the tissue. Coherent interference of the sample and reference fields will occur only between fields that have traveled the same pathlength – thus, pathlength specific detection is achieved by simply varying the length (s) of the reference arm. The detected intensity can, therefore, be written as

$$I(s, t) = I_0 + I_{dcs}(s, t), \quad (\text{Eq. 5.6})$$

where I_0 is the incoherent addition of light fields from both the sample and reference arms that are

not pathlength matched.

$$I_0 = |E_s|^2 + |E_R|^2, \quad (\text{Eq. 5.7})$$

I_0 is a constant (approximately) that can be directly measured as the sum of the average intensities with the sample and reference arms sequentially blocked. $I_{dcs}(s, t)$ is the (heterodyne) pathlength matched interference term with temporal intensity fluctuations brought about by moving particles in the sample, around/about the selected pathlength and within the coherence length of the laser. Autocorrelation of $I(t)$ yields the pathlength resolved intensity autocorrelation function

$$g_2(\tau, s) = 1 + \beta(s)|g_1(\tau, s)|^2, \quad (\text{Eq. 5.8})$$

where $\beta(s)$ is the pathlength dependent instrumentation/speckle averaging factor, τ is the correlation delay time, s is the light pathlength, and $g_1(\tau, s)$ is the pathlength resolved electric field autocorrelation function. Flow (F) is computed by fitting $g_1(\tau, s)$ to a negative exponential model,

$$g_1(\tau, s) = \exp(-2\mu'_s F k_0^2 s \tau), \quad (\text{Eq. 5.9})$$

where μ'_s is the tissue reduced scattering coefficient and k_0 is the wave vector. Note that $g_1(\tau, s)$ is dependent only on F and μ'_s , and is independent of tissue absorption coefficient (μ_a). Since μ'_s is typically constant in tissue, pathlength resolved measurements of relative blood flow changes are less sensitive to tissue optical properties. Furthermore, the average of the measured intensity $I_{dcs}(s) = \langle I_{dcs}(s, t) \rangle$ can be converted to a time-resolved diffuse reflectance data by recognizing that photon time-of-flight in tissue.

$$\delta t = s/v, \quad (\text{Eq. 5.10})$$

where, v is the speed of light in tissue. Thus, $I_{dcs}(s) \rightarrow I_{dcs}(\delta t)$, when appropriately normalized will yield diffusion time-of-flight curves that can be fit to a time-domain solution photon diffusion

equation to estimate tissue optical properties, μ_a (absorption coefficient) and μ'_s (reduced scattering coefficient). We can express time domain solution as (Patterson et al., 1989) -

$$\Phi_{TD}(\rho, \delta t) = \frac{S_0 v \exp(-\mu_a v t)}{(4 \pi D t)^{3/2}} \left[\frac{\exp(-r_1^2)}{4 D t} - \frac{\exp(-r_b^2)}{4 D t} \right] \Bigg|_{z=0}, \quad (\text{Eq. 5.11})$$

where, $r_1^2 = (l_{tr}^2 + \rho^2)$ and $r_b^2 = ((2z_b + l_{tr})^2 + \rho^2)$ are constants which include transport mean-free path, $l_{tr} = 1/(\mu_a + \mu'_s)$, source detector separation, ρ , and $z_b = (2l_{tr} (1 + R_{eff}))/3(1 - R_{eff})$, R_{eff} effective reflection coefficient which accounts for refractive index mismatch between tissue (n_{tissue}) and surrounding medium (n_{medium}).

5.3 Data Processing

Figure 5.2 presents a typical data processing protocol for *invivo* depth sensitive measurements of blood flow. First, we record the DCS intensity autocorrelation functions and average intensities for multiple pathlengths – for a source-detector separation of 2.5 cm, measurements will span pathlengths 5~30 cm; longer pathlengths (>20 cm) sample tissues as deep as 2-3 cm below the surface. Pathlength resolved average intensities will be fit to a time-domain photon diffusion solution to first estimate tissue optical properties (μ_a and μ'_s), while the pathlength resolved intensity autocorrelation functions will be used to estimate baseline flow as a function of pathlength/depth. Then, the reference arm will be parked at a desired pathlength (depending on depth of interest), to record high-speed (20~100 Hz) depth-sensitive changes in blood flow.

5.4 Instrumentation

A schematic of our optical system, shown in Figure 5.3, is based on a fiber-based Mach-Zehnder interferometer. Light from a CW multimode laser diode (Thorlabs L808P500MM) with center wavelength $\lambda_c = 808$ nm and coherence length 0.5 mm is collimated using an aspheric lens. The collimated beam is coupled to a 90/10 multimode fiber coupler (Thorlabs TM105R2F1A),

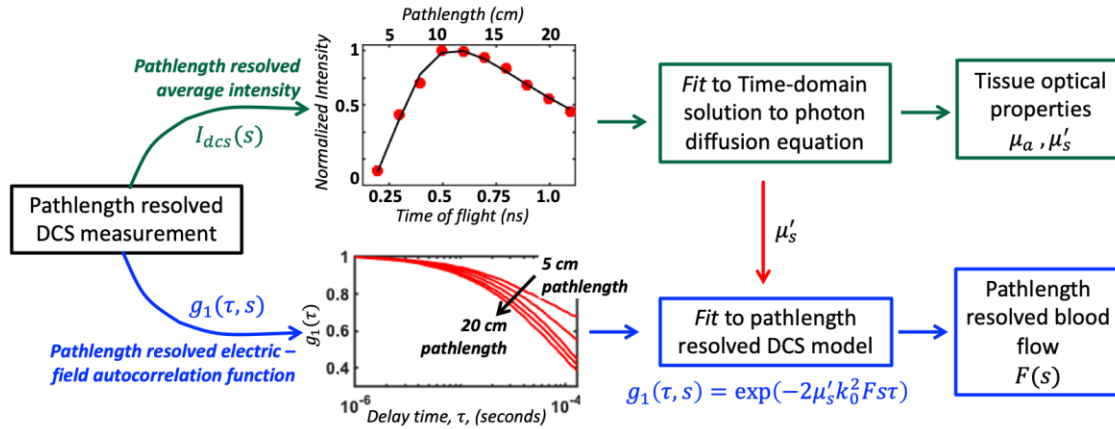


Figure 5.2 Data analysis scheme for pathlength resolved diffuse correlation spectroscopy (PR-DCS). A single measurement yields both pathlength resolved average intensities (top row – used to estimate optical properties) and electric field autocorrelation functions (bottom row – used to estimate blood flow). Once optical properties are computed, fast CBF measurements can be performed at a set/desired pathlength. Note that relative CBF measurements are independent of optical properties, since μ'_s is typically constant.

90% light is transmitted into the sample and 10% is transmitted to the reference arm. Two motorized translational stages (Thorlabs PT1Z8) with travel range each 50 mm total 100 mm have been added to the reference arm (delay line) to control pathlength sensitivity by coherence gating. Reflected light from the sample and retroreflector from the reference arm are combined with a 50/50 single mode fiber (Thorlabs TN808R5F1) and directed single photon counting avalanche photon diode modules (Excelitas SPCM 4AQC, Quebec, Canada). DCS photons are recorded at a 1 MHz sampling frequency and intensity autocorrelation functions can be recorded as 1-100 Hz using a custom software correlator (Wang et al., 2016). The DCS detectors measure the intensity autocorrelation of heterodyne mixing of light from the sample and reference arms. However, coherent interference of the two fields will occur only when the path lengths of the sample and reference arms are matched (i.e., by moving the delay line), within the coherence length of the laser. Then, moving particles in the sample – around/about the selected path lengths will impart temporal intensity fluctuations, which can be measured using traditional DCS systems.

intensity/field autocorrelation functions are obtained by scanning the delay line in the reference arm. Finally, the average intensity recorded as a function of path length can be readily converted to photon time-of-flight intensity distributions, to estimate tissue optical properties.

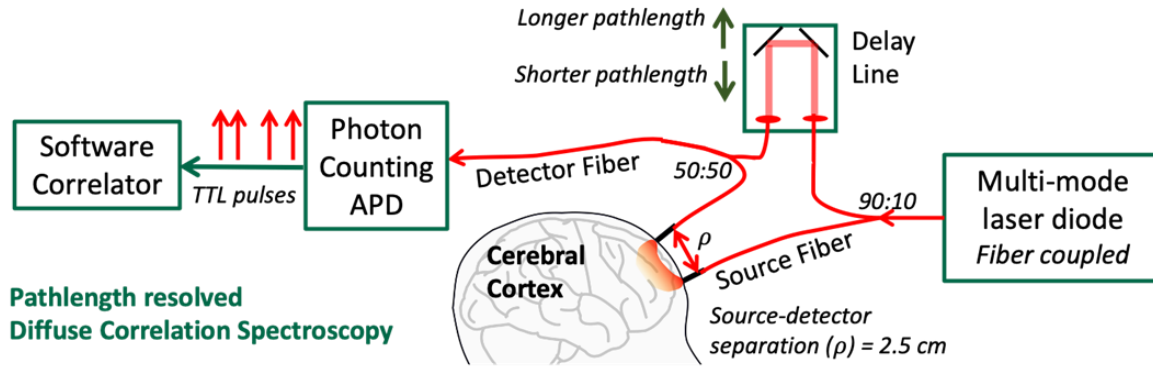


Figure 5.3 Schematic of proposed pathlength resolved diffuse correlation spectroscopy (PR-DCS) instrument. Light from a multi-mode laser diode is directed to a programmable delay line as well as the sample. A standard DCS detector arrangement is used to record the heterodyne interference between the sample and reference arms. Fibers of equal lengths will be used in the instrument.

5.5 Results

We demonstrate the feasibility of pathlength resolved blood flow measurements by estimating the static and dynamic (Figure 5.4B) optical properties of a semi-infinite tissue simulating phantom (intralipid + India ink, $\mu_a = 0.1 \text{ cm}^{-1}$, $\mu'_s = 8 \text{ cm}^{-1}$). PR-DCS measurements were performed with a source detector separation of 2.5 cm and integration time of 1 second. Figure 5.4A displays the diffusion time-of-flight (DTOF) curve obtained by analysis of pathlength resolved average intensities (red circles) fit to a time-domain solution to the diffusion equation (black line); optical properties ($\mu_a = 0.09 \text{ cm}^{-1}$, $\mu'_s = 7 \text{ cm}^{-1}$) were recovered to within 10% of their true value. Fig. 4B displays representative pathlength resolved electric field autocorrelation functions, fit to a negative exponential model; blood flow index, $\langle F \rangle = (3.4 \pm 0.1) \times 10^{-10} \text{ cm}^2/\text{s}$ (in diffusion units), was found to be constant (within 3%) across different pathlengths, as expected in this homogenous semi-infinite tissue phantom.

Next, we demonstrate the ability to measure depth sensitive blood flow with an in-vivo arm cuff ischemia experiment (schematic in Figure 5.5A). Briefly, PR-DCS measurements were performed on an arm of a healthy volunteer with a source-detector separation of 2.5 cm, and at light pathlengths of 5.4 cm (short) and 20.5 cm (long). Figure 5.5B displays representative fast (20 Hz) measurement of blood flow under baseline conditions at the 20.5 cm pathlength; blood flow pulsatility is clearly resolved demonstrating high signal-to-noise ratio of the approach. Figure 5.5C displays the hemodynamic response to arm cuff-ischemia measured at 1Hz with both long and short pathlengths; 1-minute baseline (blue region), ~2-minute occlusion (orange), 2-minute recovery (green). Hemodynamic response and reperfusion peak observed at the long pathlength (red curve) is typical of response from blood vessels in the muscle that lies deeper within the tissue. On the other hand, the corresponding response observed at the shorter pathlength is stunted indicating that the tissue sampled is primarily microvasculature in the skin. These experiments clearly demonstrate that the PR-DCS instrument is a robust instrument to measure static and dynamic tissue optical properties. In addition, the signal-to-noise ratio of the measurements is high enough to observe pulsatile blood flow changes even at longer pathlengths (low probability events), and the instrument can clearly discriminate between superficial and deep-tissue blood flow changes.

5.6 Discussion

In this work we have shown the feasibility of obtaining Brownian diffusion coefficients of scatterers in tissue mimicking phantom using off the shelf low coherence multimode laser diode only with a single source distance separation. By using the coherence gated approach, we have observed the typical decay of decorrelation time as we scan deeper into the tissue, which is similar to traditional TD-DCS approach.

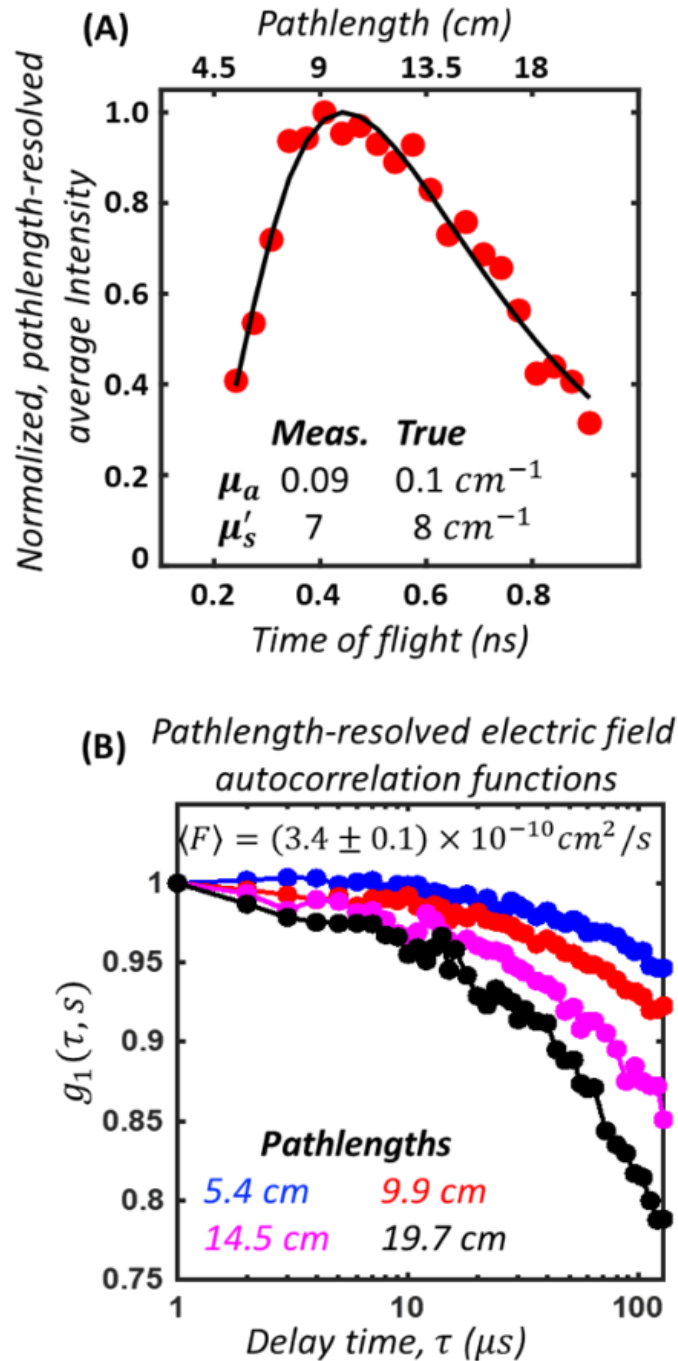


Figure 5.4 Experimental validation of pathlength resolved diffuse correlation spectroscopy (PR-DCS). (A) Pathlength resolved diffuse reflectance measurements (red circles) fit to a photon diffusion model to retrieve optical properties (<10% error) of homogeneous tissue simulating phantom with a source-detector separation of 2.5 cm. (B) Representative pathlength resolved electric field autocorrelation functions fit to DCS model to estimate blood flow (<3% variation in flow across pathlengths in homogeneous phantom).

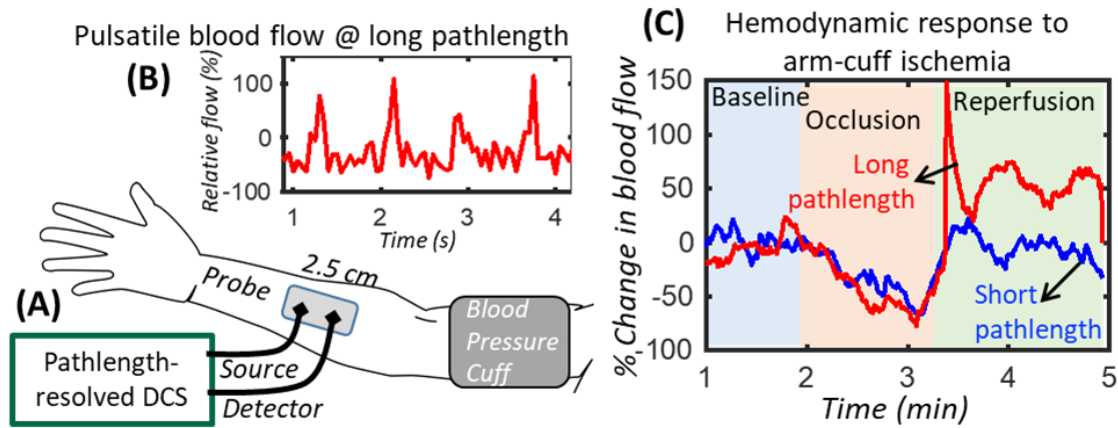


Figure 5.5 PR-DCS on *in vivo* experiment. (A) Schematic of in-vivo arm-cuff ischemia experiment. PR-DCS measurements were performed at 2.5 cm source-detector separation, at pathlengths of 5.4 and 20.5 cm (B) Representative time course of pulsatile blood flow measured from the arm of a volunteer with PR-DCS; 20 Hz measurement rate. (C) Relative changes in arm blood flow during arm-cuff ischemia measured at 1Hz. Red/blue curves indicate flow changes at 20.5/5.4 cm pathlengths respectively. Long pathlength response shows classic hyperemic reperfusion typically seen in deeper, larger blood vessels. Short pathlength response, from smaller, shallower blood vessels is stunted by comparison.

Here, we demonstrated for the first-time large source distance (SD) separation 2.5 cm using our pathlength DCS instrument. Existing pathlength DCS instrument either time domain based, or frequency domain based typically use SD separation 1cm or less to obtain path resolved information for deeper tissue. However, they cannot operate on higher SD separation as the detector need to be specialized for detecting photon. Since existing technique use specialized lasers so they lose SNR at large SD separation. Whereas due to the operation of multimode laser in CW mode we can increase signal to noise ratio at higher SD separation similar to traditional DCS system. Since our system operates at 2.5 cm SD separation, we can sample deeper tissues in the sample.

In terms of instrument, we have used a relatively low-cost multimode laser diode, while we retain the traditional DCS detector. Even though we used the same concept of Mach-Zehnder interferometer similar to existing path resolved DCS instruments, our source and detection system

are different. As existing system must use specialized source and detector which increases the system cost by employing low-cost multimode laser diode and traditional DCS detector we proposed a simple and alternative solution.

In the arm cuff experiment we showed that for the first higher a good signal-to-noise ratio at deeper path length even with 20Hz integration time, we can clearly see the pulsatility. and therefore, it is suitable to detect fast BFI. As expected, changes for shorter and longer path length. We can clearly observe the hyperemic peak for longer path length

Chapter 6: Conclusion and Future Work

My Ph.D. research work's focus was to develop new techniques for obtaining information mainly blood flow index, optical properties such as scattering coefficient, μ_s , and absorption coefficient, μ_a . I have developed and experimentally demonstrated a new speckle data processing algorithm termed as "Synthetic Multi-exposure Laser speckle Imaging", which reduces the instrument cost to 400-fold. Apart from the imaging field this algorithm can also be used in the diffuse speckle contrast analysis field. Photon shot noise is always a challenge in speckle imaging, affecting both single exposure laser speckle / multi-exposure laser speckle applications. I have developed a novel heterodyne speckle visibility theory and novel speckle imaging instrument. Combining with synthetic MESI algorithm this new heterodyne speckle imaging tool solves a decade-long problem. I hope this new imaging technique will provide fundamental information both in the preclinical and clinical realm.

Even though a significant portion of my research belongs to the macroscopic optical imaging field using utilizing spatial and temporal correlation of multi-speckle method, I have made a significant contribution in the diffuse correlation spectroscopy (DCS) field by introducing a technique by using a partially coherent continuous-wave laser source (in the order of few mm) in the Mach-Zehnder interferometer scheme. This allows for the first-time evaluation of optical properties and blood flow index at source-distance separation 2.5 cm. I believe all my developed techniques has opened up a new avenue of research in the dynamic light scattering field. In the future work section, I have included some applications/extensions of my developed techniques proposed in the thesis with I hope will helpful to the broader range of scientific community

working in the biomedical field.

6.1 Dual Wavelength Synthetic Multi-Exposure Imaging for Wound Care

As synthetic MESI allows the use of low-cost camera to obtain quantitative blood flow image. It will be interesting to use dual-wavelength approach to extract properties such as oxyhemoglobin (HbO), deoxyhemoglobin (Hb) and oxygen saturation (StO₂). Since synthetic MESI allows synchronous free camera with laser hence it facilitates to use RGB camera or even phone cameras. Both the cameras contain Bayer filter i.e., RGB (red-green-blue) channel. If we take the channel correspondent to laser wavelength for example if we shine laser of wavelength 633 nm which is more red shifted and of wavelength 532 nm simultaneously, red channel will provide scattering information due to the 633 nm wavelength and the green channel will provide scattering information related to 532 nm. So, using a color camera we can obtain scattering information of both lasers simultaneously. Then we can apply the synthetic MESI algorithm on the raw images of each channel raw image. This approach will make a portable quantitative imaging tool for monitoring HbO, Hb, StO₂ and blood flow simultaneously. Till now, in the clinic for wound care traditional single exposure speckle imaging system is used, which only allows qualitative blood flow index. Our dual wavelength syMESI approach can overcome this and will provide, other properties along with blood flow which can be a potential biomarker for wound healing and can aid physicians with the correct assessment.

6.2 Quantitative Assessment of Neurovascular Coupling

Cerebral blood flow (CBF) is closely linked to understanding neurovascular coupling (NVC) which gives indirect information of neuronal activity (Seker et al., 2021). Hence, measuring the relative change of CBF can help to get a clear idea of the cerebrovascular system under different stimulus conditions. Our developed heterodyne syMESI imaging system can be a proper

tool for detecting small change of CBF change due to stimulation as our interferometry technique increase the small signal which traditional imaging system cannot perform. Another advantage of our heterodyne system provides is high image acquisition speed and quantitative flow due to the use of syMESI algorithm. We believe using our approach for monitoring neurovascular coupling will play a critical role in Alzheimer's study (Bandyopadhyay, 2021; Tarantini et al., 2017). The biggest advantage is neuroscientists can get a quantitative response of neuronal activation for different animal models, breed and stimulation parameters, which can help to develop drug for increasing the response of neurons.

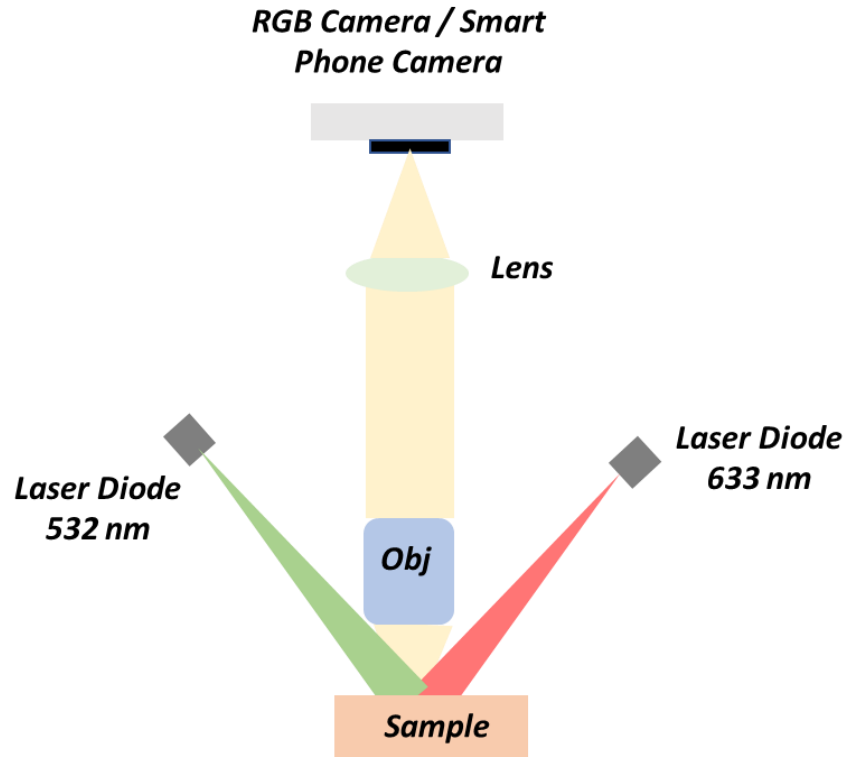


Figure 6.1 Dual wavelength synthetic multi-exposure imaging.

6.3 Blood Coagulation Measurement Using Synthetic Multi-Exposure Imaging

Traditional invitro blood coagulation studies use single exposure speckle contrast imaging approach to estimate the coagulation time. Few studies have shown the use of high-speed camera and performing intensity autocorrelation to extract the coagulation time (Jeon, Qureshi, Lee, &

Chung, 2019; Jeon, Qureshi, Lee, Badadhe, et al., 2019; Tripathi et al., 2014). Traditional hardware based MESI, due to its low temporal resolution is unable to perform blood coagulation study. However, since synthetic MESI is a single shot method, thereby it can capture images at a very high frame rate. This will allow quantitative blood coagulation time measurement even with a smartphone.

6.4 Wearable Deep Tissue Blood Flow Monitoring

As we demonstrated initial results syMESI algorithm in combination with diffusion theory can provide an alternative low-cost approach to deep tissue blood flow estimation. As our syMESI depends upon camera sensor pixels we can use bare CMOS/CCDD sensor chip (C. Huang et al., 2016) or miniaturized low noise CMOS camera (Xuhui Liu et al., 2021) to obtain quantitative deep tissue flow in wearable form factor. This could potentially be a useful tool for monitoring neonatal health.

6.5 Path-Length Resolved Measurement of Cerebral Autoregulation

An interesting application of path-length resolved diffuse correlation system will be to measure cerebral autoregulation. Till now, cerebral autoregulation measures with traditional CW DCS system. This allows measurement of cerebral autoregulation at a source distance separation up to 2.5 cm, which corresponds to depth inside the brain \sim 4cm. This scheme requires the utilization of a sophisticated algorithm and assumption of multilayer layer to remove the skull/scalp influence on the sensitive autoregulation signal (Baker et al., 2015). Path-length resolved measurement can mitigate this issue, as flow information is obtained only from the selected path length via interferometric method. This allows probing much deeper into the brain tissue without being affected by the skull/scalp. We believe this approach will eventually lead clinicians to a better understanding of the human brain working mechanism. Optical properties

and blood flow index obtained by the path-length resolved system may work as a biomarker and the index of cerebral autoregulation can help neurologists to come up with a treatment plan for diseases such as stroke, Parkinson, and Alzheimer's disease.

References

- Ayata, C., Dunn, A. K., Gursoy-Özdemir, Y., Huang, Z., Boas, D. A., & Moskowitz, M. A. (2004). Laser speckle flowmetry for the study of cerebrovascular physiology in normal and ischemic mouse cortex. *Journal of Cerebral Blood Flow and Metabolism*.
<https://doi.org/10.1097/01.WCB.0000122745.72175.D5>
- Baker, W. B., Parthasarathy, A. B., Busch, D. R., Mesquita, R. C., Greenberg, J. H., & Yodh, A. G. (2014). Modified Beer-Lambert law for blood flow. *Biomedical Optics Express*, 5(11), 4053–4075. <https://doi.org/10.1364/BOE.5.004053>
- Baker, W. B., Parthasarathy, A. B., Ko, T. S., Busch, D. R., Abramson, K., Tzeng, S.-Y., Mesquita, R. C., Durduran, T., Greenberg, J. H., Kung, D. K., & Yodh, A. G. (2015). Pressure modulation algorithm to separate cerebral hemodynamic signals from extracerebral artifacts. *Neurophotonics*, 2(3), 1–20. <https://doi.org/10.1117/1.NPh.2.3.035004>
- Bandyopadhyay, R., Gittings, A. S., Suh, S. S., Dixon, P. K., & Durian, D. J. (2005a). Speckle-visibility spectroscopy: A tool to study time-varying dynamics. *Review of Scientific Instruments*. <https://doi.org/10.1063/1.2037987>
- Bandyopadhyay, R., Gittings, A. S., Suh, S. S., Dixon, P. K., & Durian, D. J. (2005b). Speckle-visibility spectroscopy: A tool to study time-varying dynamics. *Review of Scientific Instruments*, 76(9), 1–11. <https://doi.org/10.1063/1.2037987>
- Bandyopadhyay, S. (2021). Role of Neuron and Glia in Alzheimer’s Disease and Associated Vascular Dysfunction. *Frontiers in Aging Neuroscience*, 13.
<https://doi.org/10.3389/fnagi.2021.653334>

- Berning, S., Willig, K. I., Steffens, H., Dibaj, P., & Hell, S. W. (2012). *Nanoscopy in a Living Mouse Brain*. 335(February). <https://doi.org/10.1126/science.1215369>
- Betzig, E., Patterson, G. H., Sougrat, R., Lindwasser, O. W., Olenych, S., Bonifacino, J. S., Davidson, M. W., Lippincott-Schwartz, J., & Hess, H. F. (2006). Imaging Intracellular Fluorescent Proteins at Nanometer Resolution. *Science*, 313(5793), 1642–1645. <https://doi.org/10.1126/science.1127344>
- Bi, R., Dong, J., & Lee, K. (2013). Deep tissue flowmetry based on diffuse speckle contrast analysis. *Optics Letters*, 38(9), 1401. <https://doi.org/10.1364/ol.38.001401>
- Bi, R., Du, Y., Singh, G., Ho, J.-H., Zhang, S., Ebrahim Attia, A. B., Li, X., & Olivo, M. C. (2020). Fast pulsatile blood flow measurement in deep tissue through a multimode detection fiber. *Journal of Biomedical Optics*. <https://doi.org/10.1117/1.jbo.25.5.055003>
- Boas, D. A., & Yodh, A. G. (1997). Spatially varying dynamical properties of turbid media probed with diffusing temporal light correlation. *Journal of the Optical Society of America A*. <https://doi.org/10.1364/josaa.14.000192>
- Boas, D A, Campbell, L. E., & Yodh, A. G. (1995). Scattering and Imaging with Diffusing Temporal Field Correlations. *Phys. Rev. Lett.*, 75(9), 1855–1858. <https://doi.org/10.1103/PhysRevLett.75.1855>
- Boas, David A., & Dunn, A. K. (2010). Laser speckle contrast imaging in biomedical optics. *Journal of Biomedical Optics*, 15(1), 011109. <https://doi.org/10.1117/1.3285504>
- Bonner, R., & Nossal, R. (1981). Model for laser Doppler measurements of blood flow in tissue. *Appl. Opt.*, 20(12), 2097–2107. <https://doi.org/10.1364/AO.20.002097>

- Borycki, D., Kholiqov, O., & Srinivasan, V. J. (2016). Interferometric near-infrared spectroscopy directly quantifies optical field dynamics in turbid media. *Optica*, 3(12), 1471.
<https://doi.org/10.1364/optica.3.001471>
- Borycki, D., Kholiqov, O., & Srinivasan, V. J. (2017). Reflectance-mode interferometric near-infrared spectroscopy quantifies brain absorption, scattering, and blood flow index in vivo. *Opt. Lett.*, 42(3), 591–594. <https://doi.org/10.1364/OL.42.000591>
- Bosworth, P., Masson, C. R., Melville, H. W., & Peaker, F. W. (1952). Determination of the molecular weights of fractionated polyvinyl acetates by a new type of light-scattering instrument. *Journal of Polymer Science*, 9(6), 565–574.
<https://doi.org/https://doi.org/10.1002/pol.1952.120090613>
- Briers, J. D., & Webster, S. (1996). Laser speckle contrast analysis (LASCA): a non-scanning, full-field technique for monitoring capillary blood flow. *Journal of Biomedical Optics*, 1(2), 174–179. <https://doi.org/10.1117/12.231359>
- Brunker, J., & Beard, P. (2016). Velocity measurements in whole blood using acoustic resolution photoacoustic Doppler. 7(7), 89–99. <https://doi.org/10.1364/BOE.7.002789>
- Calzetti, G., La Morgia, C., Cattaneo, M., Carta, A., Bosello, F., Amore, G., Carbonelli, M., Cascavilla, M. L., Gandolfi, S., Carelli, V., Schmetterer, L., Scholl, H. P. N., & Barboni, P. (2022). Longitudinal Study of Optic Disk Perfusion and Retinal Structure in Leber's Hereditary Optic Neuropathy. *Investigative Ophthalmology & Visual Science*, 63(1), 43.
<https://doi.org/10.1167/iovs.63.1.43>

- Calzetti, G., Mursch-Edlmayr, A. S., Bata, A. M., Ungaro, N., Mora, P., Chua, J., Schmidl, D., Bolz, M., Garhöfer, G., Gandolfi, S., Schmetterer, L., & Wong, D. (2022). Measuring optic nerve head perfusion to monitor glaucoma: a study on structure–function relationships using laser speckle flowgraphy. *Acta Ophthalmologica*, *100*(1), e181–e191.
<https://doi.org/https://doi.org/10.1111/aos.14862>
- Carp, S A, Dai, G. P., Boas, D. A., Franceschini, M. A., & Kim, Y. R. (2010). Validation of diffuse correlation spectroscopy measurements of rodent cerebral blood flow with simultaneous arterial spin labeling MRI; towards MRI-optical continuous cerebral metabolic monitoring. *Biomedical Optics Express*, *1*(2), 553–565.
<https://doi.org/10.1364/BOE.1.000553>
- Carp, Stefan A, Farzam, P., Redes, N., Hueber, D. M., & Franceschini, M. A. (2017). Combined multi-distance frequency domain and diffuse correlation spectroscopy system with simultaneous data acquisition and real-time analysis. *Biomedical Optics Express*, *8*(9), 3993–4006. <https://doi.org/10.1364/BOE.8.003993>
- Carvalho Brinca, A. M., de Castro Pinho, A., & Costa Vieira, R. J. D. (2021). Blood Perfusion of Random Skin Flaps in Humans—In Vivo Assessment by Laser Speckle Contrast Imaging. *Dermatologic Surgery*, *47*(11).
https://journals.lww.com/dermatologicsurgery/Fulltext/2021/11000/Blood_Perfusion_of_Random_Skin_Flaps_in_Humans_In.1.aspx
- Chammas, M., & Pain, F. (2022). Synthetic exposure with a CMOS camera for multiple exposure speckle imaging of blood flow. *Scientific Reports*, *12*(1), 4708.
<https://doi.org/10.1038/s41598-022-08647-6>

- Chen, C., Zhang, M., Yu, N., Zhang, W., Long, X., Wang, Y., & Wang, X. (2021). Heterogeneous Features of Keloids Assessed by Laser Speckle Contrast Imaging: A Cross-Sectional Study. *Lasers in Surgery and Medicine*, 53(6), 865–871. <https://doi.org/https://doi.org/10.1002/lsm.23331>
- Choi, W. J., Li, Y., Qin, W., & Wang, R. K. (2016). Cerebral capillary velocimetry based on temporal OCT speckle contrast. *Biomedical Optics Express*, 7(12), 4859. <https://doi.org/10.1364/BOE.7.004859>
- Chong, K., Ku, T., Choi, K., Choi, M., Yoon, J., & Choi, C. (2011). Current Optical Imaging Techniques for Brain Tumor Research: Application of in vivo Laser Scanning Microscopy Imaging with a Cranial Window System. In A. L. Abujamra (Ed.), *Diagnostic Techniques and Surgical Management of Brain Tumors*. IntechOpen. <https://doi.org/10.5772/22707>
- Cochran, J. M., Leproux, A., Busch, D. R., O’Sullivan, T. D., Yang, W., Mehta, R. S., Police, A. M., Tromberg, B. J., & Yodh, A. G. (2021). Breast cancer differential diagnosis using diffuse optical spectroscopic imaging and regression with z-score normalized data. *Journal of Biomedical Optics*, 26(2), 1–15. <https://doi.org/10.1117/1.JBO.26.2.026004>
- Colombo, L., Samaei, S., Lanka, P., Ancora, D., Pagliuzzi, M., Durduran, T., Sawosz, P., Liebert, A., & Pifferi, A. (2021). Speckle fluctuations in time-domain diffuse optics. In V. Tuchin, M. J. Leahy, & R. K. Wang (Eds.), *Dynamics and Fluctuations in Biomedical Photonics XVIII* (Vol. 11641, pp. 34–38). SPIE. <https://doi.org/10.1117/12.2577622>
- Conchello, J.-A., & Lichtman, J. W. (2005). Optical sectioning microscopy. *Nature Methods*, 2(12), 920–931. <https://doi.org/10.1038/nmeth815>

- Conkey, D. B., Caravaca-Aguirre, A. M., & Piestun, R. (2012). High-speed scattering medium characterization with application to focusing light through turbid media. *Opt. Express*, 20(2), 1733–1740. <https://doi.org/10.1364/OE.20.001733>
- Conroy, L., Dacosta, R. S., & Vitkin, I. A. (2012). *Quantifying tissue microvasculature with speckle variance optical coherence tomography*. 37(15), 3180–3182.
- Contag, C. H., & Bachmann, M. H. (2002). Advances in In Vivo Bioluminescence Imaging of Gene Expression. *Annual Review of Biomedical Engineering*, 4(1), 235–260. <https://doi.org/10.1146/annurev.bioeng.4.111901.093336>
- Dainty, J. C. (1972). Coherent Addition of a Uniform Beam to a Speckle Pattern. *J. Opt. Soc. Am.*, 62(4), 595–596. <https://doi.org/10.1364/JOSA.62.000595>
- Devor, A., Sakadžić, S., Srinivasan, V. J., Yaseen, M. a, Nizar, K., Saisan, P. a, Tian, P., Dale, A. M., Vinogradov, S. a, Franceschini, M. A., & Boas, D. a. (2012). Frontiers in optical imaging of cerebral blood flow and metabolism. *Journal of Cerebral Blood Flow & Metabolism*, 32(7), 1259–1276. <https://doi.org/10.1038/jcbfm.2011.195>
- Doty, P., & Steiner, R. F. (1950). Light Scattering and Spectrophotometry of Colloidal Solutions. *The Journal of Chemical Physics*, 18(9), 1211–1220. <https://doi.org/10.1063/1.1747913>
- Dragojević, T., Bronzi, D., Varma, H. M., Valdes, C. P., Castellvi, C., Villa, F., Tosi, A., Justicia, C., Zappa, F., & Durduran, T. (2015). High-speed multi-exposure laser speckle contrast imaging with a single-photon counting camera. *Biomedical Optics Express*, 6(8), 2865. <https://doi.org/10.1364/BOE.6.002865>

- Dragojević, T., Hollmann, J. L., Tamborini, D., Portaluppi, D., Buttafava, M., Culver, J. P., Villa, F., & Durduran, T. (2018). Compact, multi-exposure speckle contrast optical spectroscopy (SCOS) device for measuring deep tissue blood flow. *Biomedical Optics Express*. <https://doi.org/10.1364/boe.9.000322>
- Draijer, M., Hondebrink, E., van Leeuwen, T., & Steenbergen, W. (2008). Review of laser speckle contrast techniques for visualizing tissue perfusion. *Lasers in Medical Science*, 24(4), 639. <https://doi.org/10.1007/s10103-008-0626-3>
- Draijer, M., Hondebrink, E., Van Leeuwen, T., & Steenbergen, W. (2009). Review of laser speckle contrast techniques for visualizing tissue perfusion. *Lasers in Medical Science*, 24(4), 639–651. <https://doi.org/10.1007/s10103-008-0626-3>
- Dunn, A. K. (2012). Laser speckle contrast imaging of cerebral blood flow. *Annals of Biomedical Engineering*. <https://doi.org/10.1007/s10439-011-0469-0>
- Dunn, A. K., Bolay, H., Moskowitz, M. A., & Boas, D. A. (2001). Dynamic Imaging of Cerebral Blood Flow Using Laser Speckle. *Journal of Cerebral Blood Flow & Metabolism*, 21, 195–201. <https://doi.org/https://doi.org/10.1097/00004647-200103000-00002>
- Durduran, T., Burnett, M. G., Yu, G., Zhou, C., Furuya, D., Yodh, A. G., Detre, J. A., & Greenberg, J. H. (2004). Spatiotemporal Quantification of Cerebral Blood Flow during Functional Activation in Rat Somatosensory Cortex Using Laser-Speckle Flowmetry. *Journal of Cerebral Blood Flow and Metabolism*. <https://doi.org/10.1097/00004647-200405000-00005>

- Erdener, Ş. E., Tang, J., Sajjadi, A., Kılıç, K., Kura, S., Schaffer, C. B., & Boas, D. A. (2019). Spatio-temporal dynamics of cerebral capillary segments with stalling red blood cells. *Journal of Cerebral Blood Flow and Metabolism*.
<https://doi.org/10.1177/0271678X17743877>
- Farzam, P., & Durduran, T. (2015). Multidistance diffuse correlation spectroscopy for simultaneous estimation of blood flow index and optical properties. *Journal of Biomedical Optics*, 20(5), 1–10. <https://doi.org/10.1117/1.JBO.20.5.055001>
- Fercher, A. F., & Briers, J. D. (1981). Flow visualization by means of single-exposure speckle photography. *Optics Communications*, 37(5), 326–330. [https://doi.org/10.1016/0030-4018\(81\)90428-4](https://doi.org/10.1016/0030-4018(81)90428-4)
- Foord, R., Jakeman, E., Oliver, C. J., Pike, E. R., Blagrove, R. J., Wood, E., & Peacocke, A. R. (1970). Determination of diffusion coefficients of haemocyanin at low concentration by intensity fluctuation spectroscopy of scattered laser light. *Nature*, 227(5255), 242–245. <https://doi.org/10.1038/227242a0>
- Frijia, E. M., Billing, A., Lloyd-Fox, S., Vidal Rosas, E., Collins-Jones, L., Crespo-Llado, M. M., Amadó, M. P., Austin, T., Edwards, A., Dunne, L., Smith, G., Nixon-Hill, R., Powell, S., Everdell, N. L., & Cooper, R. J. (2021). Functional imaging of the developing brain with wearable high-density diffuse optical tomography: A new benchmark for infant neuroimaging outside the scanner environment. *NeuroImage*, 225, 117490. <https://doi.org/https://doi.org/10.1016/j.neuroimage.2020.117490>
- Fujii, H., & Asakura, T. (1974). Effect of surface roughness on the statistical distribution of image speckle intensity. *Optics Communications*, 11(1), 35–38. [https://doi.org/https://doi.org/10.1016/0030-4018\(74\)90327-7](https://doi.org/https://doi.org/10.1016/0030-4018(74)90327-7)

- Fujii, H., & Asakura, T. (1975). Statistical properties of image speckle patterns in partially coherent light. *Nouvelle Revue d'Optique*, 6(1), 5–14. <https://doi.org/10.1088/0335-7368/6/1/301>
- Gabriele, M. L., Wollstein, G., Ishikawa, H., Kagemann, L., Xu, J., Folio, L. S., & Schuman, J. S. (2011). Optical coherence tomography: history, current status, and laboratory work. *Investigative Ophthalmology & Visual Science*, 52(5), 2425–2436. <https://doi.org/10.1167/iovs.10-6312>
- Gibson, a P., Hebden, J. C., & Arridge, S. R. (2005). Recent advances in diffuse optical imaging. *Physics in Medicine and Biology*, 50(4), R1–R43. <https://doi.org/10.1088/0031-9155/50/4/R01>
- Goodman, J. W. (1975). Statistical Properties of Laser Speckle Patterns. In J. C. Dainty (Ed.), *Laser Speckle and Related Phenomena* (pp. 9–75). Springer Berlin Heidelberg. https://doi.org/10.1007/978-3-662-43205-1_2
- Gratton, E. (2011). Deeper Tissue Imaging with Total Detection. *Science*, 331(6020), 1016–1017. <https://doi.org/10.1126/science.1201542>
- Guilbert, J., & Desjardins, M. (2022). Movement correction method for laser speckle contrast imaging of cerebral blood flow in cranial windows in rodents. *Journal of Biophotonics*, 15(1), e202100218. <https://doi.org/https://doi.org/10.1002/jbio.202100218>
- Guzman-Sepulveda, J. R., & Dogariu, A. (2019). Probing complex dynamics with spatiotemporal coherence-gated DLS. *Appl. Opt.*, 58(13), D76--D90. <https://doi.org/10.1364/AO.58.000D76>

- Hashem, M., Shafqat, Q., Wu, Y., Rho, J. M., & Dunn, J. F. (2022). Abnormal oxidative metabolism in the cuprizone mouse model of demyelination: An in vivo NIRS-MRI study. *NeuroImage*, 250, 118935.
<https://doi.org/https://doi.org/10.1016/j.neuroimage.2022.118935>
- He, L., Baker, W. B., Milej, D., Kavuri, V. C., Mesquita, R. C., Busch, D. R., Abramson, K., Jiang, J. Y., Diop, M., Lawrence, K. St., Amendolia, O., Quattrone, F., Balu, R., Kofke, W. A., & Yodh, A. G. (2018). Noninvasive continuous optical monitoring of absolute cerebral blood flow in critically ill adults. *Neurophotonics*, 5(4), 1–15.
<https://doi.org/10.1117/1.NPh.5.4.045006>
- Hell, S. W., & Wichmann, J. (1994). Breaking the diffraction resolution limit by stimulated emission: stimulated-emission-depletion fluorescence microscopy. *Opt. Lett.*, 19(11), 780–782. <https://doi.org/10.1364/OL.19.000780>
- Helmchen, F., & Denk, W. (2005). Deep tissue two-photon microscopy. *Nature Methods*, 2(12), 932–940. <https://doi.org/10.1038/nmeth818>
- Hong, J., Zhu, X., Lu, J., & Li, P. (2021). Quantitative laser speckle auto-inverse covariance imaging for robust estimation of blood flow. *Optics Letters*.
<https://doi.org/10.1364/ol.422062>
- Huang, C., Seong, M., Morgan, J. P., Mazdeyasna, S., Kim, J. G., Hastings, J. T., & Yu, G. (2016). Low-cost compact diffuse speckle contrast flowmeter using small laser diode and bare charge-coupled-device. *Journal of Biomedical Optics*.
<https://doi.org/10.1117/1.jbo.21.8.080501>

- Huang, I.-T., Wu, K.-C., & Chen, J.-J. (2018). Development of Near-Infrared Diffuse Correlation Spectroscopy for Noninvasive Monitoring of Cerebral Blood Flow. In F. Ibrahim, J. Usman, M. Y. Ahmad, N. Hamzah, & S. J. Teh (Eds.), *2nd International Conference for Innovation in Biomedical Engineering and Life Sciences* (pp. 231–234). Springer Singapore.
- Hultman, M., Fredriksson, I., Larsson, M., Alvandpour, A., & Strömberg, T. (2018). A 15.6 frames per second 1-megapixel multiple exposure laser speckle contrast imaging setup. *Journal of Biophotonics*, *11*(2), e201700069.
<https://doi.org/https://doi.org/10.1002/jbio.201700069>
- Ikemura, T., Nakamura, N., & Hayashi, N. (2022). Impact of acute dynamic exercise on vascular stiffness in the retinal arteriole in healthy subjects. *Journal of Applied Physiology*, *132*(2), 459–468. <https://doi.org/10.1152/jappphysiol.00507.2021>
- Irwin, D., Dong, L., Shang, Y., Cheng, R., Kudrimoti, M., Stevens, S. D., & Yu, G. (2011). Influences of tissue absorption and scattering on diffuse correlation spectroscopy blood flow measurements. *Biomed. Opt. Express*, *2*(7), 1969–1985.
<https://doi.org/10.1364/BOE.2.001969>
- Ishikawa, M., Sekizuka, E., Shimizu, K., Yamaguchi, N., & Kawase, T. (1998). Measurement of RBC velocities in the rat pial arteries with an image-intensified high-speed video camera system. *Microvascular Research*. <https://doi.org/10.1006/mvre.1998.2100>
- Iyer, S. N., Behary, N., Nierstrasz, V., Guan, J., & Chen, G. (2019). Study of photoluminescence property on cellulosic fabric using multifunctional biomaterials riboflavin and its derivative Flavin mononucleotide. *Scientific Reports*, *9*(1), 8696. <https://doi.org/10.1038/s41598-019-45021-5>

- Jain, V., Buckley, E. M., Licht, D. J., Lynch, J. M., Schwab, P. J., Naim, M. Y., Lavin, N. A., Nicolson, S. C., Montenegro, L. M., Yodh, A. G., & Wehrli, F. W. (2014). Cerebral Oxygen Metabolism in Neonates with Congenital Heart Disease Quantified by MRI and Optics. *Journal of Cerebral Blood Flow & Metabolism*, *34*(3), 380–388. <https://doi.org/10.1038/jcbfm.2013.214>
- Jeon, H. J., Qureshi, M. M., Lee, S. Y., Badadhe, J. D., Cho, H., & Chung, E. (2019). Laser speckle decorrelation time-based platelet function testing in microfluidic system. *Scientific Reports*. <https://doi.org/10.1038/s41598-019-52953-5>
- Jeon, H. J., Qureshi, M. M., Lee, S. Y., & Chung, E. (2019). Optofluidic laser speckle image decorrelation analysis for the assessment of red blood cell storage. *PLoS ONE*, *14*(10), 1–14. <https://doi.org/10.1371/journal.pone.0224036>
- Judkewitz, B., Wang, Y. M., Horstmeyer, R., Mathy, A., & Yang, C. (2013). Speckle-scale focusing in the diffusive regime with time reversal of variance-encoded light (TROVE). *Nature Photonics*, *7*(4), 300–305. <https://doi.org/10.1038/nphoton.2013.31>
- Kase, S., Hasegawa, A., Hirooka, K., Endo, H., Noda, K., & Ishida, S. (2022). Laser speckle flowgraphy findings in a patient with radiation retinopathy. *International Journal of Ophthalmology*, *15*(1), 172–174. <https://doi.org/10.18240/ijo.2022.01.26>
- Kato, T. (2004). Principle and technique of NIRS-Imaging for human brain FORCE: fast-oxygen response in capillary event. *International Congress Series*, *1270*, 85–90. <https://doi.org/https://doi.org/10.1016/j.ics.2004.05.052>
- Kazmi, S M Shams, Balial, S., & Dunn, A. K. (2014). Optimization of camera exposure durations for multi-exposure speckle imaging of the microcirculation. *Biomed. Opt. Express*, *5*(7), 2157–2171. <https://doi.org/10.1364/BOE.5.002157>

- Kazmi, Syed Mohammad Shams, Parthasarthy, A. B., Song, N. E., Jones, T. a, & Dunn, A. K. (2013). Chronic imaging of cortical blood flow using Multi-Exposure Speckle Imaging. *Journal of Cerebral Blood Flow and Metabolism : Official Journal of the International Society of Cerebral Blood Flow and Metabolism*, 33(6), 798–808. <https://doi.org/10.1038/jcbfm.2013.57>
- Kholiqov, O., Zhou, W., Zhang, T., Du Le, V. N., & Srinivasan, V. J. (2020). Time-of-flight resolved light field fluctuations reveal deep human tissue physiology. *Nature Communications*, 11(1), 391. <https://doi.org/10.1038/s41467-019-14228-5>
- Kirkpatrick, N., Chung, E., Cook, D., Han, X., Gruionu, G., Liao, S., Munn, L., Padera, T., Fukumura, D., & Jain, R. K. (2012). Video-rate resonant scanning multiphoton microscopy: An emerging technique for intravital imaging of the tumor microenvironment. *IntraVital*, 1(1), 60–68. <https://doi.org/10.4161/intv.21557>
- Kisler, K., Nelson, A. R., Montagne, A., & Zlokovic, B. V. (2017). Cerebral blood flow regulation and neurovascular dysfunction in Alzheimer disease. In *Nature Reviews Neuroscience* (Vol. 18, Issue 7, pp. 419–434). <https://doi.org/10.1038/nrn.2017.48>
- Kono, T., & Yamada, J. (2019). In Vivo Measurement of Optical Properties of Human Skin for 450–800 nm and 950–1600 nm Wavelengths. *International Journal of Thermophysics*, 40(5), 51. <https://doi.org/10.1007/s10765-019-2515-3>
- Kratohvil, J. P., & Smart, C. (1965). Calibration of light-scattering instruments. III. Absolute angular intensity measurements on mie scatterers. *Journal of Colloid Science*, 20(8), 875–892. [https://doi.org/https://doi.org/10.1016/0095-8522\(65\)90060-7](https://doi.org/https://doi.org/10.1016/0095-8522(65)90060-7)

- Lam, J. H., Hill, B. Y., Quang, T., Amelard, R., Kim, S., Yazdi, H. S., Warren, R. V, Cutler, K. B., & Tromberg, B. J. (2021). Multi-modal diffuse optical spectroscopy for high-speed monitoring and wide-area mapping of tissue optical properties and hemodynamics. *Journal of Biomedical Optics*, 26(8), 1–15. <https://doi.org/10.1117/1.JBO.26.8.085002>
- Langmuir, R. V. (1963). SCATTERING OF LASER LIGHT. *Applied Physics Letters*, 2(2), 29–30. <https://doi.org/10.1063/1.1753756>
- Lazaridis, A., Triantafyllou, A., Dipla, K., Dolgyras, P., Koletsos, N., Anyfanti, P., Aslanidis, S., Douma, S., & Gkaliagkousi, E. (2022). Skin microvascular function, as assessed with laser speckle contrast imaging, is impaired in untreated essential and masked hypertension. *Hypertension Research*, 45(3), 445–454. <https://doi.org/10.1038/s41440-021-00816-w>
- Lemieux, P.-A., & Durian, D. J. (1999). Investigating non-Gaussian scattering processes by using nth-order intensity correlation functions. *J. Opt. Soc. Am. A*, 16(7), 1651–1664. <https://doi.org/10.1364/JOSAA.16.001651>
- Li, H., Liu, Q., Lu, H., Li, Y., Zhang, H. F., & Tong, S. (2014). Directly measuring absolute flow speed by frequency-domain laser speckle imaging. *Optics Express*, 22(17), 21079. <https://doi.org/10.1364/OE.22.021079>
- Liang, X., Zou, Q., He, Y., & Yang, Y. (2013). Coupling of functional connectivity and regional cerebral blood flow reveals a physiological basis for network hubs of the human brain. *Proceedings of the National Academy of Sciences of the United States of America*. <https://doi.org/10.1073/pnas.1214900110>
- Liu, J., Zhang, H., Lu, J., Ni, X., & Shen, Z. (2017). Simultaneously extracting multiple parameters via multi-distance and multi-exposure diffuse speckle contrast analysis. *Biomedical Optics Express*. <https://doi.org/10.1364/boe.8.004537>

- Liu, W., Qian, R., Xu, S., Chandra Konda, P., Jönsson, J., Harfouche, M., Borycki, D., Cooke, C., Berrocal, E., Dai, Q., Wang, H., & Horstmeyer, R. (2021). Fast and sensitive diffuse correlation spectroscopy with highly parallelized single photon detection. *APL Photonics*.
<https://doi.org/10.1063/5.0031225>
- Liu, Xuan, Zhang, K., Huang, Y., & Kang, J. U. (2011a). *Spectroscopic-speckle variance OCT for microvasculature detection and analysis*. 2(11), 545–547.
- Liu, Xuan, Zhang, K., Huang, Y., & Kang, J. U. (2011b). Spectroscopic-speckle variance OCT for microvasculature detection and analysis. *Biomed. Opt. Express*, 2(11), 2995–3009.
<https://doi.org/10.1364/BOE.2.002995>
- Liu, Xuhui, Gu, Y., Huang, C., Zhao, M., Cheng, Y., Jawdeh, E. G. A., Bada, H. S., Chen, L., & Yu, G. (2021). Simultaneous measurements of tissue blood flow and oxygenation using a wearable fiber-free optical sensor. *Journal of Biomedical Optics*, 26(1), 1–15.
<https://doi.org/10.1117/1.JBO.26.1.012705>
- Lockwood, D. J. (2016). Rayleigh and Mie Scattering. In M. R. Luo (Ed.), *Encyclopedia of Color Science and Technology* (pp. 1097–1107). Springer New York.
https://doi.org/10.1007/978-1-4419-8071-7_218
- Magnain, C., Castel, A., Boucneau, T., Simonutti, M., Ferezou, I., Rancillac, A., Vitalis, T., Sahel, J. A., Paques, M., & Atlan, M. (2014). Holographic laser Doppler imaging of microvascular blood flow. *Journal of the Optical Society of America A*, 31(12), 2723.
<https://doi.org/10.1364/JOSAA.31.002723>
- Maiman, T. H. (1960). Stimulated optical radiation in Ruby. *Nature*, 187(4736), 493–494.
<https://doi.org/10.1038/187493a0>

- Mangraviti, A., Volpin, F., Cha, J., Cunningham, S. I., Raje, K., Brooke, M. J., Brem, H., Olivi, A., Huang, J., Tyler, B. M., & Rege, A. (2020). Intraoperative Laser Speckle Contrast Imaging For Real-Time Visualization of Cerebral Blood Flow in Cerebrovascular Surgery: Results From Pre-Clinical Studies. *Scientific Reports*.
<https://doi.org/10.1038/s41598-020-64492-5>
- Mariampillai, A., Leung, M. K. K., Jarvi, M., Standish, B. A., Lee, K., Wilson, B. C., Vitkin, A., & Yang, V. X. D. (2010). *Optimized speckle variance OCT imaging of microvasculature*. *35*(8), 1257–1259.
- Masters, B. R. (2008). Handbook of Biological Confocal Microscopy, Third Edition. *Journal of Biomedical Optics*, *13*(2). <https://doi.org/10.1117/1.2911629>
- Mayerhöfer, T. G., Pahlow, S., & Popp, J. (2020). The Bouguer-Beer-Lambert Law: Shining Light on the Obscure. *ChemPhysChem*, *21*(18), 2029–2046.
<https://doi.org/https://doi.org/10.1002/cphc.202000464>
- Mazdeyasna, S., Huang, C., Zhao, M., Agochukwu, N. B., Bahrani, A. A., Wong, L., & Yu, G. (2018). Noncontact speckle contrast diffuse correlation tomography of blood flow distributions in tissues with arbitrary geometries. *Journal of Biomedical Optics*, *23*(9), 1–9.
<https://doi.org/10.1117/1.JBO.23.9.096005>
- Mesquita, R. C., Durduran, T., Yu, G., Buckley, E. M., Kim, M. N., Zhou, C., Choe, R., Sunar, U., & Yodh, A. G. (2011). Direct measurement of tissue blood flow and metabolism with diffuse optics. *Philosophical Transactions of the Royal Society A: Mathematical, Physical and Engineering Sciences*, *369*(1955), 4390–4406. <https://doi.org/10.1098/rsta.2011.0232>

- Miao, P., Lu, H., Liu, Q., Li, Y., & Tong, S. (2011). Laser speckle contrast imaging of cerebral blood flow in freely moving animals. *Journal of Biomedical Optics*, *16*(9), 090502. <https://doi.org/10.1117/1.3625231>
- Miller, D. R., Ashour, R., Sullender, C. T., & Dunn, A. K. (2022). Continuous blood flow visualization with laser speckle contrast imaging during neurovascular surgery. *Neurophotonics*, *9*(2), 1–12. <https://doi.org/10.1117/1.NPh.9.2.021908>
- Murali, K., Nandakumaran, A. K., & Varma, H. M. (2020). On the equivalence of speckle contrast-based and diffuse correlation spectroscopy methods in measuring in vivo blood flow. *Optics Letters*. <https://doi.org/10.1364/ol.397979>
- Murali, K., & Varma, H. M. (2020). Multi-speckle diffuse correlation spectroscopy to measure cerebral blood flow. *Biomedical Optics Express*. <https://doi.org/10.1364/boe.401702>
- Nadort, A., Kalkman, K., van Leeuwen, T. G., & Faber, D. J. (2016). Quantitative blood flow velocity imaging using laser speckle flowmetry. *Scientific Reports*, *6*(April), 25258. <https://doi.org/10.1038/srep25258>
- Nadort, A., Woolthuis, R. G., van Leeuwen, T. G., & Faber, D. J. (2013). Quantitative laser speckle flowmetry of the in vivo microcirculation using sidestream dark field microscopy. *Biomedical Optics Express*, *4*(11), 2347–2361. <https://doi.org/10.1364/BOE.4.002347>
- Ntziachristos, V. (2010). Going deeper than microscopy: the optical imaging frontier in biology. *Nature Methods*, *7*(8), 603–614. <https://doi.org/10.1038/nmeth.1483>
- Ntziachristos, V., & Razansky, D. (2010). Molecular Imaging by Means of Multispectral Optoacoustic Tomography (MSOT). *Chemical Reviews*, *110*(5), 2783–2794. <https://doi.org/10.1021/cr9002566>

- Outer, P., Carr, C. I., & Zimm, B. H. (1950). Light Scattering Investigation of the Structure of Polystyrene. *The Journal of Chemical Physics*, 18(6), 830–839.
<https://doi.org/10.1063/1.1747783>
- Pagliazzi, M., Sekar, S. K. V., Colombo, L., Martinenghi, E., Minnema, J., Erdmann, R., Contini, D., Mora, A. D., Torricelli, A., Pifferi, A., & Durduran, T. (2017). Time domain diffuse correlation spectroscopy with a high coherence pulsed source: in vivo and phantom results. *Biomed. Opt. Express*, 8(11), 5311–5325. <https://doi.org/10.1364/BOE.8.005311>
- Pagliazzi, Marco, Colombo, L., Vidal-Rosas, E. E., Dragojević, T., Parfentyeva, V., Culver, J. P., Sekar, S. K. V., Sieno, L. Di, Contini, D., Torricelli, A., Pifferi, A., Mora, A. D., & Durduran, T. (2021). Time resolved speckle contrast optical spectroscopy at quasi-null source-detector separation for non-invasive measurement of microvascular blood flow. *Biomed. Opt. Express*, 12(3), 1499–1511. <https://doi.org/10.1364/BOE.418882>
- Parry, G. (1975). Speckle Patterns in Partially Coherent Light. In J. C. Dainty (Ed.), *Laser Speckle and Related Phenomena* (pp. 77–121). Springer Berlin Heidelberg.
https://doi.org/10.1007/978-3-662-43205-1_3
- Parthasarathy, A. B., Gannon, K. P., Baker, W. B., Favilla, C. G., Balu, R., Kasner, S. E., Yodh, A. G., Detre, J. A., & Mullen, M. T. (2018). Dynamic autoregulation of cerebral blood flow measured non-invasively with fast diffuse correlation spectroscopy. *Journal of Cerebral Blood Flow and Metabolism*. <https://doi.org/10.1177/0271678X17747833>
- Parthasarathy, A. B., Kazmi, S. M. S., & Dunn, A. K. (2010). *Quantitative imaging of ischemic stroke through thinned skull in mice with Multi Exposure Speckle Imaging*. 1(1), 246–259.
<https://doi.org/10.1364/BOE.1.000246>

- Parthasarathy, A. B., Tom, W. J., Gopal, A., Zhang, X., & Dunn, A. K. (2008a). Robust flow measurement with multi-exposure speckle imaging. *Optics Express*, *16*(3), 1975. <https://doi.org/10.1364/oe.16.001975>
- Parthasarathy, A. B., Tom, W. J., Gopal, A., Zhang, X., & Dunn, A. K. (2008b). Robust flow measurement with multi-exposure speckle imaging. *Optics Express*, *16*(3), 1975–1989.
- Parthasarathy, A. B., Weber, E. L., Richards, L. M., Fox, D. J., & Dunn, A. K. (2010). Laser speckle contrast imaging of cerebral blood flow in humans during neurosurgery: a pilot clinical study. *Journal of Biomedical Optics*. <https://doi.org/10.1117/1.3526368>
- Patterson, M. S., Chance, B., & Wilson, B. C. (1989). Time resolved reflectance and transmittance for the noninvasive measurement of tissue optical properties. *Appl. Opt.*, *28*(12), 2331–2336. <https://doi.org/10.1364/AO.28.002331>
- Pedersen, H. M. (1974). The roughness dependence of partially developed, monochromatic speckle patterns. *Optics Communications*, *12*(2), 156–159. [https://doi.org/10.1016/0030-4018\(74\)90380-0](https://doi.org/10.1016/0030-4018(74)90380-0)
- Pellett, P. A., Sun, X., Gould, T. J., Rothman, J. E., Xu, M.-Q., Corrêa, I. R., & Bewersdorf, J. (2011). Two-color STED microscopy in living cells. *Biomed. Opt. Express*, *2*(8), 2364–2371. <https://doi.org/10.1364/BOE.2.002364>
- Pine, D. J., Weitz, D. A., Chaikin, P. M., & Herbolzheimer, E. (1988). Diffusing wave spectroscopy. *Physical Review Letters*, *60*(12), 1134.
- Qureshi, M. M., Liu, Y., Mac, K. D., Kim, M., Safi, A. M., & Chung, E. (2021). Quantitative blood flow estimation in vivo by optical speckle image velocimetry. *Optica*, *8*(8), 1092–1101. <https://doi.org/10.1364/OPTICA.422871>

- Raichle, M. E., Posner, J. B., & Plum, F. (1970). Cerebral blood flow during and after hyperventilation. *Archives of Neurology*.
- Ramirez-San-Juan, J. C., Regan, C., Coyotl-Ocelotl, B., & Choi, B. (2014). Spatial versus temporal laser speckle contrast analyses in the presence of static optical scatterers. *Journal of Biomedical Optics*, 19(10), 1–5. <https://doi.org/10.1117/1.JBO.19.10.106009>
- Razansky, D., Buehler, A., & Ntziachristos, V. (2011). Volumetric real-time multispectral optoacoustic tomography of biomarkers. *Nature Protocols*, 6(8), 1121–1129. <https://doi.org/10.1038/nprot.2011.351>
- Richards, L. M., Kazmi, S. M. S., Davis, J. L., Olin, K. E., & Dunn, A. K. (2013). Low-cost laser speckle contrast imaging of blood flow using a webcam. *Biomedical Optics Express*. <https://doi.org/10.1364/boe.4.002269>
- Richards, L. M., Kazmi, S. S., Olin, K. E., Waldron, J. S., Fox, D. J., & Dunn, A. K. (2017). Intraoperative multi-exposure speckle imaging of cerebral blood flow. *Journal of Cerebral Blood Flow & Metabolism*, 0271678X1668698. <https://doi.org/10.1177/0271678X16686987>
- Robinson, M. B., Boas, D. A., Sakadzic, S., Franceschini, M. A., & Carp, S. A. (2020). Interferometric diffuse correlation spectroscopy improves measurements at long source–detector separation and low photon count rate. *Journal of Biomedical Optics*. <https://doi.org/10.1117/1.jbo.25.9.097004>
- Roe, A. W. (2010). Imaging the brain with optical methods. In *Imaging the Brain with Optical Methods*. <https://doi.org/10.1007/978-1-4419-0452-2>

- Rust, M. J., Bates, M., & Zhuang, X. (2006). Sub-diffraction-limit imaging by stochastic optical reconstruction microscopy (STORM). *Nature Methods*, 3(10), 793–796.
<https://doi.org/10.1038/nmeth929>
- Safi, A., & Chung, E. (2015). Biomedical in vivo Optical Imaging for Disease Espying and Diagnosis. *Biomedical Engineering: Frontier Research and Converging Technologies*, 329–355.
- Safi, A. M., Qureshi, M. M., Liu, Y., & Chung, E. (2019). Optical Speckle Image Correlation Velocimetry (OSICV) - A New Quantitative Blood Flow Imaging Tool. *Biophotonics Congress: Optics in the Life Sciences Congress 2019 (BODA, BRAIN, NTM, OMA, OMP)*, DM3B.4. <https://doi.org/10.1364/BODA.2019.DM3B.4>
- Samaei, S., Sawosz, P., Kacprzak, M., Pastuszak, Ż., Borycki, D., & Liebert, A. (2021). Time-domain diffuse correlation spectroscopy (TD-DCS) for noninvasive, depth-dependent blood flow quantification in human tissue in vivo. *Scientific Reports*, 11(1), 1817.
<https://doi.org/10.1038/s41598-021-81448-5>
- Schawlow, A. L., & Townes, C. H. (1958). Infrared and Optical Masers. *Phys. Rev.*, 112(6), 1940–1949. <https://doi.org/10.1103/PhysRev.112.1940>
- Schneider, C. A., Rasband, W. S., & Eliceiri, K. W. (2012). NIH Image to ImageJ: 25 years of image analysis. *Nature Methods*, 9(7), 671–675. <https://doi.org/10.1038/nmeth.2089>
- Scholler, J. (2019). Motion artifact removal and signal enhancement to achieve in vivo dynamic full field OCT. *Opt. Express*, 27(14), 19562–19572. <https://doi.org/10.1364/OE.27.019562>

- Scholler, J., Mazlin, V., Thouvenin, O., Groux, K., Xiao, P., Sahel, J.-A., Fink, M., Boccara, C., & Grieve, K. (2019). Probing dynamic processes in the eye at multiple spatial and temporal scales with multimodal full field OCT. *Biomed. Opt. Express*, *10*(2), 731–746.
<https://doi.org/10.1364/BOE.10.000731>
- Seker, F. B., Fan, Z., Gesierich, B., Gaubert, M., Sienel, R. I., & Plesnila, N. (2021). Neurovascular Reactivity in the Aging Mouse Brain Assessed by Laser Speckle Contrast Imaging and 2-Photon Microscopy: Quantification by an Investigator-Independent Analysis Tool. *Frontiers in Neurology*, *12*. <https://doi.org/10.3389/fneur.2021.745770>
- Senarathna, J., Member, S., Rege, A., Li, N., & Thakor, N. V. (2013). *Laser Speckle Contrast Imaging : Theory , Instrumentation and Applications*. *6*, 99–110.
- Seylaz, J., Charbonné, R., Nanri, K., Von Euw, D., Borredon, J., Kacem, K., Méric, P., & Pinard, E. (1999). Dynamic in vivo measurement of erythrocyte velocity and flow in capillaries and of microvessel diameter in the rat brain by confocal laser microscopy. *Journal of Cerebral Blood Flow and Metabolism*. <https://doi.org/10.1097/00004647-199908000-00005>
- Shah, K., & Weissleder, R. (2005). Molecular optical imaging: applications leading to the development of present day therapeutics. *NeuroRx : The Journal of the American Society for Experimental NeuroTherapeutics*, *2*(2), 215–225.
<https://doi.org/10.1602/neurorx.2.2.215>
- Shang, Y., Li, T., & Yu, G. (2017). Clinical applications of near-infrared diffuse correlation spectroscopy and tomography for tissue blood flow monitoring and imaging. *Physiological Measurement*, *38*(4), R1--R26. <https://doi.org/10.1088/1361-6579/aa60b7>

- Shih, A. Y., Driscoll, J. D., Drew, P. J., Nishimura, N., Schaffer, C. B., & Kleinfeld, D. (2012). Two-photon microscopy as a tool to study blood flow and neurovascular coupling in the rodent brain. In *Journal of Cerebral Blood Flow and Metabolism*.
<https://doi.org/10.1038/jcbfm.2011.196>
- Sie, E. J., Chen, H., Saung, E.-F., Catoen, R., Tietze, T., Chevillet, M. A., & Marsili, F. (2020). High-sensitivity multispeckle diffuse correlation spectroscopy. *NeuroPhotonics*, 7(3), 1–15.
<https://doi.org/10.1117/1.NPh.7.3.035010>
- Siket, M., Jánoki, I., Demeter, K., Szabó, M., & Földesy, P. (2021). Time varied illumination laser speckle contrast imaging. *Optics Letters*. <https://doi.org/10.1364/ol.413767>
- Steinmeier, R., Bondar, I., Bauhuf, C., & Fahlbusch, R. (2002). Laser Doppler flowmetry mapping of cerebrocortical microflow: Characteristics and limitations. *NeuroImage*.
<https://doi.org/10.1006/nimg.2001.0943>
- Stern, M. D. (1975). In vivo evaluation of microcirculation by coherent light scattering. *Nature*, 254(5495), 56–58. <https://doi.org/10.1038/254056a0>
- Sullender, C. T., Richards, L. M., He, F., Luan, L., & Dunn, A. K. (2022). Dynamics of isoflurane-induced vasodilation and blood flow of cerebral vasculature revealed by multi-exposure speckle imaging. *Journal of Neuroscience Methods*, 366, 109434.
<https://doi.org/https://doi.org/10.1016/j.jneumeth.2021.109434>
- Sun, S., Hayes-Gill, B. R., He, D., Zhu, Y., & Morgan, S. P. (2015). Multi-exposure laser speckle contrast imaging using a high frame rate CMOS sensor with a field programmable gate array. *Opt. Lett.*, 40(20), 4587–4590. <https://doi.org/10.1364/OL.40.004587>

- Sutin, J., Zimmerman, B., Tyulmankov, D., Tamborini, D., Wu, K. C., Selb, J., Gulinatti, A., Rech, I., Tosi, A., Boas, D. A., & Franceschini, M. A. (2016). Time-domain diffuse correlation spectroscopy. *Optica*, 3(9), 1006–1013.
<https://doi.org/10.1364/OPTICA.3.001006>
- Takanezawa, S., Saitou, T., & Imamura, T. (2021). Wide field light-sheet microscopy with lens-axicon controlled two-photon Bessel beam illumination. *Nature Communications*.
<https://doi.org/10.1038/s41467-021-23249-y>
- Tarantini, S., Fulop, G. A., Kiss, T., Farkas, E., Zölei-Szénási, D., Galvan, V., Toth, P., Csiszar, A., Ungvari, Z., & Yabluchanskiy, A. (2017). Demonstration of impaired neurovascular coupling responses in TG2576 mouse model of Alzheimer's disease using functional laser speckle contrast imaging. *GeroScience*, 39(4), 465–473. <https://doi.org/10.1007/s11357-017-9980-z>
- Teng, Y., Hao, Y., Liu, H., Shan, M., Chen, Q., Song, K., & Wang, Y. (2022). Histology and Vascular Architecture Study of Keloid Tissue to Outline the Possible Terminology of Keloid Skin Flaps. *Aesthetic Plastic Surgery*. <https://doi.org/10.1007/s00266-022-02775-0>
- Tom, W. J., Ponticorvo, A., & Dunn, A. K. (2008). Efficient Processing of Laser Speckle Contrast Images. *IEEE Transactions on Medical Imaging*, 27(12), 1728–1738.
<https://doi.org/10.1109/TMI.2008.925081>
- Toricelli, A., Contini, D., Pifferi, A., Caffini, M., Re, R., Zucchelli, L., & Spinelli, L. (2014). Time domain functional NIRS imaging for human brain mapping. *NeuroImage*, 85, 28–50.
<https://doi.org/https://doi.org/10.1016/j.neuroimage.2013.05.106>

- Tripathi, M. M., Hajjarian, Z., Van Cott, E. M., & Nadkarni, S. K. (2014). Assessing blood coagulation status with laser speckle rheology. *Biomedical Optics Express*.
<https://doi.org/10.1364/boe.5.000817>
- Tsukada, K., Minamitani, H., Sekizuka, E., & Oshio, C. (2000). Image correlation method for measuring blood flow velocity in microcirculation: Correlation “window” simulation and in vivo image analysis. *Physiological Measurement*. <https://doi.org/10.1088/0967-3334/21/4/303>
- Tsukada, K., Sekizuka, E., Oshio, C., Tsujioka, K., & Minamitani, H. (2004). Red blood cell velocity and oxygen tension measurement in cerebral microvessels by double-wavelength photoexcitation. *Journal of Applied Physiology*.
<https://doi.org/10.1152/jappphysiol.00764.2003>
- Vaishnavi, S. N., Vlassenko, A. G., Rundle, M. M., Snyder, A. Z., Mintun, M. A., & Raichle, M. E. (2010). Regional aerobic glycolysis in the human brain. *Proceedings of the National Academy of Sciences of the United States of America*.
<https://doi.org/10.1073/pnas.1010459107>
- Varma, H. M., Valdes, C. P., Kristoffersen, A. K., Culver, J. P., & Durduran, T. (2014). Speckle contrast optical tomography: A new method for deep tissue three-dimensional tomography of blood flow. *Biomedical Optics Express*, 5(4), 1275–1289.
<https://doi.org/10.1364/BOE.5.001275>
- Vellekoop, I. M., & Mosk, A. P. (2008). Phase control algorithms for focusing light through turbid media. *Optics Communications*, 281(11), 3071–3080.
<https://doi.org/https://doi.org/10.1016/j.optcom.2008.02.022>

- Venugopal, K., Unni, S. N., Bach, A., Conzen, C., & Lindauer, U. (2019). Assessment of cerebral hemodynamics during neurosurgical procedures using laser speckle image analysis. *Journal of Biophotonics*. <https://doi.org/10.1002/jbio.201800408>
- Wang, C., Cao, Z., Jin, X., Lin, W., Zheng, Y., Zeng, B., & Xu, M. (2019). Robust quantitative single-exposure laser speckle imaging with true flow speckle contrast in the temporal and spatial domains. *Biomedical Optics Express*. <https://doi.org/10.1364/boe.10.004097>
- Wang, D., Parthasarathy, A. B., Baker, W. B., Gannon, K., Kavuri, V., Ko, T., Schenkel, S., Li, Z., Li, Z., Mullen, M. T., Detre, J. A., & Yodh, A. G. (2016). Fast blood flow monitoring in deep tissues with real-time software correlators. *Biomedical Optics Express*. <https://doi.org/10.1364/boe.7.000776>
- Wang, L. V., & Hu, S. (2012). Photoacoustic Tomography: In Vivo Imaging from Organelles to Organs. *Science*, *335*(6075), 1458–1462. <https://doi.org/10.1126/science.1216210>
- Wang, Y., Wen, D., Chen, X., Huang, Q., Chen, M., Lu, J., & Li, P. (2017). Improving the estimation of flow speed for laser speckle imaging with single exposure time. *Optics Letters*, *42*(1), 57. <https://doi.org/10.1364/OL.42.000057>
- Widginton, D. W. (1986). Practical laser safety. In *Journal of Occupational Accidents* (2nd ed., Vol. 8, Issue 3, pp. 228–229). [https://doi.org/10.1016/0376-6349\(86\)90010-6](https://doi.org/10.1016/0376-6349(86)90010-6)
- Xu, J., Jahromi, A. K., Brake, J., Robinson, J. E., & Yang, C. (2020). Interferometric speckle visibility spectroscopy (ISVS) for human cerebral blood flow monitoring. *APL Photonics*, *5*(12), 126102. <https://doi.org/10.1063/5.0021988>
- Yodh, A. G., Kaplan, P. D., & Pine, D. J. (1990). Pulsed diffusing-wave spectroscopy: High resolution through nonlinear optical gating. *Phys. Rev. B*, *42*(7), 4744–4747. <https://doi.org/10.1103/PhysRevB.42.4744>

- Yoon, J. (2022). Hyperspectral Imaging for Clinical Applications. *BioChip Journal*.
<https://doi.org/10.1007/s13206-021-00041-0>
- Yu, G., Floyd, T. F., Durduran, T., Zhou, C., Wang, J., Detre, J. A., & Yodh, A. G. (2007). Validation of diffuse correlation spectroscopy for muscle blood flow with concurrent arterial spin labeled perfusion MRI. *Opt. Express*, *15*(3), 1064–1075.
<https://doi.org/10.1364/OE.15.001064>
- Yu, J., Xu, G., Miao, P., & Tong, S. (2021). Label-free intraoperative blood flow imaging and augmented reality display in surgical microscope. *International IEEE/EMBS Conference on Neural Engineering, NER*. <https://doi.org/10.1109/NER49283.2021.9441393>
- Yuan, S., Devor, A., Boas, D. A., & Dunn, A. K. (2005). Determination of optimal exposure time for imaging of blood flow changes with laser speckle contrast imaging. *Applied Optics*.
<https://doi.org/10.1364/AO.44.001823>
- Zakharov, P., Völker, a C., Wyss, M. T., Haiss, F., Calcinaghi, N., Zunzunegui, C., Buck, a, Scheffold, F., & Weber, B. (2009). Dynamic laser speckle imaging of cerebral blood flow. *Optics Express*, *17*(16), 13904–13917. <https://doi.org/10.1364/OE.17.013904>
- Zeng, Y., Acord, M., Kaovasia, T. P., Miao, P., Sun, J., Tong, S., Curry, E., Aghabaglou, F., Theodore, N., Thakor, N., & Manbachi, A. (2021). *A Miniature Laser Speckle Contrast Imager for Monitoring the Neuromodulatory Effect of Transcranial Ultrasound Stimulation*.
<https://doi.org/10.1115/DMD2021-1038>
- Zhang, H. F., Maslov, K., Stoica, G., & Wang, L. V. (2006). Functional photoacoustic microscopy for high-resolution and noninvasive in vivo imaging. *Nature Biotechnology*, *24*(7), 848–851. <https://doi.org/10.1038/nbt1220>

- Zhao, M., Huang, C., Mazdeyasna, S., & Yu, G. (2021). Extraction of tissue optical property and blood flow from speckle contrast diffuse correlation tomography (scDCT) measurements. *Biomed. Opt. Express*, *12*(9), 5894–5908. <https://doi.org/10.1364/BOE.429890>
- Zhou, W., Kholiqov, O., Chong, S. P., & Srinivasan, V. J. (2018). Highly parallel, interferometric diffusing wave spectroscopy for monitoring cerebral blood flow dynamics. *Optica*. <https://doi.org/10.1364/optica.5.000518>
- Zhou, W., Kholiqov, O., Zhu, J., Zhao, M., Zimmermann, L. L., Martin, R. M., Lyeth, B. G., & Srinivasan, V. J. (2021). Functional interferometric diffusing wave spectroscopy of the human brain. *Science Advances*, *7*(20), eabe0150. <https://doi.org/10.1126/sciadv.abe0150>
- Zimm, B. H. (1945). Molecular Theory of the Scattering of Light in Fluids. *The Journal of Chemical Physics*, *13*(4), 141–145. <https://doi.org/10.1063/1.1724013>
- Zimm, B. H. (1948). Apparatus and Methods for Measurement and Interpretation of the Angular Variation of Light Scattering; Preliminary Results on Polystyrene Solutions. *The Journal of Chemical Physics*, *16*(12), 1099–1116. <https://doi.org/10.1063/1.1746740>

Appendix A: Copyright Permissions

Copyright permission for Figure 2.1 is given below.

| | |
|---|---|
| SPRINGER NATURE | <p>Study of photoluminescence property on cellulosic fabric using multifunctional biomaterials riboflavin and its derivative Flavin mononucleotide</p> <p>Author: Sweta Narayanan Iyer et al Publication: Scientific Reports Publisher: Springer Nature Date: Jun 18, 2019</p> <p><i>Copyright © 2019, The Author(s)</i></p> |
| <p>Creative Commons</p> <p>This is an open access article distributed under the terms of the Creative Commons CC BY license, which permits unrestricted use, distribution, and reproduction in any medium, provided the original work is properly cited.</p> <p>You are not required to obtain permission to reuse this article.</p> <p>To request permission for a type of use not listed, please contact Springer Nature</p> | |

Copyright permission for Figure 2.2 is given below.

| | |
|------------------------|--|
| SPRINGER NATURE | In Vivo Measurement of Optical Properties of Human Skin for 450–800 nm and 950–1600 nm Wavelengths |
| | Author: Takahiro Kono et al Publication: International Journal of Thermophysics Publisher: Springer Nature Date: Apr 26, 2019 |
| | <i>Copyright © 2019, The Author(s)</i> |

| |
|---|
| Creative Commons |
| This is an open access article distributed under the terms of the Creative Commons CC BY license, which permits unrestricted use, distribution, and reproduction in any medium, provided the original work is properly cited. |
| You are not required to obtain permission to reuse this article. |
| To request permission for a type of use not listed, please contact Springer Nature |

Copyright permission for Figure 2.3 is given below.

SPRINGER NATURE

Thank you for your order!

Dear Abdul Mohaimen Safi,

Thank you for placing your order through Copyright Clearance Center's RightsLink® service.

Order Summary

Licensee: University of South Florida
Order Date: Mar 27, 2022
Order Number: 5277010418814
Publication: Springer eBook
Title: Biomedical in vivo Optical Imaging for Disease Espying and Diagnosis
Type of Use: Thesis/Dissertation
Order Total: 0.00 USD

View or print complete [details](#) of your order and the publisher's terms and conditions.

Sincerely,
Copyright Clearance Center

Tel: +1-855-239-3415 / +1-978-646-2777
customercare@copyright.com
<https://myaccount.copyright.com>

 **CCC** RightsLink®

Copyright permission for Figure 2.5 (a) is given below.

SPRINGER NATURE

Thank you for your order!

Dear Abdul Mohaimen Safi,

Thank you for placing your order through Copyright Clearance Center's RightsLink® service.

Order Summary


| | |
|---------------|---|
| Licensee: | University of South Florida |
| Order Date: | Mar 27, 2022 |
| Order Number: | 5277011433854 |
| Publication: | Springer eBook |
| Title: | Development of Near-Infrared Diffuse Correlation Spectroscopy for Noninvasive Monitoring of Cerebral Blood Flow |
| Type of Use: | Thesis/Dissertation |
| Order Total: | 0.00 USD |

View or print complete [details](#) of your order and the publisher's terms and conditions.

Sincerely,

Copyright Clearance Center

Tel: +1-855-239-3415 / +1-978-646-2777
customercare@copyright.com
<https://myaccount.copyright.com>

 RightsLink®

Copyright permission for Figure 2.6 is given below.

Time-domain diffuse correlation spectroscopy (TD-DCS) for noninvasive, depth-dependent blood flow quantification in human tissue in vivo

Author: Saeed Samaei et al

Publication: Scientific Reports

Publisher: Springer Nature

Date: Jan 19, 2021

Copyright © 2021, The Author(s)

SPRINGER NATURE


Creative Commons

This is an open access article distributed under the terms of the [Creative Commons CC BY](#) license, which permits unrestricted use, distribution, and reproduction in any medium, provided the original work is properly cited.

You are not required to obtain permission to reuse this article.

To request permission for a type of use not listed, please contact [Springer Nature](#)

Copyright permission for content use in chapter 3, and chapter 5 is given below.

 **Optica Publishing Group Copyright** March 7, 2022 at 10:49 AM
RE: Permission require to reuse the conference paper ID : BTh1B.6 "Quantitative Measurement of Static and Dynamic Tissue Optical Properties with Contin...
To: Abdul Mohaimen Safi, Optica Publishing Group Copyright [Details](#)

Dear Abdul Mohaimen Safi,

Thank you for contacting Optica Publishing Group.

For the use of material from A. M. Safi, S. Moka, M. Harrah, S. Cini, and A. B. Parthasarathy, "Quantitative Measurement of Static and Dynamic Tissue Optical Properties with Continuous Wave Pathlength Resolved Diffuse Correlation Spectroscopy," in Biophotonics Congress 2021, C. Boudoux, K. Maitland, C. Hendon, M. Wojtkowski, K. Quinn, M. Schanne-Klein, N. Durr, D. Elson, F. Cichos, L. Oddershede, V. Emiliani, O. Maragò, S. Nic Chormaic, N. Pégard, S. Gibbs, S. Vinogradov, M. Niedre, K. Samkoe, A. Devor, D. Peterka, P. Blinder, and E. Buckley, eds., OSA Technical Digest (Optica Publishing Group, 2021), paper BTh1B.6 and A. M. Safi, C. Hernandez-Isidro, S. Cini, S. Moka, M. Harrah, C. L. Passaglia, and A. B. Parthasarathy, "Quantitative Cerebral Blood Flow Imaging with Synthetic Single-Shot Multi-Exposure Laser Speckle Imaging," in Biophotonics Congress 2021, C. Boudoux, K. Maitland, C. Hendon, M. Wojtkowski, K. Quinn, M. Schanne-Klein, N. Durr, D. Elson, F. Cichos, L. Oddershede, V. Emiliani, O. Maragò, S. Nic Chormaic, N. Pégard, S. Gibbs, S. Vinogradov, M. Niedre, K. Samkoe, A. Devor, D. Peterka, P. Blinder, and E. Buckley, eds., OSA Technical Digest (Optica Publishing Group, 2021), paper BW3B.4:

Optica Publishing Group only has copyright for the compilation of the conference proceedings, not the individual papers themselves. As the authors retain copyright to the individual paper, an credit statement is not needed, although we do request a complete citation be included in any publication or adjacent to any posting.

Please let me know if you have any questions.


Kind Regards,
Hannah Greenwood

Hannah Greenwood
March 7, 2022
Authorized Agent, Optica Publishing Group

OPTICA
PUBLISHING GROUP Part of **OSA**

Accepted paper for content use in chapter 4 is given below.

BioMed 2022 | Contributed Paper | Control ID 3703148

M msigillito@optica.org <onbehalf@abstractcentral.com> 
Wed 1/26/2022 12:05 PM

To: Abdul Mohaimen Safi
Cc: Abdul Mohaimen Safi; Ashwin Parthasarathy

Dear Abdul Mohaimen Safi,

On behalf of the [2022 Biophotonics Congress: Biomedical Optics](#) Technical Program Committee, we are pleased to inform you that your paper has been sessioned for an oral presentation at the BioMed 2022 meeting which is scheduled in Fort Lauderdale, Florida, USA, 24 – 27 April 2022. Technical sessions will be presented live from the Eastern Daylight Time Zone (EDT, UTC -04:00) with a recorded archive available later for on-demand viewing.

Paper Information
Control Number: 3703148
Paper Title: Quantitative Blood Flow Imaging at Photon Shot Noise Limit with Heterodyne Synthetic Multi-Exposure Laser Speckle Imaging
Author block: Abdul Mohaimen Safi(1); Ashwin Parthasarathy(1); 1. University of South Florida, Tampa, FL, United States.

Presentation Information
Presenting Author: Abdul Mohaimen Safi
Session Time and Dates: April 25, 2022 from 3:00 PM to 5:00 PM EDT
Session Title: Diffuse Correlation and Laser Speckle Techniques

The final ID and the time for your presentation will be sent closer to the meeting. The presenting author must be a co-author listed above. If you have any edits to your author block, please email Maria Sigillito at msigillito@optica.org no later than 7 February 2022.

Appendix B: IRB approval Pages

IRB approval for experiments performed in chapter 4 and 5 is given below.



APPROVAL

January 14, 2021

This letter supersedes the letter dated November 23, 2020

Ashwin Parthasarathy
4202 E Fowler Ave
ENB 118
Tampa, FL 33620

Dear Dr. Ashwin Parthasarathy:

On 11/17/2020, the IRB reviewed and approved the following protocol:

| | |
|---|---|
| Application Type: | Continuing Review |
| IRB ID: | Pro00039832_CR000001 |
| Review Type: | Committee |
| Title: | Noninvasive monitoring of tissue hemodynamics with diffuse optical techniques |
| Funding: | None |
| IND, IDE, or HDE: | None |
| Approved Protocol and Consent(s)/Assent(s): | <ul style="list-style-type: none">• Omnibus_IRB_V2_2_CleanCopy.pdf;• Omnibus Informed Consent V3 Clean Copy.pdf; Approved study documents can be found under the 'Documents' tab in the main study workspace. Use the stamped consent found under the 'Last Finalized' column under the 'Documents' tab. |


The IRB approved the protocol from 11/17/2020 to 11/17/2021. Within 45 days of 11/17/2021, submit a continuing review/study closure request in BullsIRB by clicking Create Modification/CR.

If continuing review approval is not granted before the expiration date of 11/17/2021, approval of this protocol expires on that date.

In conducting this protocol you are required to follow the requirements listed in the INVESTIGATOR MANUAL (HRP-103).

Appendix C: IACUC approval Pages

IACUC approval for experiments performed in chapter 4 is given below.




**UNIVERSITY OF
SOUTH FLORIDA**
USF RESEARCH & INNOVATION

**RESEARCH INTEGRITY & COMPLIANCE
INSTITUTIONAL ANIMAL CARE & USE COMMITTEE**

MEMORANDUM

TO: Christopher Passaglia,

FROM: 
Farah Moulvi, MSPH, IACUC Coordinator
Institutional Animal Care & Use Committee
Research Integrity & Compliance

DATE: 8/3/2021

PROJECT TITLE: Structure and function of healthy and glaucomatous eyes

FUNDING SOURCE: Federal government or major agency that awards grants based on peer-reviewed proposals (NIH, NSF, DOD, AHA, ACS, etc.)
National Eye Institute

IACUC PROTOCOL #: R IS00009432

PROTOCOL STATUS: **APPROVED**

The Institutional Animal Care and Use Committee (IACUC) reviewed your application requesting the use of animals in research for the above-entitled study. The IACUC **APPROVED** your request to use the following animals in your **protocol for a one-year period beginning 8/3/2021:**

| | |
|---|-----|
| Rat: Brown-Norway (adult, 250-450g, males or females) | 400 |
|---|-----|

Please take note of the following:

- **IACUC approval is granted for a one-year period at the end of which, an annual renewal form must be submitted for years two (2) and three (3) of the protocol through the eIACUC system.** After three years all continuing studies must be completely re-described in a new electronic application and submitted to IACUC for review.
- **All modifications to the IACUC-Approved Protocol must be approved by the IACUC prior to initiating the modification.** Modifications can be submitted to the IACUC for review and approval as an Amendment or Procedural Change through the eIACUC system. These changes must be within the scope of the original research hypothesis, involve the original species and justified in writing. Any change in the IACUC-approved protocol that does not meet the latter definition is considered a major protocol change and requires the submission of a new application.
- **All costs invoiced to a grant account must be allocable to the purpose of the grant.** Costs allocable to one protocol may not be shifted to another in order to meet deficiencies caused by overruns, or for other reasons convenience. Rotation of charges among protocols by month without establishing that the rotation schedule credibly reflects the relative benefit to each protocol is unacceptable.

INSTITUTIONAL ANIMAL CARE AND USE COMMITTEE